Multisensor Microbathymetric Habitat Mapping with a Deep-Towed Ocean Floor Observation and Bathymetry System (OFOBS)

by
Simon Dreutter

A thesis submitted to the HafenCity University Hamburg
in partial fulfillment of the requirements for the degree of
Master of Science
Geomatics (Hydrography)

1st Examiner: Prof. Dr. Karl-Peter Traub
2nd Examiner: Dr. Boris Dorschel

May, 2017

HCU | HafenCity Universität
Hamburg

ALFRED-WEGENER-INSTITUT
HELMHOLTZ-ZENTRUM FÜR POLAR-
UND MEERESFORSCHUNG

Declaration (§20(4) ASPO 2012)

I declare that this Master Thesis – in the case of group work the respective marked parts of the work – has been completed by myself without external help and only the cited sources and references were used.

Literally cited or quotes from different text or other sources are marked.

Hamburg, May 22nd, 2017

(Simon Dreutter)

Acknowledgments

Abstract

To describe the seafloor topography, a number of different bathymetric methods can be applied. These methods vary greatly in coverage, resolution, and topographic uncertainty. Satellite-based gravimetry and radar altimetry can give large-scale structural estimates of the seafloor topography, yet, with a very low resolution and without real depth measurements. Ship-based swath bathymetry systems greatly improve the topographic uncertainty and increase the knowledge on geomorphology and depth of the seafloor. In shallow waters, ship mounted echo-sounders can produce high-resolution data on a submeter level. However, in deep-sea environments, the resolution deteriorates due to large acoustic footprints and a reduced number of measurement points with respect to the mapped area. In order to conduct high-resolution habitat mapping and to resolve small-scale topographic seafloor features, subsea survey vehicles need to be employed. Next to remotely operated or autonomous underwater vehicles, towed camera systems present a comparatively cheap method, both financially and with regards to support requirements, to collect close-range optical seafloor data. Nonetheless, optical sensors have very limited coverage capabilities in the deep sea, due to the nature of the sensors and the high attenuation of light in the water column. Acoustic sensors on the other hand can achieve much wider survey swaths, depending on their operation frequency.

The *Ocean Floor Observation and Bathymetry System (OFOBS)*, developed at the Alfred Wegener Institute for Polar and Marine Research, Germany, offers a novel survey technology for deep-towed multisensor microbathymetric habitat mapping. To augment the traditional optical sensors, the OFOBS was equipped with additional acoustic and navigational sensors. A bathymetric side scan sonar collects lateral seafloor reflection intensity and bathymetry at ranges up to 100 m to both sides of the vehicle. A forward looking sonar records acoustic imagery ahead of the system, which can be used for hazardous obstacle avoidance in rough terrain.

This thesis introduces the newly developed system along with processing workflows for the acquired datasets. Underwater photogrammetric methods are utilized for the optical data, to reconstruct the three dimensional morphology of the seabed. The camera pose estimations of the employed bundle adjustment algorithms are used for local navigation corrections of the acoustic datasets, to achieve best possible data alignment. The resulting multilayer product consists of wide-swath acoustic bathymetry (submeter resolution), multi-frequency side scan mosaics (sub-decimeter resolution), photogrammetric microbathymetry (subcentimeter resolution), and geometrically corrected, georeferenced photo mosaics (submillimeter resolution). These results offer a wide variety of use cases in high-resolution habitat analyses by the associated scientific working groups.

The data used for developing the presented workflow was collected during the *RV Polarstern* expedition PS101 in the extreme environment of the volcanic seamounts along the Langseth Ridge in the high Arctic (87°N, 60°E).

Contents

List of Abbreviations

AMORE	Arctic Mid-Ocean Ridge Expedition
ASCII	American Standard Code for Information Interchange
AUV	Autonomous Underwater Vehicle
AWI	Alfred Wegener Institute for Polar and Marine Research, Bremerhaven, Germany
DEM	Digital Elevation Model
FLS	Forward Looking Sonar
FPS	Frames Per Second
FS	Full Scale
GCP	Ground Control Point
GEBCO	General Bathymetric Chart of the Oceans
GIS	Geographic Information System
GNSS	Global Navigation Satellite System
HD	High Definition
HF	High Frequency
HIPS	Hydrographic Information Processing System
HROV	Hybrid Remote Operated Vehicles
IBCAO	International Bathymetric Chart of the Arctic Ocean
IHO	International Hydrographic Organization
IMU	Inertial Measurement Unit
INS	Inertial Navigation System
IOC	International Oceanographic Commission
LBL	Long Baseline
LED	Light-Emitting Diode
LF	Low Frequency
MAPR	Miniature Autonomous Plume Recorder
MBES	Multibeam Echosounder
MPES	Multiphase Echosounder
MTL	Miniaturized Temperature Data Logger
NMEA	National Marine Electronics Association
NOAA	National Oceanic and Atmospheric Administration
OFOBS	Ocean Floor Observation and Bathymetry System
PANGAEA	Publishing Network for Geoscientific and Environmental Data
RMS	Root Mean Square
ROV	Remotely Operated Vehicle
RV	Research Vessel
SBAS	Satellite Based Augmentation System
SCUFN	Sub-Committee for Undersea Feature Names (GEBCO)
SfM	Structure from Motion
SIPS	Sonar Information Processing System
SLAM	Simultaneous Localization And Mapping
SNR	Signal-to-Noise Ratio
SONAR	Sound Navigation and Ranging
SSS	Side Scan Sonar
SV	Sound Velocity
TPU	Total Propagated Uncertainty
TV MUC	Television Multi Corer
UDP	User Datagram Protocol
USBL	Ultra Short Baseline
UTC	Coordinated Universal Time

List of Figures

List of Tables

1 Introduction

The first bathymetric chart of the central Arctic Ocean was produced by Fridtjof Nansen in the beginning of the last century. His chart showed a single deep basin with little to none distinct seafloor features. Modern large-scale gravimetry and radar altimetry reveal a large abundance of bathymetric features in the Eurasian Basin, such as ridges and seamounts, most of which are located around the Arctic mid-ocean ridge systems. To increase resolution and to gain detailed knowledge on the geomorphology of the seafloor, ship-based swath bathymetry can be used, creating a basis for further research. However, only approximately 11% of the Arctic Ocean are actually mapped with swath bathymetry systems, leaving a high topographic uncertainty in the remaining area (Jakobsson et al., 2015). Especially in research related to smaller scale features, such as individual seamounts, higher resolution surveying techniques need to be utilized.

Seamounts are active or inactive volcanoes, globally distributed on the seafloor. Most of the seamounts originate from volcanic activities near mid-ocean ridges and over volcanic intraplate hotspots (mantle plumes). Since seamounts play a key role in many marine processes due to their specific morphology, Wessel et al. (2010) describe them as the "last major frontier in geographic, geological, and ecological exploration on planet Earth". Seamounts are hotspots for marine faunal abundance and biological productivity, act as barriers for currents, influencing vertical mixing of the ocean, and determine the habitats of a large number of marine communities (Wessel et al., 2010; Boetius, 2016).

In order to investigate the geophysical, geological, and biological characteristics of seamounts, several scientific sampling methods can be applied to acquire discrete information on seabed morphology and faunal distribution. To conduct large-area habitat mapping, different subsea survey methods are available for high-resolution bathymetric measurements and videographic observation of the seabed. One of those methods is the use of towed systems with the goal to bring surveying sensors closer to the seabed for higher resolution results. The here presented system is the newly developed *Ocean Floor Observation and Bathymetry System (OFOBS)*, a deep-towed frame, equipped with a sensor suite for close-range, high-resolution habitat mapping.

The aims of this work are to introduce the novel multisensor habitat mapping approach, to develop a workflow for processing the acquired datasets, and to evaluate and discuss the resulting products. The main questions to be answered are:

- What are the capabilities of the OFOBS in deep-sea habitat mapping, both qualitative and in terms of resulting resolution and accuracy?
- What are the advantages of the multisensor setup in order to overcome survey uncertainties and to improve microbathymetric results of the mapped area?
- How can the OFOBS surveys contribute to ongoing research on deep-sea habitats?

The thesis is structured as follows. Chapter 2 will introduce the OFOBS by listing the onboard sensors and briefly explaining their working principles as well as by giving an overview of the general dive procedure. Chapter 3 describes the study area in which the data was acquired that was used for developing the processing workflow. Chapter 4 outlines the characteristics of the different recorded raw datasets. These introductory chapters are fundamental for understanding the technical prerequisites, the environmental survey conditions under which the data was acquired, and the type and quality specifications of the raw data. All these factors had to be considered in the further work on the project. Chapter 5 explains the developed processing workflow, structured by the nature of the data (optical, acoustic, navigation) and the used software. It will be explained, how the datasets were combined to adjust and improve the overall results. Chapter 6 presents the different data products, obtained from the methods, outlined in chapter 5. Chapter 7 discusses the presented process and the results by considering the survey uncertainties and comparing the survey method to technology of similar capabilities. Following up, a number of recommendations will be given for future improvements on the system and resulting changes in the processing workflow. Finally, the data is evaluated with regards to the use in related research and an outlook is given on further work on the acquired datasets. Chapter 8 summarizes the work and draws an overall conclusion.

2 Ocean Floor Observation and Bathymetry System

The OFOBS is a deep-towed device for close-range marine benthic habitat mapping. The setup consists of two primary components, a topside unit with power supply, network facilities and control computers, as well as a subsea unit. Both components are connected via a fiber optic tether cable within the operating ship's winch system.

The subsea unit is a sturdy steel frame that holds the sensor suite adapted to the various mapping tasks. Its dimensions are 235L x 92W x 105H cm and it has a weight of 1 ton in air. The system is rated to a maximum operation depth of 6000 m. Figure 2-1 shows the OFOBS subsea unit coming back on deck after a completed dive in the high Arctic.

This section will give an overview over the instruments and a brief introduction on some of the working principles. Additionally, the normal OFOBS dive procedure will be outlined and the raw, unprocessed data output of the various sensors will be presented.

Figure 2-1: OFOBS subsea unit coming back on deck of *RV Polarstern* (Photo: Frederic Tardeck)

2.1 Instruments

The OFOBS, developed by the Alfred Wegener Institute, Germany, is the extended version of the *Ocean Floor Observation System* (OFOS, without the bathymetric sensors). The OFOS was originally developed within the Helmholtz program ROBEX and was built with a set of cameras, lights, flashes, scaling lasers and a rudimentary navigation setup (Bergmann et al., 2011; Purser et al., In review). It was meant for visual-only exploration and mapping of marine benthic habitats. With an operation altitude of about 1.5–5 m above the seafloor the OFOS produces high resolution still images and video data. The lights and flashes assure proper lighting conditions for the cameras even at great depths without any remaining sunlight. However, the high scattering and absorption levels of light within the water column greatly limit the altitude of the system, hence the coverage of the imaging sensors.

Acoustic systems in comparison can achieve significantly wider ranges with respect to setup size and power consumption. To extend the survey coverage and to augment the original camera setup, the OFOS was additionally equipped with a bathymetric side scan sonar for lateral measurements, a forward looking sonar, and some auxiliary sensors needed for bathymetric data collection.

Figure 2-2 shows a schematic view of the OFOBS with all the installed subsystems. The design drawings of the frame are attached in Appendix A and include all dimensions and relevant offsets between the different sensors. The larger cuboid frame, in the front, is the original system and the extended tailpiece holds most of the newly installed subsystems. The connection scheme of these new bathymetry instruments is illustrated in Figure 2-3. In the following subsections, the different parts will be explained in more detail.
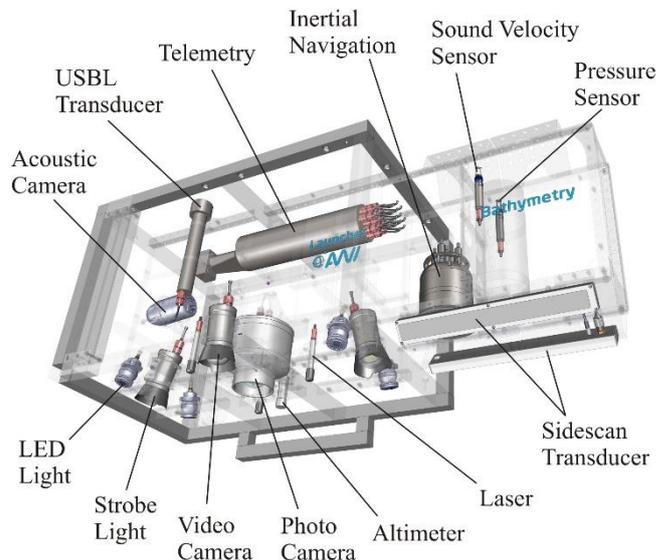
Figure 2-2: Schematic view of the OFOBS instruments (Purser et al., In review)
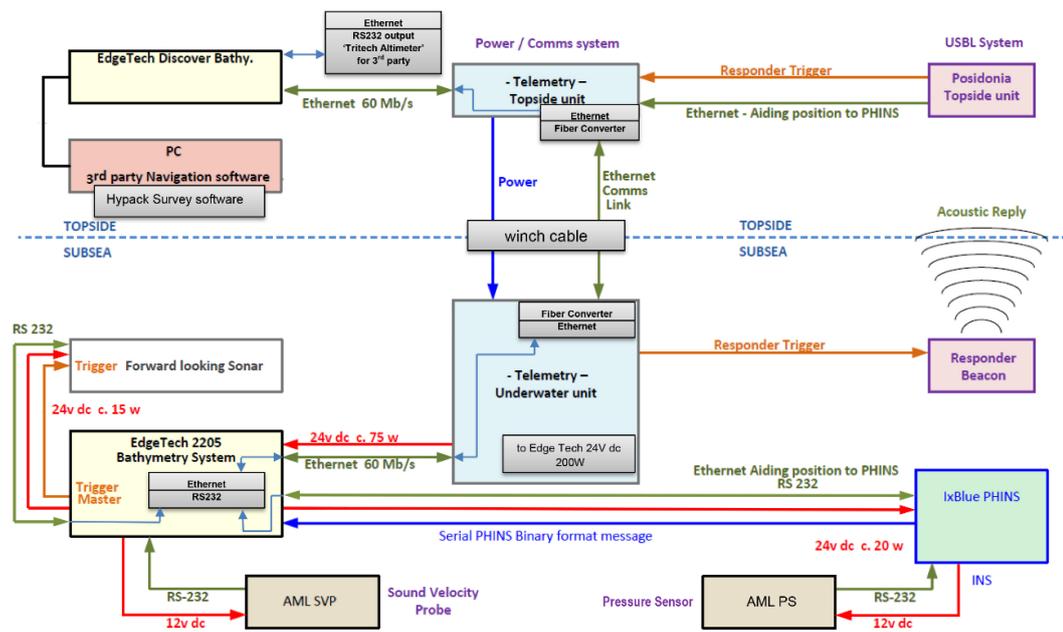
Figure 2-3: OFOBS connection diagram (adapted from EdgeTech, original schematic supplied with the hardware)

2.1.1 Power Supply, Communication & Data Storage

The tether/tow cable serves two purposes: it provides power to the subsea unit and creates a network between the two components. Powering the system via a cable allows running the different instruments with high frequency over long durations. The dive time can be adjusted to the individual circumstances if needed, without the limitation of a battery-powered setup.

The high-speed fiber optic network between the subsea and the topside units allows two-way communication with sufficient bandwidth between control PCs and the instruments. This enables the operator(s) to change survey parameters during operation and view results in real time.

Data recording is also done on the ship-based PCs. This has the disadvantage of data gaps in case of network outages, but there are a number of upsides to this approach. With topside data collection, there is no need for extra physical hard drive space on the instrument directly, the data is safe, even in the case of serious failure or loss of the subsea unit, and collected data can be checked, evaluated and post processed while the dive is still in progress.

2.1.2 Navigation & Attitude

The OFOBS contains three instruments that make up the navigation setup: a pressure sensor, an ultra-short baseline (USBL) transponder and an inertial navigation system (INS). The pressure sensor is an *AML Micro-X 6000 P-Xchange* that measures pressure in dBar with an accuracy of

0.05% FS and a precision of 0.03% FS, up to 6000 dbar (AML Oceanographic (Ed.), 2015). The sensor feeds the measurements into the INS via serial connection.

The USBL transponder communicates with the ship-mounted USBL system. The setup described here is specific for *RV Polarstern* and can differ depending on the system availability on other vessels. On *Polarstern*, the USBL system is an *iXBlue Posidonia* antenna connected to an *iXBlue USBL-Box*. The ship-based USBL operates on 10.5 kHz and covers a 60°-wide cone (30° from nadir) below the antenna and the subsea transponder operates on 9.5 kHz (Boetius & Purser, 2017). By triangulation, the USBL system tracks the subsea transponder with an nominal position accuracy of 0.2% of the slant distance (IXSEA (Ed.), 2010c; iXBlue (Ed.), 2011; iXBlue (Ed.), 2016), which, however, can depend greatly on the survey conditions. Aided by the ships GNSS positioning system and inertial measurement unit (IMU), the measured relative position of the USBL transponder is georeferenced on the fly.

The heart of the OFOBS navigation setup is an *iXBlue PHINS 6000* INS. The PHINS outputs a navigation solution containing geographic position, depth, true heading, attitude, speed and heave. While motion data comes from the internal 3D fiber optic gyroscopes and accelerometers, the PHINS is aided by the USBL and the pressure sensor. All input signals are processed and fused by a Kalman filter to get a high-rate, real-time position that feeds straight into the bathymetric systems (IXSEA (Ed.), 2010c). The nominal position of the PHINS is three times more accurate than the USBL (iXBlue (Ed.), 2014). In addition to the position and motion output the PHINS is time synchronized with the ships GNSS based timeserver and creates an OFOBS internal time and pulse per second signal for accurate sensor synchronization.

2.1.3 Optical Systems

As previously mentioned, OFOBS is equipped with two downward looking camera systems: a *Canon EOS 5D Mark III* with a 24 mm fixed lens for high-resolution still images and a *Sony FCB-H11* high definition video camera for continuous video recording. Both cameras are mounted in pressure housings, taking images and video through hemispherical dome ports. The cameras are remote controlled within the OFOBS software (*iSiTEC OFOS software package*) on a topside PC. Four *SeaLight sphere 3150* LED lights illuminate the scene from the corners of the OFOBS steel frame to provide constant lighting conditions for the video stream. Two additional *iSiTEC UW-Blitz 250* strobe lights aid the stills camera in achieving sharp high-quality images without motion blur (Purser et al., In review). Three parallel scaling lasers, arranged in a triangle around the stills camera, create three red laser dots in every image and video to estimate the size of objects within the shots; the distance between each laser is 50 cm (+/- 1 cm).

The video stream is recorded with 25 fps in Full HD resolution (1920 x 1080 pixels) and still images are taken with 22.3 megapixels, resulting in an image resolution of 5760 x 3840 pixels. A timer triggers the stills camera every 20 seconds to remove observer bias in statistical evaluations of the images. A hotkey gives the option to trigger the camera manually to record noticeable events in addition to the timer images. Since recharging the strobe lights creates significant

spikes in the overall power consumption, a higher trigger rate than 0.2 Hz is not advised. However, with a survey speed of 0.5 knots and an altitude of around 5 m, this creates acceptable overlap between still images for continuous mosaicking.

At an altitude of 2 m above seafloor, both cameras cover an area of approximately 6.5 m² each, depending on the topography. Increasing the flight height results in a bigger coverage, but as mentioned above, scattering and absorption of light in the water column reduces brightness, hence quality of the image, as will be shown in chapter 4.2.

2.1.4 Acoustic Systems

Two acoustic surveying systems are installed on the OFOBS: an *EdgeTech 2205* multiphase echosounder (MPES) and a *BlueView M900-130* forward looking sonar (FLS). Additionally, a sound velocity (SV) probe (*AML Micro-X 6000 SV-Xchange*) is attached to the frame to aid the MPES for bathymetric signal processing. The schematic in Figure 2-4 demonstrates the acoustic data acquisition with the OFOBS.

AML Micro-X 6000 SV-Xchange

The SV probe measures the return time of a transmitted sound pulse on a known distance to calculate sound velocity in the current water mass; it's nominal accuracy is 0.025 m/s (AML Oceanographic (Ed.), 2015). The measured value is instantly sent to the MPES for real-time phase correction.
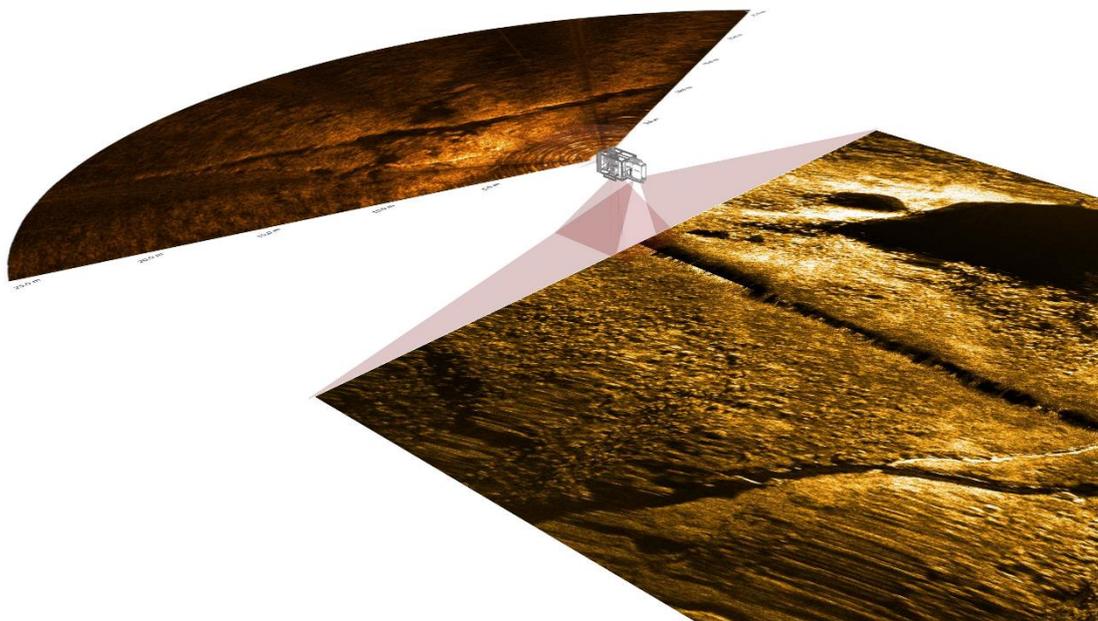
Figure 2-4: Acoustic data acquisition with the OFOBS. For a better representation, the size of the vehicle is not to scale with respect to the sonar ranges. (Purser et al., In review)

EdgeTech 2205 Multiphase Echosounder

The 2205 sonar is the AUV/ROV version of EdgeTech's MPES line, a technology that was introduced by EdgeTech in 2014 (Brisson & Hiller, 2015). MPES technology is a hybrid approach between the two conventional swath echosounder systems, multibeam echosounders (MBES) and phase discriminating bathymetric sonars (PDBS).

MBES use beamforming methods to produce relatively clean and accurate bathymetry measurements with consistent density over the whole swath. However, MBES produce comparatively poor-resolution backscatter data due to their short receive arrays and with widely used single-head systems the swath width is usually limited to approximately 5.5 times the water depth. (de Souza et al., 2015)

PDBS, on the other hand, rely on interferometric methods, have a much wider swath width than MBES, and produce high-resolution side scan data, additional to the bathymetric measurements. PDBS typically use three or more side scan staves in parallel, to infer at least two phase differences to calculate the angle of the received signal. Depending on the number of phase-difference measurements, this technology provides only little information for statistical filtering of the data (standard deviation, mean), and is, therefore, very noisy and susceptible to multi-path effects. With the dual echo, the low signal strength and the resulting high noise in the nadir region under the transducers, PDBS suffer from a very low data density or even a substantial gap in the nadir area. (EdgeTech (Ed.), 2015b)

EdgeTech's MPES, similar to PDBS, are based on side scan sonar (SSS) technology and bring the same advantages, such as wide swath width and simultanious high-resolution side scan and bathymetric data acquisition. But instead of being equipped with parallel side scan staves, the transducer setup holds a side scan array and an additional bathymetric receive array (Figure 2-5). The side scan array transmits a signal in a wide opening across and a narrow opening along track. While the same array is used for receiving the signal for side scan data collection, the signal is also received by the bathymetric array for phase difference measurements (Figure 2-6). The bathymetric array consists of ten vertically aligned staves to infer nine phases-differences. This allows for statistical calculations and filtering techniques to reject dual echos and other extraneous acoustic noise, resulting in a comparatively clean dataset. Additionally, the signal sensitivity can be focused towards the seafloor in order to fill the nadir gap and get an even data density throughout the whole swath. (Brisson & Hiller, 2015; EdgeTech (Ed.), 2015b)

According to Brisson & Wolfe (2014), EdgeTech's MPES technology complies with the IHO Special Order (IHO, 2008) in total vertical uncertainty out to 9.5 times the water depth at a nominal
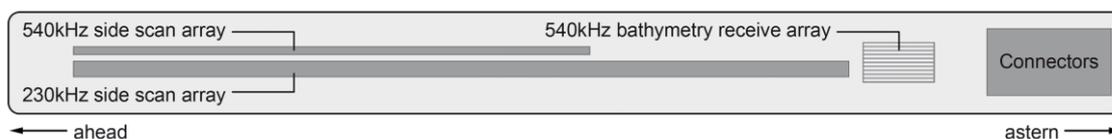
Figure 2-5: Schematic of the 2205 MPES transducer. The dual frequency side scan arrays are positioned up front and the bathymetric receive array with ten stacked is positioned in the back. (Adapted from EdgeTech, original schematic supplied with the hardware)
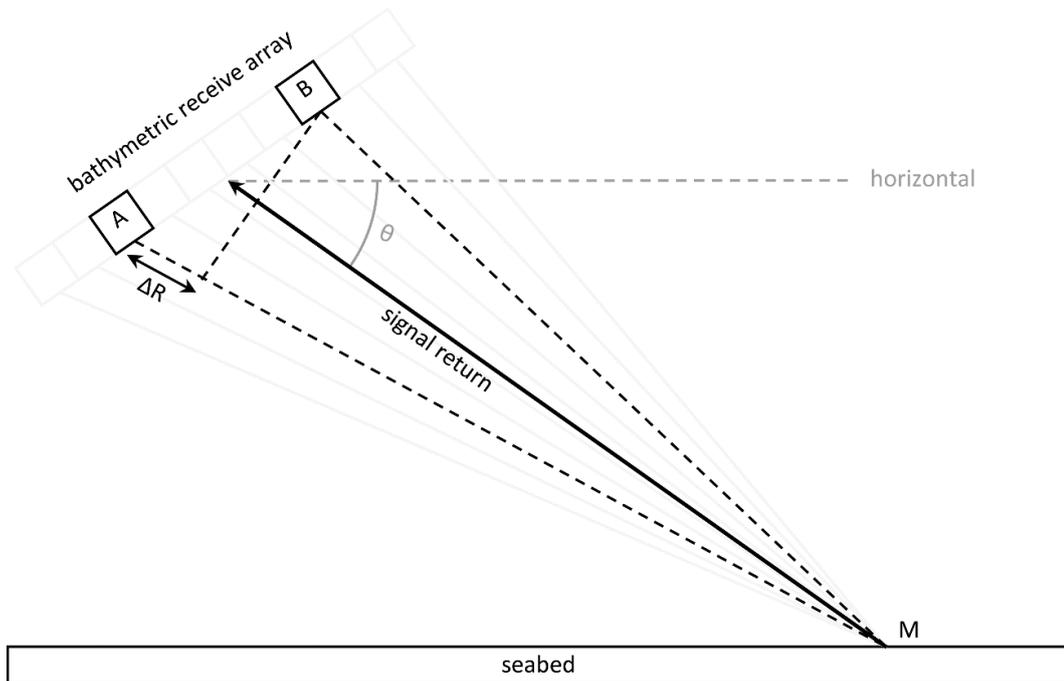
Figure 2-6: Interferometric principle for the EdgeTech MPES. The signal is backscattered from point M on the seabed to the bathymetric receive array and is picked up by the different staves. For explanatory purposes, only two of the ten staves are marked in the figure. The slant range between M and staves A and B is different by ΔR related to the beam angle θ. This difference corresponds to a phase shift on the signal which can be measured on the staves and used to compute θ. (Adapted from Blondel, 2009)

depth of 10 m with a 95% confidence level. In case of subsea systems, *water depth* can be substituted with *altitude over the seabed* at an arbitrary vehicle depth, as this only characterizes the general sounding quality of the system. However, this does not mean that the OFOBS is conducting Special Order bathymetric surveys as the position uncertainty, the pressure sensor uncertainty, and the resulting total propagated uncertainty (TPU) does not comply with the IHO specifications.

The 2205 uses frequency modulated (chirp) pulses and EdgeTech's so called *Full Spectrum™* technology. A broad bandwidth signal and long pulses put a high amount of energy in the water, resulting in a higher achievable range compared to continuous wave systems. The signal processing technology uses proprietary filter techniques that maximize the signal-to-noise ratio (SNR) and result in a side scan image with high dynamic range and high across-track resolution. (EdgeTech (Ed.), 2015a)

Multiple options are available for the frequency setup of the 2205. The one set up in the OFOBS contains a dual frequency side scan sonar with a high frequency (HF) of 540 kHz and a low frequency (LF) of 230 kHz. The bathymetric array receives the HF signal so the swath width of bathymetry data is limited to the range of the HF side scan. Both frequencies can be used for simultaneous data collection. Table 2-1 shows the nominal resolution and range achievements for the OFOBS.

Side scan imagery	230kHz	540kHz
Horizontal beam width (2-way)	0.54°	0.36°
Max range	250 m	150 m
Bathymetry	540kHz	
Beam width	1° x 0.5°	
Max sounding depth	120 m	
Max swath width	200 m	
Max swath sector	200° (100° from nadir)	
Max number of soundings per ping	800	
Sounding Patterns	Equidistant or equiangular	

Table 2-1: EdgeTech 2205 technical specifications (EdgeTech (Ed.), 2015a)

Both of the bathymetric transducers were roll calibrated in a pool trial prior to the expedition, to correct the angular bias from the planned installation angles in the across-track vertical plain. This was done by conducting a standard patch test (IHO, 2005) during the first pool trial post installation.

BlueView M900-130 Forward Looking Sonar

A FLS is a type of imaging sonar that uses multiple beams to create a 2-dimensional wedge-shaped sonar image with one ping, whereas conventional scanning sonars use one beam and mechanical rotation to create an image. FLSs can be used stationary or on moving platforms as they are not affected by motion artifacts. Due to their high update rate and the movie like data characteristics, FLSs are also called acoustic cameras. (Teledyne BlueView (Ed.), 2016)

Like with any imaging sonar, FLS data can easiest be compared to a flashlight, shining on a surface from a small height with an angle close to the horizontal and the user observing the scene from above. Objects with an inclination towards the light give a brighter reflection than objects
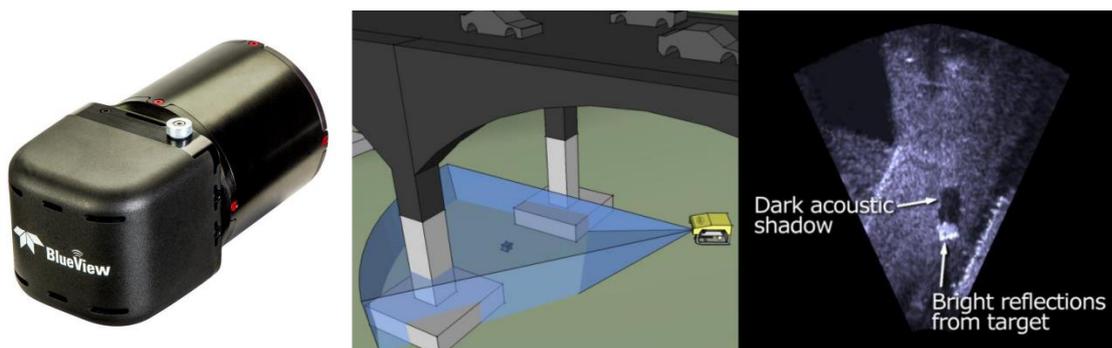
Figure 2-7: BlueView M900-130. (left) 900 transducer, (center) schematic view of ensonified bridge pillars with the FLS mounted on an ROV, (right) resulting 2D sonar image wedge. (Teledyne BlueView (Ed.), 2016)

less inclined towards the light. Behind objects, a shadow occurs and no reflection is visible. While a SSS builds up a 2D image by moving the sensor, a FLS gives an image right away. Figure 2-7 shows the transducer of the M900 and illustrates a resulting data sample of a schematic survey situation.

The M900-130 has a total horizontal opening angle of 130°, divided into 512 beams of 1° x 20° (horizontal x vertical). It operates at an acoustic frequency of 900 kHz, resulting in a sharp image wedge with ranges up to 100 m. The (range dependent) ping rate is up to 25 Hz. However, to prevent acoustic interferences, the OFOBS M900 is triggered by the 2205 sonar, resulting in (range setting dependent) ping rates of around 3 Hz. Table 2-2 summarizes the technical specifications of the M900.

The FLS is mounted in the upper front of the OFOBS subsea unit, about 65 cm above the bottom edge of the steel frame with an angle of 5° downward from the horizontal. At flight heights of around 3–15 m, this installation assures a suitable and even ensonification of the seafloor ahead.

Sonar	M900-130
Field-of view	130°
Maximum range	100 m
Optimum range	2–60 m
Beam width	1° x 20°
Beam spacing	0.18°
No. of beams	512
Update rate within optimum range	Up to 25 Hz
Operating frequency	900 kHz
Depth rating	6000 m

Table 2-2: BlueView M900-130 technical specifications (Teledyne BlueView (Ed.), 2015)

2.1.5 Additional Sensors

The open frame structure of the OFOBS subsea unit allows for easy expansion of the sensor suite for a number of autonomous, battery powered sensors, like the *ANTARES Miniaturized Temperature Data Logger* (MTL) or NOAA's *Miniature Autonomous Plume Recorders* (MAPR) for recording physical and chemical water properties (Baker & Milburn, 1997; Pfender & Villinger, 2002; Boetius & Purser, 2017). Their data can be evaluated after the dive and, if properly timestamped, can be combined with the camera and sonar data to correlate changes in water properties with changes in seafloor characteristics or specific observed features. With consideration of network bandwidth and power resources, the OFOBS could even hold additional cabled instruments with real time data transmission to the topside unit. This might include the above mentioned, but can also be an additional camera, a subsea laser scanner, a sediment echosounder, etc.

2.2 Dive Procedure

The OFOBS is not a standalone system and therefore needs to be set up within the ship's infrastructure before the first dive. However, this process is rather straightforward: the topside unit is mounted and connected to the ships power supply and fiber optic network, and the subsea unit is connected to the winch cable. A number of PCs are connected to the topside network to connect to and control the various imaging and acoustic subsystems of the OFOBS. The following section describes the technical setup of the topside, as well as the different steps of operation between launch and recovery of the OFOBS.

2.2.1 Technical Setup of the Topside Workspace

All OFOBS subsystems do not depend on individual topside processing units, as these are mounted in the subsea unit. Any computer can connect to the network and run the appropriate software to control a specific instrument. Hence, different operation setups are possible. The setup described here was used during *RV Polarstern* research cruise PS101, throughout which the data samples for this thesis where collected (see chapter 3), and therefore serves as an example for the process.

Figure 2-8 shows the OFOBS workspace as it was installed on *RV Polarstern*. A total of seven PCs with additional extension displays, as well as a video recorder (hidden behind laptop (H) in the figure) were used to control the system and record the different data streams. This workspace was divided between four operators. One to control the acoustic and navigation systems (A–E), one to monitor the imaging systems, keep an observation log and take still images with the hotkey (F, G), one to adjust camera settings, lighting intensity and other technical parameters (H, I) and one to run the GIS (J, K). The remaining screen (L) shows ship related auxiliary information like UTC time, geographic position, speed, heading, weather data, etc.
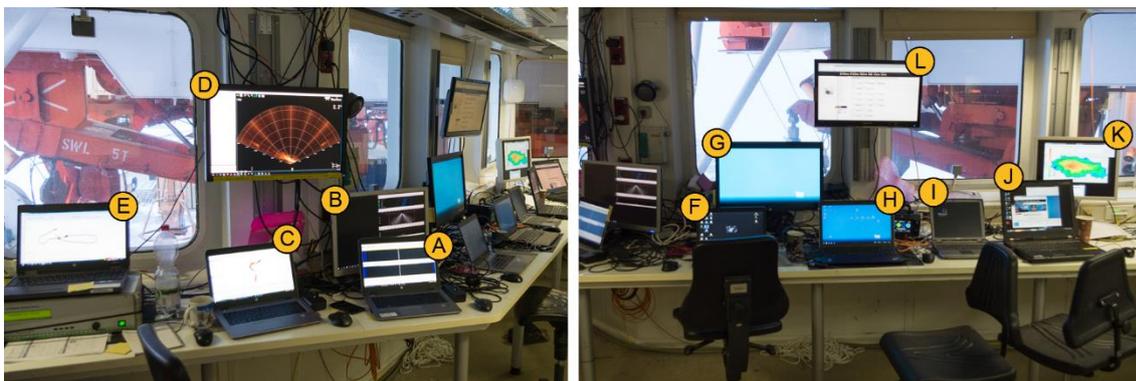
Figure 2-8: OFOBS workspace on *RV Polarstern* during PS101. (A–D) Acoustic systems, (E) navigation screen, (F–H) imaging systems, (J+K) GIS, (I+L) auxiliary information. The equipment is set up in the winch room to allow direct communication between the OFOBS team and the winch driver.

Figure 2-9: OFOBS subsea unit launched with the A-frame of *RV Polarstern*. Deployment is possible over either the side or the stern of the ship. (Photo: Laura Hehemann)

2.2.2 Launch & Descent

After installing the topside workspace, the subsea unit can be prepared for operation. Additional sensors (as mentioned in chapter 2.1.5) have to be primed for use and mounted on the frame. Then the subsea unit can be winched into the water (see Figure 2-9). During takeoff, the OFOBS is not powered due to safety measures, as the device can be supplied with high power loads (600V/700W) and physical contact between decks crew and the frame might be required.

Once in the water, the OFOBS is powered on and lowered down to the seafloor. During descent, all instruments are checked for correct functioning and parameters can be set for the upcoming survey.

At a sufficient distance below the ship (dependent on USBL antenna geometry), the USBL system fixes the transponder position, which is looped back into the OFOBS INS. After the first initial position input, the INS starts a coarse alignment process (five minutes) to find true north and self-calibrate the gyroscopes and accelerometers. The coarse alignment is followed by the fine

alignment process (~30 minutes) where all external inputs (USBL & pressure sensor) are included to build up the internal error model for the extended Kalman filter (IXSEA (Ed.), 2010c). The PHINS will output navigation data while still in fine alignment mode, but a longer descent, resulting in more time to finish the alignment before the actual data collection, helps to improve navigation and motion data quality.

Even though the descent is mostly used for technical checks and debugging, visual data can already be recorded in order to capture water column characteristics like suspended matter or marine snow. Zooplankton and other living beings can be observed and when switching off the lights it can be possible to capture bioluminescent organisms in proximity to the OFOBS.

2.2.3 At Depth

The seafloor is first visible on the SSS at an altitude of approximately 100 m. At ~40 m, the bathymetry is measured and at 15–10 m the seafloor is visible in the camera streams. The latter is of course highly dependent on the water properties and in waters with high suspended-matter concentration, the visibility may be reduced drastically.

Once at survey altitude, instrumentation recordings begin. The flight height of the system can be adjusted in communication with the winch operator. It varies usually between 1.5 m and

Figure 2-10: The OFOBS workspace during a dive on PS101. (foreground) The scientific observer keeps an observation log and controls the manually triggered still image recordings. (background) The GIS operator monitors ship and vehicle tracks for station planning purposes.

10 m to assure reasonable data on both imaging and acoustic systems but depends on the individual research needs. Different altitudes greatly influence the coverage and quality of the different datasets, which will be shown below.

Figure 2-10 shows members of the OFOBS team during PS101. The prominent display on the left shows the live camera feed and a color bar indicating the current vehicle altitude. The winch operator has a mirrored version of the same display. This is necessary for maintaining consistent altitude and to recognize quickly approaching seafloor to react by winching up the unit. Navigating rough terrain, such as seamounts or subsea ridges, is especially challenging, but the FLS can provide crucial support in hazard avoidance. Ensonifying the area ahead with a range of up to 100 m and an opening of 130° can give a good overview of what obstacles lie ahead. Figure 2-11 illustrates how hazardous obstacles are visible in the FLS data.

While the function of the first three mentioned operators in section 2.2.1 is obvious, the GIS operator is not crucial for the OFOBS survey itself, but nevertheless an important contributor to the success of a dive. The GIS holds planned tracks and coordinates of targets as well as a live
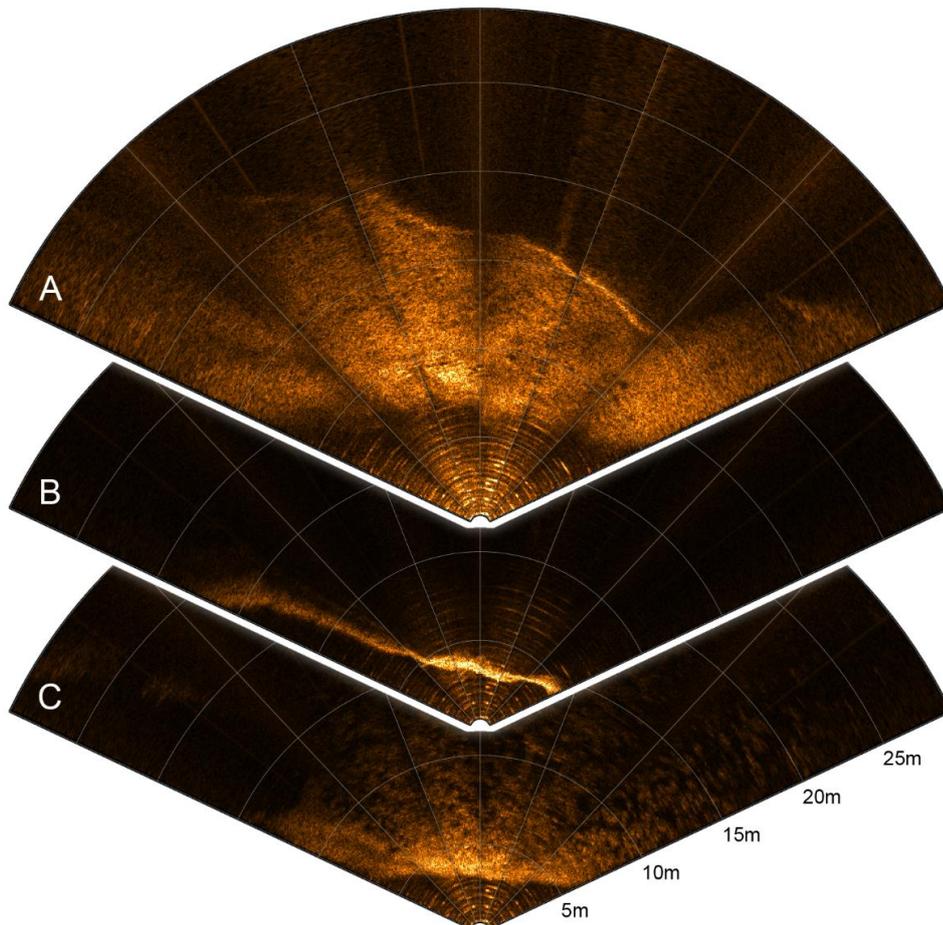
Figure 2-11: Upcoming near-vertical cliff in the FLS image. (A) Cliff ahead at ~15 m. (B) Cliff at less than 5 m distance while winching up the unit, no reflection signal behind the hard reflector of the rocky wall. (C) Upper edge of the cliff with ensonified sponge field behind. (Dreutter et al., 2017a)

position input of the ship and the OFOBS subsea unit (and other possible subsea vehicles if in use). The GIS operator therefore has a good overview and helps significantly with communication between the OFOBS team and the nautical staff on the bridge in order to change speed or course of the towing vessel to adjust the OFOBS survey track. Additionally, display (K) is updated by the GIS operator. It shows a selection of the GIS datasets and functions as a helmsman display, also visible on the bridge, to aid the officer on shift.

2.2.4 Ascent & Recovery

After completing the desired survey transect, recording of the data is stopped and the subsea unit is winched up to the deck. The different datasets are backed up to sufficient storage servers. Upon recovery, the OFOBS can be cleaned and additional sensors can be dismounted and prepared for data retrieval. The characteristics of the different kinds of collected raw data will be described in section 4.

3   Study Area

The OFOBS was enhanced with its acoustic instruments to serve as a new scientific survey tool during the research cruise PS101 on the German icebreaker *Polarstern*. PS101 (Sept 8th 2016 – Oct 23rd 2016) started in Tromsø, Norway, towards the Langseth Ridge in the Central Arctic (87°N, 60°E) and ended in Bremerhaven, Germany. The map in Figure 3-1 shows the cruise track.

The research aim of PS101 was to investigate geophysical, geological, geochemical, and biological processes at seamounts in the ultra-slow oceanic spreading zone Gakkel Ridge (Boetius, 2016). To achieve this, a number of scientific sampling devices and sensors were used throughout the cruise. While most of these devices were deployed at predetermined scientific stations, the OFOBS ran survey transects to gain additional knowledge on morphology and microbathymetry of the seamounts.

The following subsections will give a brief overview on the survey area, the circumstances under which the surveys were conducted, and on the selected sample areas that were used to develop and test the processing workflows within the scope of this thesis.

3.1   Geographic Setting

The research during PS101 focused on seamounts of the Langseth Ridge and adjacent regions in the Gakkel Ridge rift valley in the central Eurasian Basin. The Gakkel Ridge is the slowest spreading ridge in the global mid-ocean ridge system with spreading rates less than 13 mm/yr (Jokat & Schmidt-Aursch, 2007). It forms the boundary between the North American and the Eurasian tectonic plates. On a length of 1800 km, it divides the Eurasian Basin in the Amundsen Basin (northwest) and Nansen Basin (southeast) (Cochran et al., 2003). The ridge shows highly localized volcanism centered on large axis-perpendicular ridges (Dick et al., 2003). Oceanographic measurements conducted during the Arctic Mid-Ocean Ridge Expedition (AMORE) in 2001 also indicated hydrothermal activities along the ridge (Thiede, 2002; Edmonds et al., 2003).

One of those axis-perpendicular ridges is the Langseth Ridge (Figure 3-2). It ascents from the Nansen Basin at 85°55'N towards North, crossing the Gakkel Ridge rift valley at 87°N and extends further up to 87°40'N where it descends into the Amundsen Basin. To be officially included in the GEBCO database for undersea feature names, the ridge was submitted to the sixteenth meeting of the GEBCO Sub-Committee for Undersea Feature names (SCUFN) in 2003 to be named after the geophysicist Dr. Marcus Langseth (IOC & IHO, 2003). The SCUFN database lists the ridge as only the part south of the Gakkel Ridge up to 87°N, but Cochran et al. (2003) describe it as a cross-axis ridge extending to both sides of the Gakkel Ridge. After surveys conducted during PS101, Boetius & Purser (2017) proposed another possible geographical V-shaped extend of the ridge, providing a hypothesis for further geophysical and geological investigation.
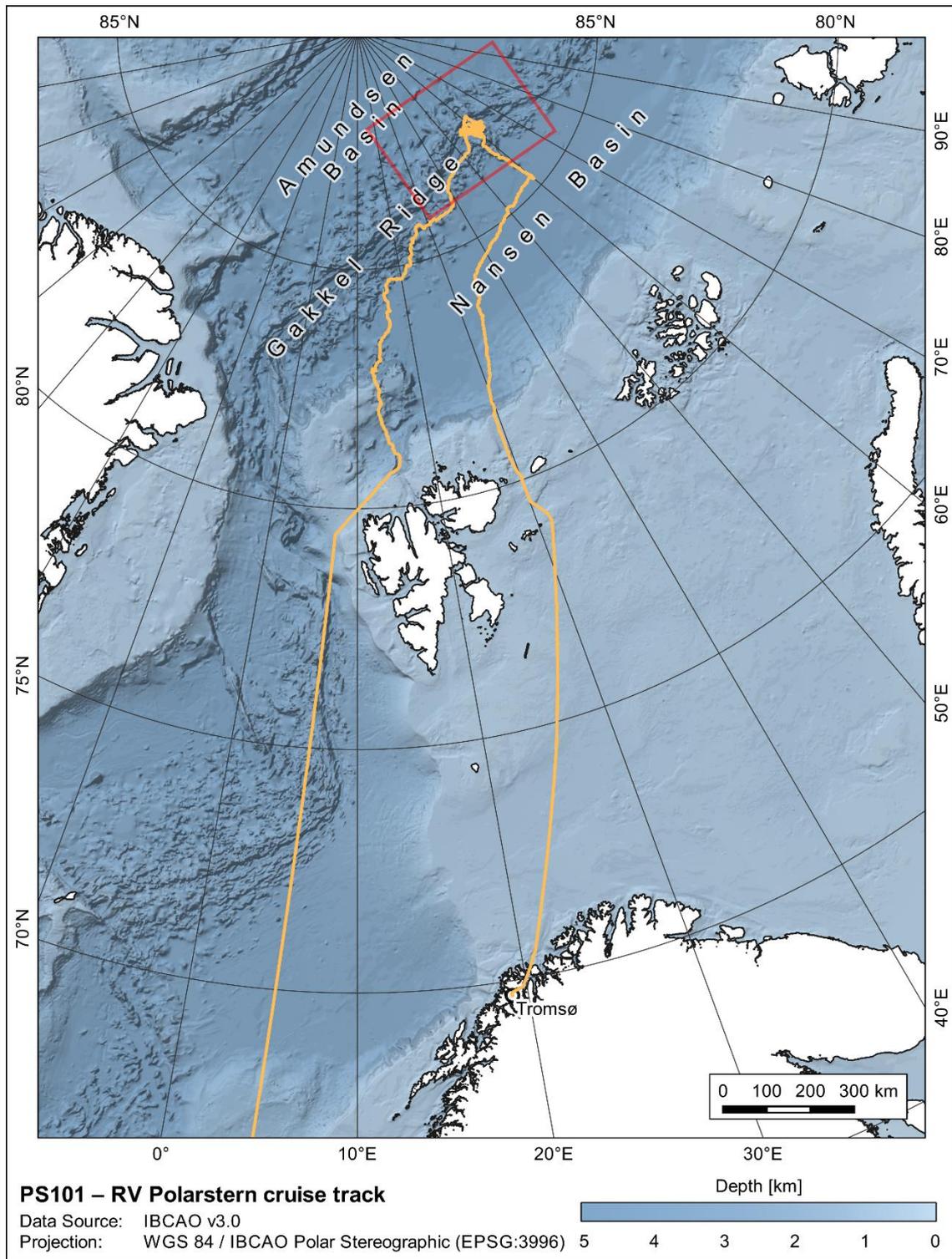
Figure 3-1: PS101 – *RV Polarstern* cruise track. Red rectangle marks map extent of Figure 3-2, which shows the bathymetry of the Langseth Ridge. Bathymetry is from the International Bathymetric Chart of the Arctic (IBCAO, Version 3.0) (Jakobsson et al., 2012).
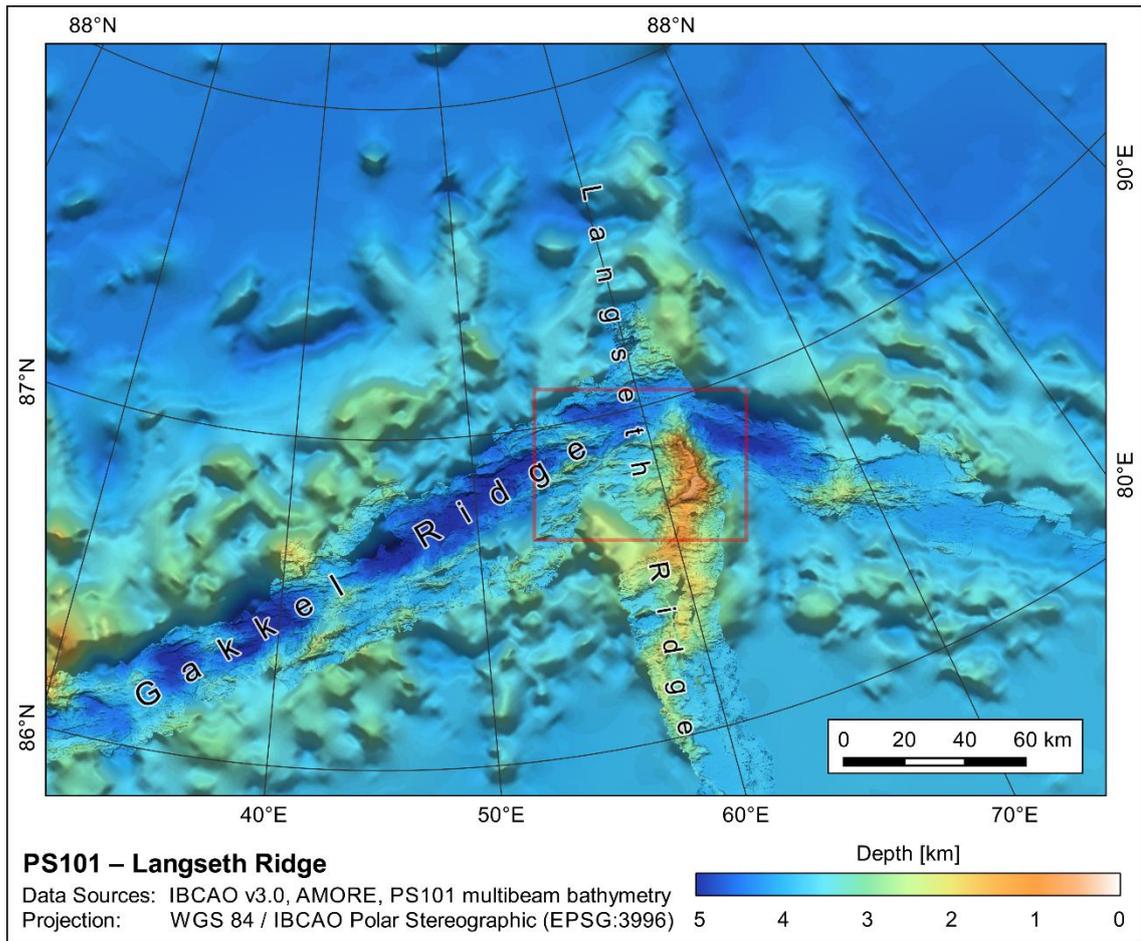
Figure 3-2: Langseth Ridge perpendicular to the ultra-slow spreading Gakkel Ridge. Red rectangle marks map extent of Figure 3-3, which shows the main research area of PS101. Bathymetry is from IBCAO (Jakobsson et al., 2012), higher resolution multibeam bathymetry was conducted during AMORE (Gauger et al., 2002) and PS101 (Dorschel & Jensen, 2017).

The highest elevation to the surrounding basin is reached at 86°42'N 61°8'E on the Karasik Seamount summit (1.5 km southwest of the proposed GEBCO location). Rising up to 585 m water depth, Karasik marks the shallowest feature in the Eurasian Basin (Cochran et al., 2003; Boetius & Purser, 2017). The seamount was first surveyed by a swath bathymetry system during the AMORE cruise and later surveyed and sampled during ARK-XXVI/3 (PS78) in 2011 (Schauer, 2012). After the initial survey, Karasik was assumed to be one individual seamount. In the new swath bathymetry from PS101, three individual peaks could be identified on the higher mountain range of the Langseth Ridge (Figure 3-3). At the time of writing, the naming of the two additional peaks is in progress; here they are given unofficial names for identification purposes.

The Central Mount, located at 86°48'N 61°55'E, rises gradually from 3300 m up to 723 m depth on the western flank and drops down to 4500 m on the steeper eastern flank. The Central Mount is separated from the Karasik summit by a saddle structure with depths around 1100 m.

The Northern Mount is located at 86°52'N 61°34'E just on the tip of the mountain chain before it descents northwards into the Gakkel Ridge rift valley. Its shallowest point has a depth of 627 m below sea level and the flank structures are similar to the Central Mount.

These three seamounts were the main study area during PS101. Another area of particular interest was a deeper nearby seamount, temporarily called Vent Mount (3045 m depth, 86°57'N, 55°45'E), which showed signs of active hydrothermal venting during earlier research cruises (Edmonds et al., 2003; Schauer, 2012).
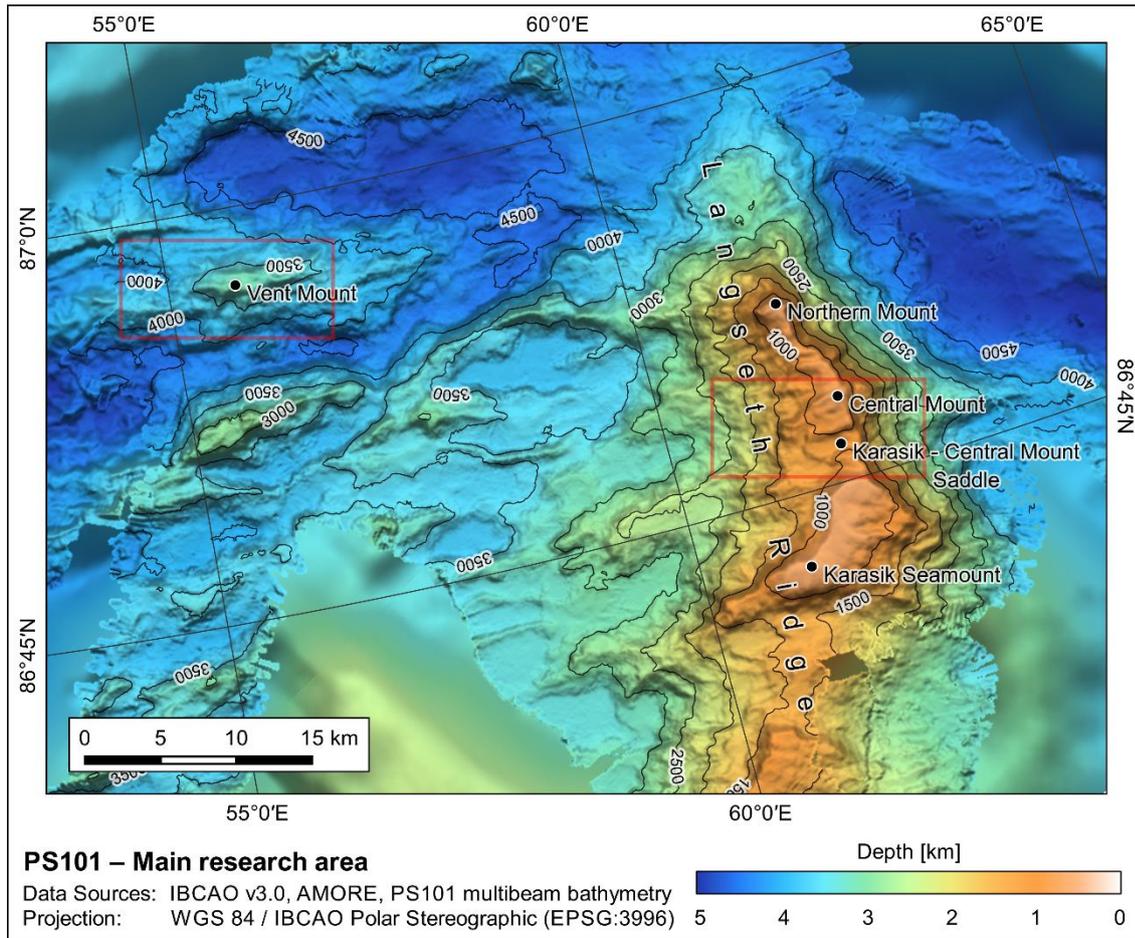
Figure 3-3: PS101 – Main research area on the Langseth Ridge. Red rectangles mark map extents of Figure 3-19 and Figure 3-20, which show the locations of the sample areas described in chapter 3.4. Background bathymetry is from IBCAO (Jakobsson et al., 2012), higher resolution multibeam bathymetry was conducted during AMORE (Gauger et al., 2002) and PS101 (Dorschel & Jensen, 2017).

3.2 Habitat Characteristics

The flanks of the surveyed seamounts on the Langseth ridge show steep and complex terrain while the summits are usually level. This topographic mixture promised a high variety of seafloor characteristics throughout the different OFOBS dives. During PS101, 13 successful OFOBS dives were conducted in various depths over the seamounts of the Langseth Ridge and the adjacent Vent Mount. The dives were planned in order to cover most of the different types of habitats within the research area. Being part of a mid-ocean ridge system, it was expected to find evidence for volcanic activities during seafloor investigation. Additionally, earlier studies recovered box corer samples of sponge mats and tubeworms on the Karasik crest (Schauer, 2012), which were assumed to cover most of the flatter areas of the summits. This section will give a brief overview of the observed habitat types and their geological and biological characteristics. All used figures are still images taken with the OFOBS camera during PS101. The full image dataset is available in the scientific data warehouse PANGAEA, referenced as Purser et al. (2017). Raw USBL tracks of all OFOBS dives during PS101 are also available in PANGAEA (Boetius & Roessler, 2016).

Langseth Ridge summits

The Karasik summit was investigated during OFOBS dive PS101/089-1 and revealed an almost closed cover of Geodia sponges and mats of sponge spicules (Figure 3-4). In the northern section of the dive, breaks in the sponge cover showed a thick layer of dead tubeworm tubes and occasional fields with sand and pebbles.

Central Mount was surveyed during OFOBS dive PS101/100-1 and parts of PS101/169-1, where the latter also covered the saddle area between the Karasik summit and the Central Mount. While the general impression was very similar to the observations on Karasik, the sponge abundance was slightly lower and more of the layer of dead tubeworms was visible (Figure 3-5) as well as stretches of sand and stones (Figure 3-6).

OFOBS dive PS101/120-1 covered parts of the western slope, the crest and the eastern flank of the Northern Mount. The crest looked similar to the Central Mount summit with high sponge abundance and mats of dead tubeworms. The Northern Mount summit however showed deep fissures in the East-West direction, occasionally breaking the sponge covers (Figure 3-7). The flanks on the other hand are built up with steep rocky slopes and near-vertical cliffs (Figure 3-8). Basalt outcrops and older lava flow structures covered with thin sediment layers dominate the area while sponge occurrence is reduced to occasional white glass sponges sitting on larger basalt lumps (Figure 3-9).
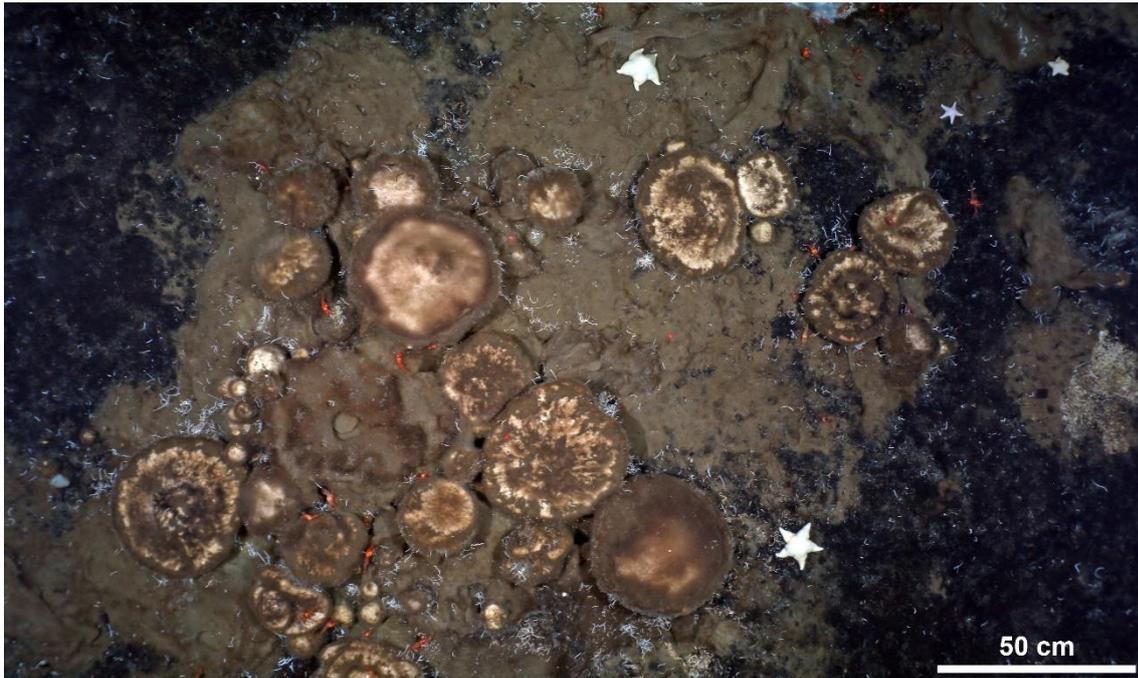
Figure 3-4: PS101/089-1, Karasik Seamount summit. Seafloor is almost totally covered with living Geodia sponges (brown, round lumps) and sponge spicules (brown mat). Occasional breaks reveal a thick layer of dead tubeworms (black mats, lower right and upper left corner). Crustaceans and Cushion Stars feed on the sponges. Scale bars in raw photographs are referenced to the laser dots in the image center and do not take perspective into account. (Purser et al., 2017)

Figure 3-5: PS101/100-1, Central Mount summit. Coverage of sponges and spicules is lesser, compared to the Karasik crest. Layer of dead tubeworms is visible more often. (Purser et al., 2017)
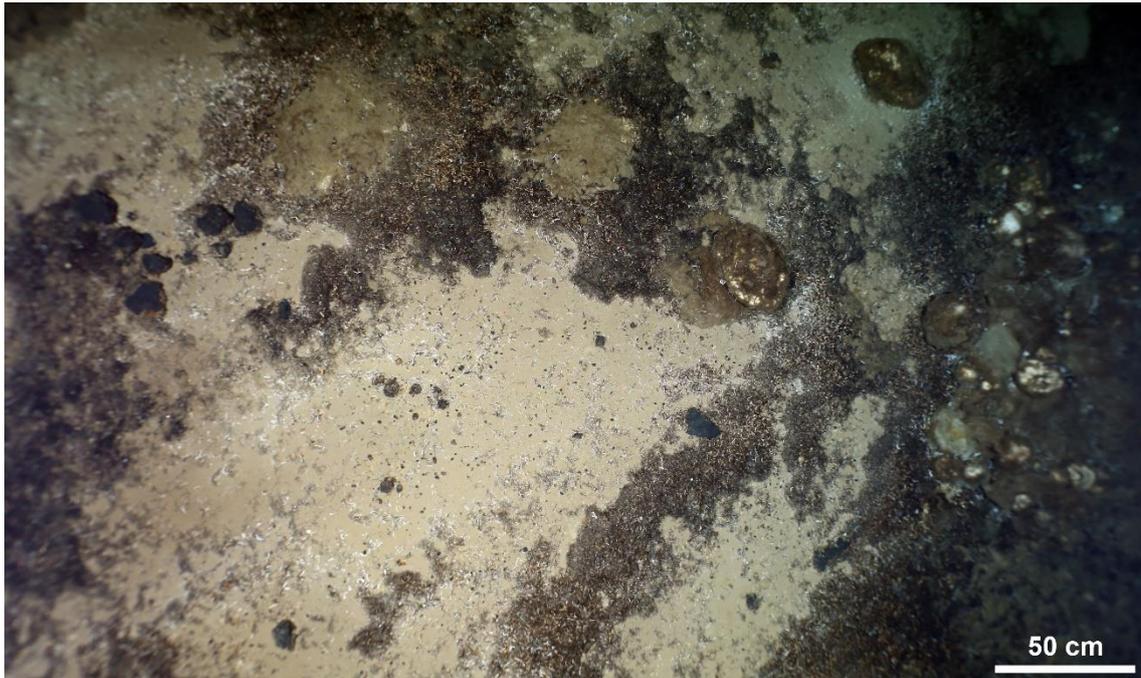
Figure 3-6: PS101/169-1, Central Mount summit. Coverage of sponges and spicules is lesser, compared to the Karasik crest. Occasional fields of sand with rocks and pebbles are visible. (Purser et al., 2017)
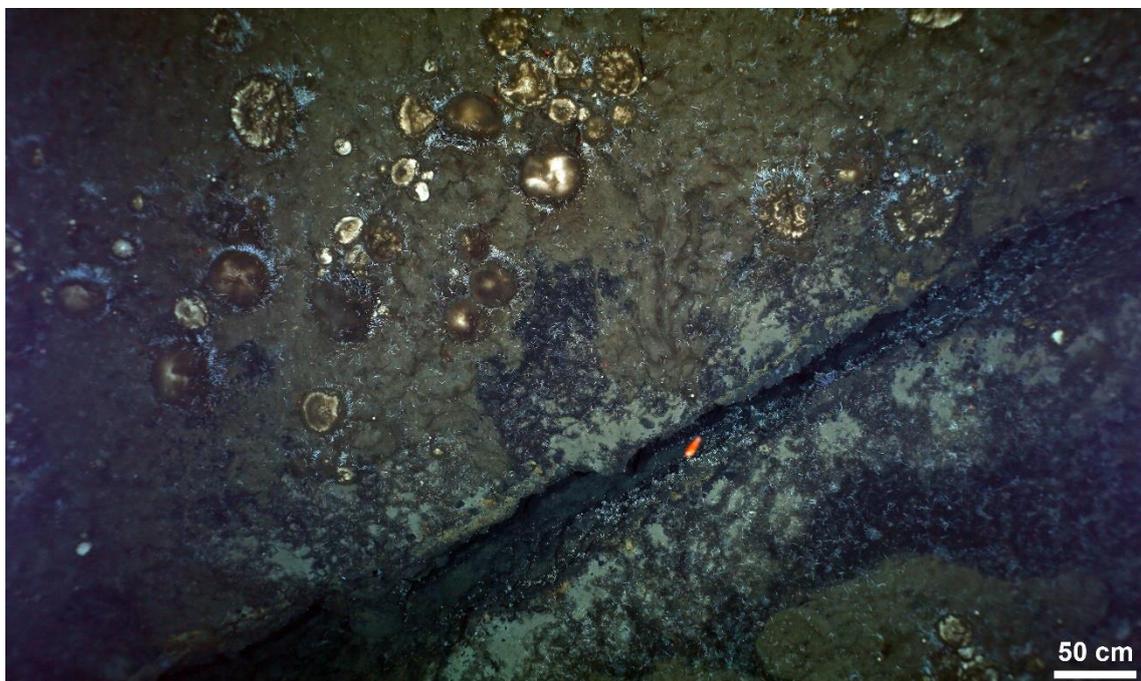
Figure 3-7: PS101/120-1, Northern Mount summit. Coverage of sponges and spicules is similar to the Central Mount crest. Deep fissures break the sponge cover from time to time. (Purser et al., 2017)

Figure 3-8: PS101/120-1, Northern Mount slopes. The flanks show steep rock-faced terrain with basalt outcrops and thin sediment coverage. (Purser et al., 2017)
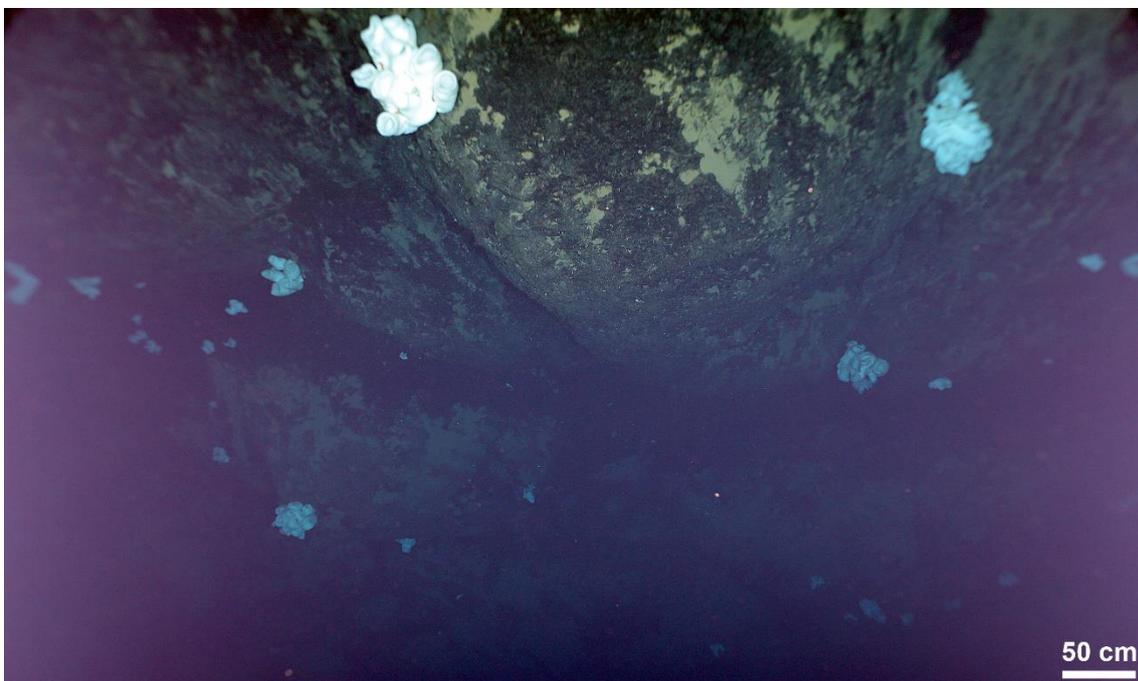
Figure 3-9: PS101/120-1, Northern Mount slopes. Occasional glass sponges sitting on basalt outcrops along the steep flanks of the seamount. (Purser et al., 2017)

Saddle

The saddle between Karasik and Central mount was investigated during OFOBS dive PS101/169-1. Close to the steep rock-faced slopes of the mounts, the saddle consists of rocky steps creating smaller plateaus inhabited by the familiar Geodia sponges (Figure 3-10). At a depth of ~1000 m the sponge abundance was lower than on the shallower surrounding summits and focused onto smaller rocky outcrops. The thick layer of living sponges and sponge spicules was replaced by larger sediment fields with rocks and pebbles (Figure 3-11).

Vent Mount

Physical oceanography studies during PS101 and earlier cruises showed strong reproducible plume signals in the water column over the Vent Mount indicating active hydrothermal venting on the seamount. Tow-yo casts with the Conductivity-Temperature-Depth (CTD) probe (lowering and heaving the instrument in a seesaw manner while the ship is drifting) were conducted to record water column properties in order to map the hydrothermal plume and pinpoint the most likely position of the vent on the seafloor (Boetius & Purser, 2017).

On the Vent Mount a total of eight OFOBS dives were conducted during PS101, with the goal of obtaining a detailed impression of the habitat. The dives covered the majority of the seamount navigating in various directions, targeting the area determined by the oceanographic investigations, and gave consistent results about the seafloor characteristics.

Figure 3-10: PS101/169-1, Karasik – Central Mount saddle slopes. Sponge abundance is isolated to rock-formed steps, as Geodia does not seem to inhabit steeper terrain. (Purser et al., 2017)
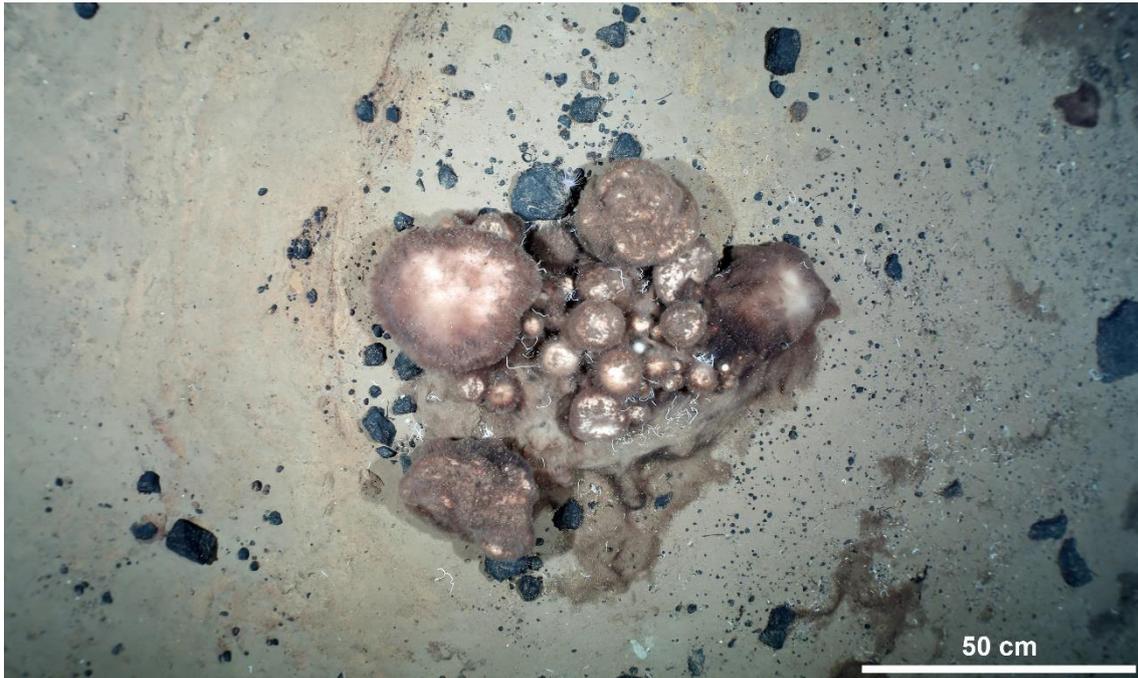
Figure 3-11: PS101/169-1, Karasik – Central Mount saddle flats. The deeper habitats (~1000 m) showed larger fields of sand with rocks and pebbles. Sponges could be seen mostly on smaller rocky outcrops. (Purser et al., 2017)

Figure 3-12: PS101/229-1, Vent Mount summit. The crest of the seamount, entirely covered with pillow basalts, mostly fresh pillows piled up into steep aggregations, and covered with a thin layer of sedimented material. (Purser et al., 2017)

The Vent Mount is almost entirely covered with pillow basalts in different stages of erosion. On the peak, larger and fresher pillows could be observed, covered with only a thin layer of sediment, and accumulated into steep aggregations (Figure 3-12).

Heading northwards from the peak, the terrain slopes down in terrace-like structures. The seafloor covers transition from fresh pillows over broken up pieces of pillow lava (Figure 3-13) to fully sedimented areas with occasional rocks protruding from the sand and gravel (Figure 3-14).

At a couple of locations along the northern flank of the Vent Mount, smaller chimney structures could be observed (Figure 3-15). Those observations could often be associated with local temperature anomalies measured by attached MTL & MAPR sensors (see chapter 2.1.5). In the vicinity of those chimneys, small fissures, discolored sediments, and hydrothermal precipitation were found (Figure 3-16).

The foot of the seamount is entirely covered with volcanic talus; fragmented pillows tumbled from its steep slopes and accumulated in the Gakkel Ridge rift valley (Figure 3-17).

Figure 3-13: PS101/135-1, Vent Mount slopes. Terrace-like formations on the northern slope covered with broken up pillow lava. (Purser et al., 2017)
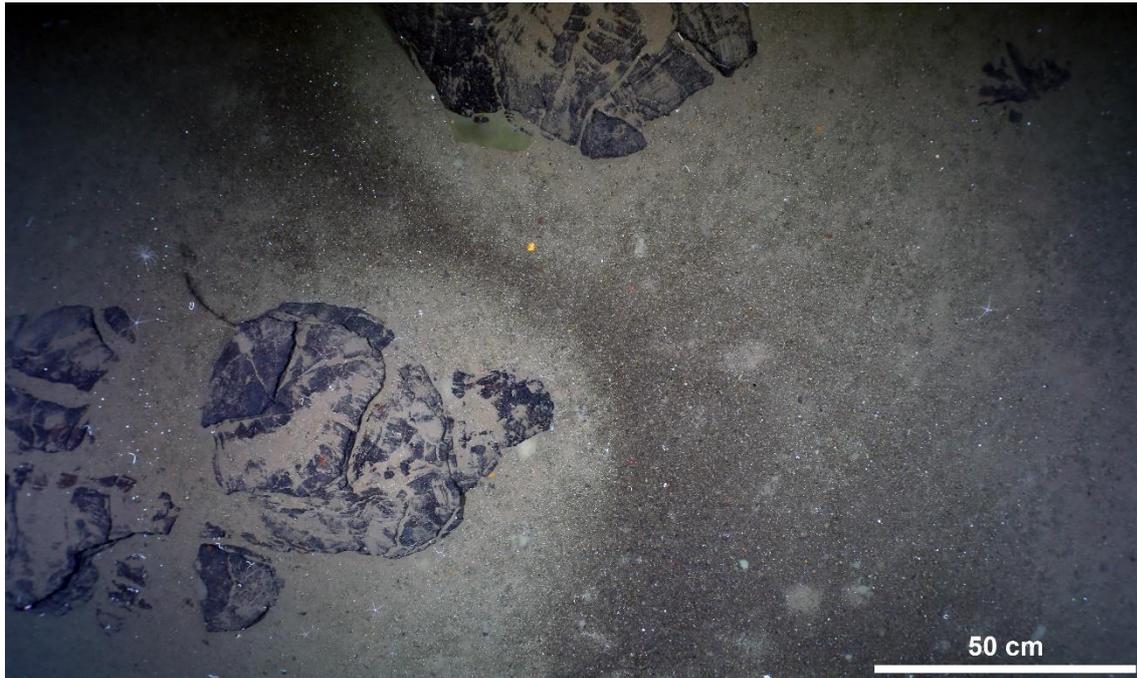
Figure 3-14: PS101/179-1, Vent Mount slopes. Deeper terraces revealed large fields of sand and gravel with isolated rocks partly buried in the sediment. (Purser et al., 2017)
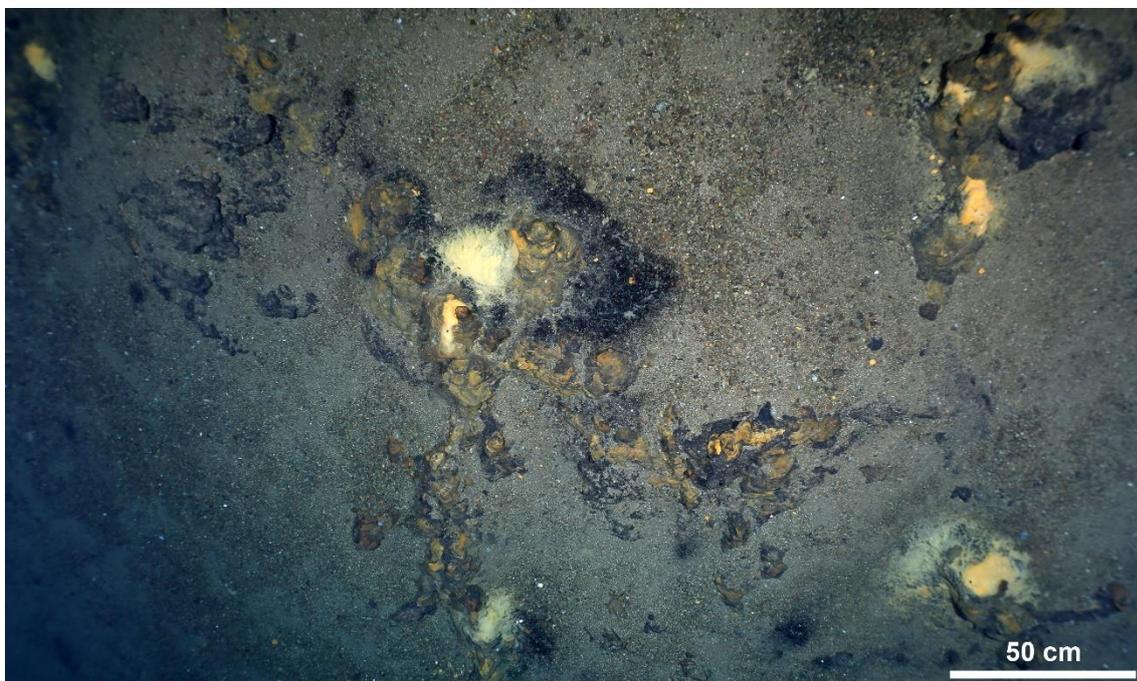
Figure 3-15: PS101/179-1, Vent Mount slopes. Smaller hydrothermal chimneys were found on the northern flank of the seamount. (Purser et al., 2017)

Figure 3-16: (left) PS101/179-1 & (right) PS101/229-1, Vent Mount slopes. Observations of chimneys could usually be associated with discolorations on sediments and rocks as well as hydrothermal precipitates. (Purser et al., 2017)
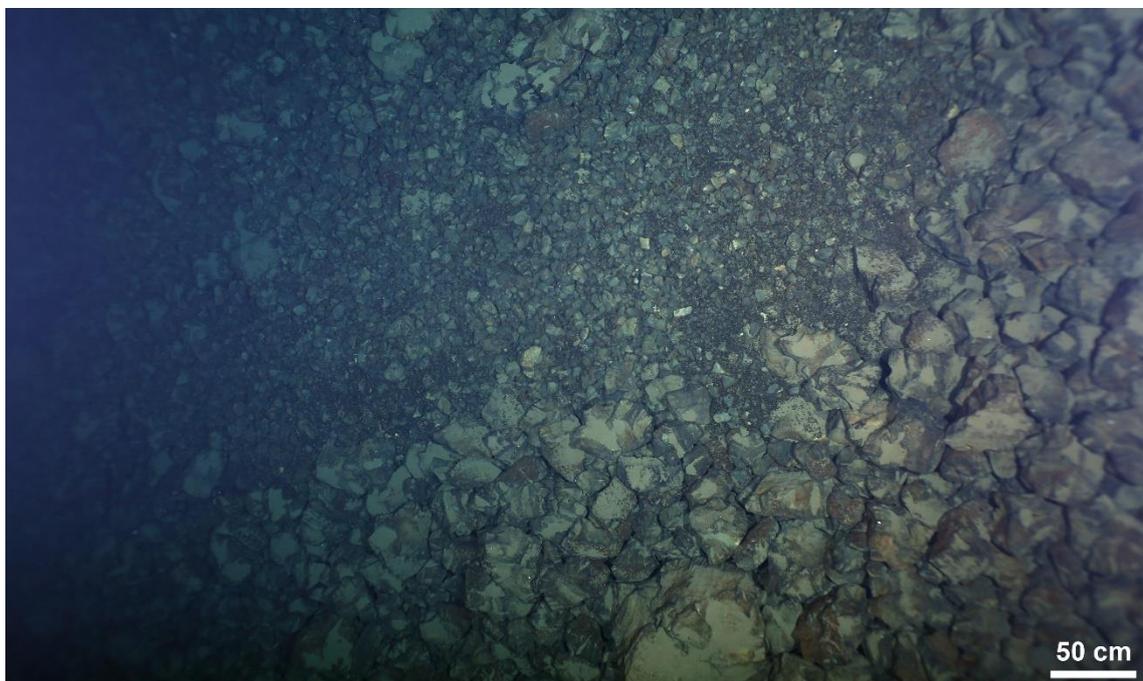
Figure 3-17: PS101/179-1, Vent Mount foot. Basalt talus, accumulated on the foot of the seamount, covers the seafloor entirely. (Purser et al., 2017)

3.3 Challenges during Surveys

OFOBS surveys during PS101 were challenging in some ways due to different environmental circumstances. As these factors greatly influence the data quality, they should briefly be introduced in this chapter.

First to be mentioned are the sea ice conditions. The PS101 research area on the Langseth Ridge, at latitudes of 86°40'N and higher, is situated below full ice cover throughout most of the year. Figure 3-18 shows the sea ice conditions over the Karasik Seamount on October 6th, 2016. Sea ice influences the OFOBS operation in certain ways. Preferably, the OFOBS is operated over the side crane to reduce the heave effects created by the ships pitch motion. However, since ice floes push alongside the hull, damage to the cable, or even loss of the vehicle, is highly possible. As a closed sea ice cover successfully dampens any water waves, OFOBS could mainly be operated over the A-frame at the stern of *Polarstern* during PS101. The propeller wash keeps ice floes away from the cable and with looser or thinner ice cover, it is possible to actively steer the ship instead of relying on ice drift speed and direction. However, even *Polarstern* can, at times, collide with ice floes too thick to break initially and backing and ramming is too risky with the tow cable behind the propeller. Therefore, sea ice highly influences and limits the ability to adjust the navigation of the towing vessel during deployment of any towed systems. Hence, track planning requires detailed preliminary examination of sea ice characteristics as well as drift direction and speed.

A more technical issue with sea ice is the influence on the quality of the navigation data of USBL tracked devices. The Posidonia USBL antenna on *RV Polarstern* is flush mounted into the ship's hull. To protect the acoustic transducers, a movable window is covering the antenna, which can be opened and closed. Whenever the ship is steaming in ice-covered waters, the protective window must be closed. The window is made from an acoustically near-transparent material, so USBL positions can still be received in this state. However, the quality is drastically reduced as will be shown in chapter 4.1.

Another key issue worth mentioning is the specific terrain in the survey area. As the previous chapter showed, the seafloor is dominated by steep cliffs and basalt aggregations. The crests of the Langseth Ridge seamounts are an exception, but the general character of seafloor during the PS101 OFOBS dives showed very rough terrain with large sudden depth changes and short wave local variations.

To achieve an even coverage, the OFOBS was usually driven with constant altitude over the seabed. Any noticeable topographic changes result in heaving or lowering the winch. Due to different hydrodynamic resistance pattern between the bow and the stern of the OFOBS subsea unit, heave motion causes pitch motion of the steel frame in the range of ±3°. Especially in the case of obstacle avoidance, these movements can be very sudden and can cause different motion artifacts in the sonar data when being picked up by the IMU with some delay.

Additionally, the close proximity to the seafloor reduces the quality of the USBL positioning system. Multipath effects caused by the near seafloor and acoustic shadow effects by steeper terrain structures create false readings and systematic outliers on the raw USBL position.

Figure 3-18: *RV Polarstern* in 100% ice cover above the Karasik Seamount summit. The darker patches in the lower right are young grey ice, the center part is mostly first-year ice, and the larger white patch stretching to the horizon is multi-year ice. Picture was taken during helicopter based sea ice observations on October 6th, 2016.

3.4 Sample Areas

Processing all 13 dives in this thesis was not feasible due to time constraints. To develop and illustrate the different processing workflows, a subset of the collected data was sufficient. Since the selected subset should cover certain characteristics to show strengths and weaknesses of the processing workflow, a set of parameters was created and the sample areas were selected such that all of these parameters are covered in most of their variations. The parameters were the following:

- Geographic location (Langseth Ridge, Vent Mount)
- Water depth (shallow crests, deeper slopes)
- Topographic structure (high variability, roughness, slopes, flat even terrain)
- Type of seafloor (pillow basalts, rocks, sand fields, sponge mats)
- Scientific features of interest (geological, biological, size, details)
- Flight height (steady, high variability)
- Quality variations of raw datasets (navigation, photographic parameters)

Based on these parameters, three sample areas were selected. The following section will outline the characteristics of the sample datasets.

Area A

The first sample is from dive PS101/169-1 on the saddle between Karasik Seamount and Central Mount. The seafloor in this area is covered with stretches of sand, occasional rocky outcrops, isolated sponge communities and sponge spicule mats. There are very little topographic variations and the flight height is comparatively steady around ~2 m. Due to the close distance, higher resolution images are to be expected from the stills camera. Without slopes, bigger rocks or any form of larger objects that might create acoustic shadows, the side scan image is expected to give an even ensonification over the whole swath, same as the resulting coverage of bathymetry data. Figure 3-19 shows the track of PS101/169-1, marking the position of area A along the dive. Table 3-1 summarizes the specifications of the sample area A subset.

Area A	
Dive number	PS101/169-1
Date, Time	2016-09-30, 21:33:54 – 21:46:03 UTC
Geographic location	Karasik – Central Mount Saddle
Start coordinates	86°46.34'N 61°50.41'E
End coordinates	86°46.47'N 61°49.91'E
Track length	245 m
Water depth	~1116 m
Topographic structure	Even flat terrain with only gradual depth variations
Seafloor coverage	Sand, rocks, pebbles, partial sponge coverage
Scientific features of interest	Biological: sponges and other megafauna
Flight height	1.5–2.5 m

Table 3-1: Specifications of sample area A
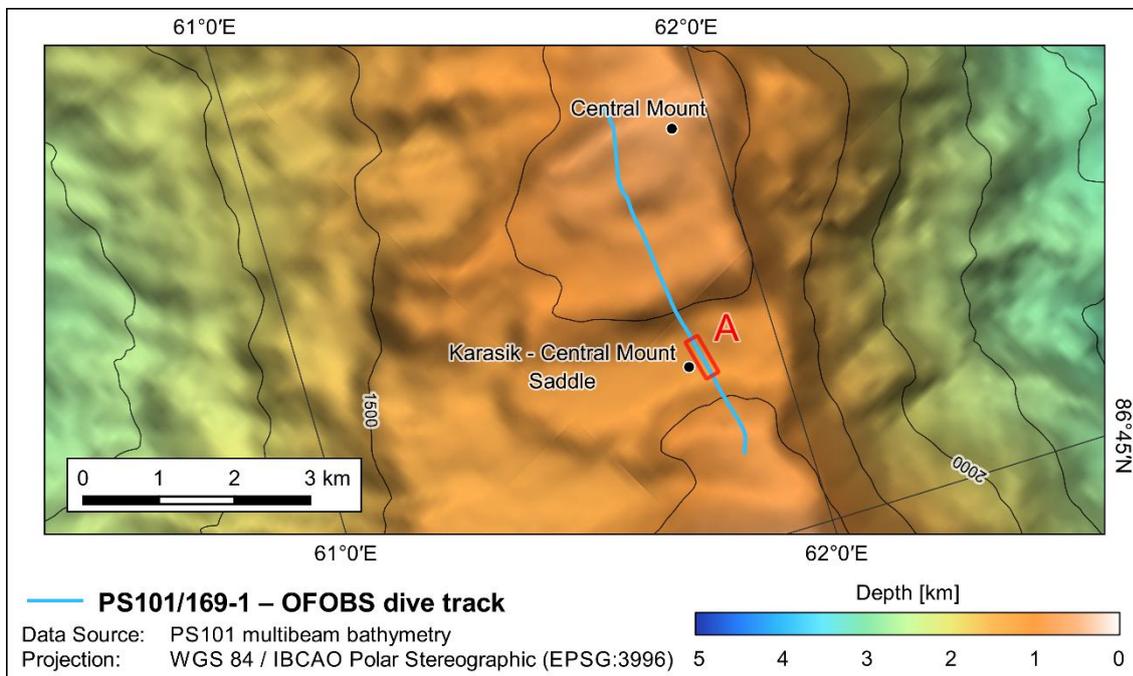
Figure 3-19: PS101/169-1 – OFOBS dive track. Red rectangle marks the location of sample area A. Bathymetry is from multibeam surveys, conducted during PS101 (Dorschel & Jensen, 2017).

Area B

The second sample dataset is from dive PS101/179-1 on the Vent Mount. Seafloor coverage consists of sand, pebbles and pillow basalts. The topographic variations are much higher than in area A. The sample starts with a flat area covered with sand, slightly inclining, passes a field with fresher pillow basalt lumps and rises up a slope covered with broken lava bits. Deep across-track fissures interrupt the flat sandy area at the beginning. Due to the wider range of flight height (3–6 m), higher variations in the data quality are to be expected, especially in terms of changes in lighting and image bottom resolution. The steeper terrain creates shadow effects on the sonar, resulting in a more uneven coverage both for the side scan and the bathymetry data. Table 3-2 summarizes the specifications of the sample area B subset. Figure 3-20 shows the track of PS101/179-1, marking the position of area B along the dive.

Area B	
Dive number	PS101/179-1
Date, Time	2016-10-03, 10:36:07 – 10:43:49 UTC
Geographic location	Vent Mount
Start coordinates	86°56.92'N 55°47.15'E
End coordinates	86°56.96'N 55°47.19'E
Track length	72 m
Water depth	3100–3140 m
Topographic structure	Higher variations in relief, sudden changes
Seafloor coverage	Sand, pebbles, pillow basalt
Scientific features of interest	Geological: deep fissures, fresh pillows
Flight height	3–6 m

Table 3-2: Specifications of sample area B

Area C

The last sample area is again from dive PS101/179-1, cutting across the northern flank of the Vent Mount. The seafloor in this area is mostly sand covered with some occasional rocky outcrops. The track passes a couple of steep rock-faced cliffs. Additionally, the center of the subset covers a field of hydrothermal chimneys. Again due to the high variations in both terrain and flight height, the data quality will show very changing results, both on the visual and the acoustic sensors. The cliff areas especially negatively influence the capabilities of the sonar due to acoustic shadows, multipath and scattering. Table 3-3 summarizes the specifications of the sample area C subset. Figure 3-20 shows the track of PS101/179-1, marking the position of area C along the dive.

Area C	
Dive number	PS101/179-1
Date, Time	2016-10-03, 21:33:54 – 21:46:03 UTC
Geographic location	Vent Mount
Start coordinates	86°57.53'N 55°43.68'E
End coordinates	86°57.61'N 55°43.09'E
Track length	160 m
Water depth	3145–3180 m
Topographic structure	High variations in relief, steep cliffs, sudden changes
Seafloor coverage	sand, rocks, pebbles, rocky cliffs, chimneys
Scientific features of interest	Geological: hydrothermal chimneys, discolorations and hydrothermal precipitates Biological: fauna associated with hydrothermal venting
Flight height	1.8–10 m

Table 3-3: Specifications of sample area C
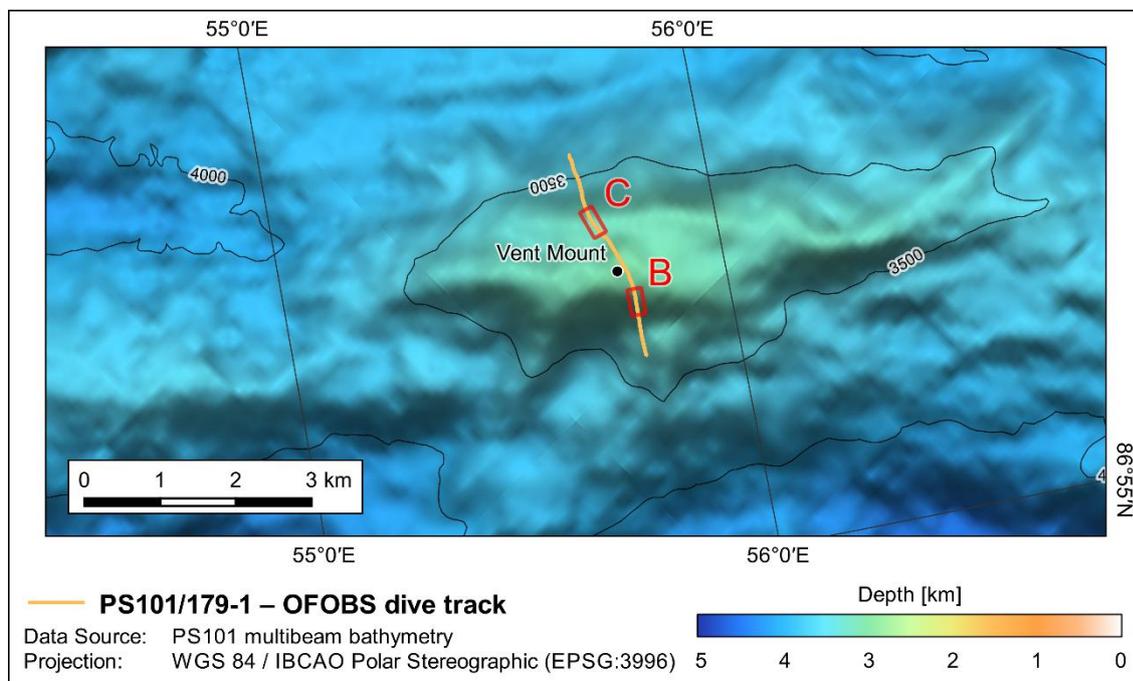
Figure 3-20: PS101/179-1 – OFOBS dive track. Red rectangles mark the locations of sample areas B and C. Bathymetry is from multibeam surveys, conducted during PS101 (Dorschel & Jensen, 2017).

4 Raw Data Characteristics

As presented above, different datasets are collected during OFOBS dives. These different datasets require different processing workflows to be combined in a multilayer habitat-mapping result. The following section describes the raw data characteristics of the individual sensors. The different processing steps will be presented in chapter 5.

4.1 Navigation Data

Navigation data was logged in multiple places and in different formats. The iXBlue USBL-Box logs NMEA strings (ASCII) of the raw USBL tracked positions of the subsea transponder. The recurrence interval for the position measurements were set to a depth-dependent value to avoid false readings from multiple pings in the water column. A typical update rate for the OFOBS dives was 5–8 seconds.

The Kalman filtered PHINS navigation solution is streamed directly into the sonar's processing unit together with the attitude measurements, and is logged within the EdgeTech JSF file format. Additionally, PHINS navigation and attitude data is broadcasted over the network in the PHINS STANDARD protocol (ASCII) with a rate of 20 Hz, and is recorded on a topside PC for further analysis.

At a depth of ~3000 m and a vessel speed of ~0.5 knots, the OFOBS subsea unit is at a slant range of ~3100 m to the USBL antenna. The resulting raw USBL position has a nominal accuracy of less than 6.2 m at a rate of one measurement every 8 seconds. This is insufficient for microbathymetric measurements with ping rates of up to 8 Hz. The PHINS, on the other hand, provides a much higher data rate and fills the navigation between acoustic interrogations with inertial measurements. As the INS receives the initial positioning input for its alignment from the USBL, the global position accuracy will not improve considerably compared to the raw USBL position, but the higher update rate and the ability to filter outliers from external inputs improves the overall navigation precision.

The USBL data quality, as mentioned above, is greatly reduced during surveys in sea ice due to the ice protective window, as well as during surveys in steep and rough terrain. Even though the PHINS internal filters are supposed to smooth USBL positioning by a factor of three and more (IXSEA (Ed.), 2010b), the USBL outliers (especially the successive ones) still highly influence the outcome of the navigation solution. The selected sample areas nicely illustrate the variations in navigation data quality. Area A (Figure 4-1) was surveyed in flat terrain without many acoustic obstacles at a relatively shallow depth. During survey, the ice protective window of the USBL antenna was open, as dive PS101/169-1 occurred mostly in ice drift. The resulting USBL data is relatively smooth and smaller outliers are filtered by the Kalman filter. Contrastingly, Area B
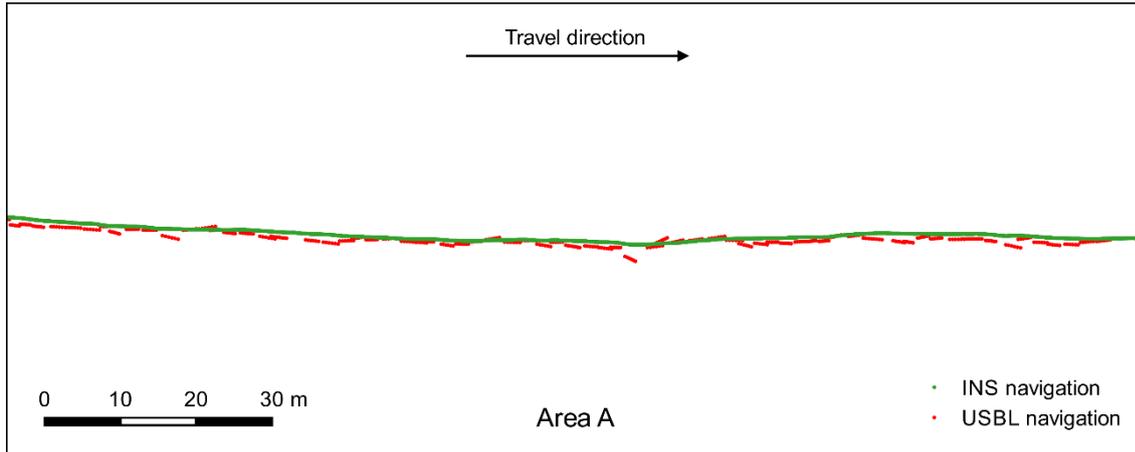
Figure 4-1: Navigation sample of area A, dive PS101/169-1. On the flat seabed of the Karasik – Central Mount saddle, the raw USBL data is very steady and smaller outliers are rejected and smoothed over by the PHINS Kalman filter.
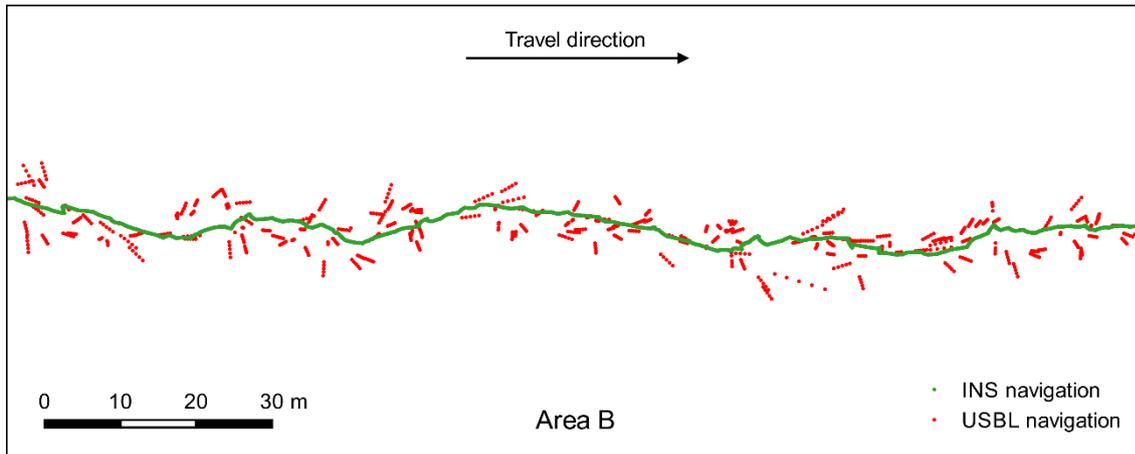
Figure 4-2: Navigation sample of area B, dive PS101/179-1. On the steep southern flank of the Vent Mount, multipath effects and acoustic shadows obscure the USBL measurements and the PHINS navigation solution deteriorates drastically.

(Figure 4-2) and C (Figure 4-3) are embedded in very rough topography. During PS101/179-1 the USBL ice protective window was closed due to active steaming. The USBL soundings show very large and partly systematic/successive outliers on both sides of the track, resulting in a more unstable navigation solution on the INS. Usually, due to the inert nature of deep-towed systems, the OFOBS has a very steady and smooth track line, as it can be observed in the video stream. Sudden movements away from the linear track can most certainly be considered as outliers. Effects of navigation artifacts on the bathymetric survey data as well as an adjustment process for navigation improvements will be shown in section 5.2.
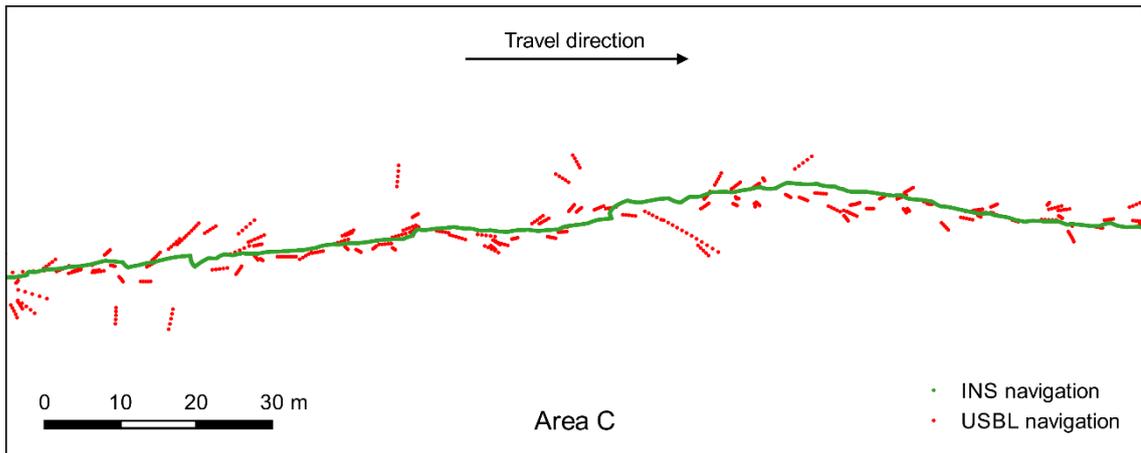
Figure 4-3: Navigation sample of area C, dive PS101/179-1. The overall navigation data quality is similar to the one of area B.

4.2 Imagery

The stills camera is operated within the iSiTEC OFOS software package. As mentioned, images are taken every 20 seconds triggered by a timer, and any time when manually triggered by the operator. The still images vary significantly in brightness and hue, mostly depending on flight height and the resulting lighting conditions (Figure 4-4). The low dynamic range of the JPG files limits the scope for brightening and color corrections in post processing. Nonetheless, the quality of the majority of images taken during PS101 is more than sufficient for the different purposes (visual interpretation, photogrammetric reconstruction, habitat representation). Some examples of the images can be seen in chapter 3.2. Additionally, Figure 4-5 shows another image sample, both in its total extend, and an unscaled section of the image.

The video stream is recorded constantly throughout the whole dive by a *RONIN HD-SDI* video recorder in 25 fps. The video itself is great for online observations during the dive. However, to be used for photogrammetric reconstruction the individual frames need to be extracted from the video. To assure sufficient overlap between the extracted frames, the extraction framerate needs to be adjusted to the survey speed and altitude. Highly complex terrain requires a denser coverage than flat terrain with less explicit objects. At the same time, it is a tradeoff with processing resources as a higher extracted framerate results in a bigger data volume and longer processing times.

Figure 4-6 illustrates the resolution ratio between still images and extracted video frame, and shows an example for the video frame quality. Still images are taken with a flash while the lower lighting in the video has to be compensated with higher exposure/sensitivity. This results in motion blur and washed out edges (clearly visible in the representation of laser dots in Figure 4-5 compared to Figure 4-6). In order to reduce the load on the network bandwidth and hard drive
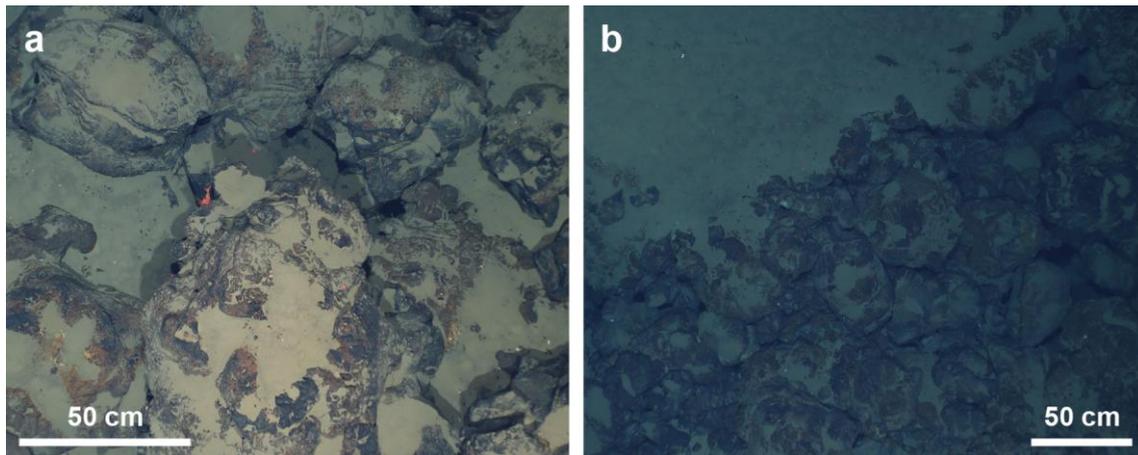
Figure 4-4: Image samples from dive PS101/179-1, area B. The images where taken ~20 m apart and show seafloor of very similar character. (a) was taken from an altitude of 2.5 m and (b) from 5 m. With increasing altitude, the absorption and scattering levels increase, which results in a generally darker image. Additionally, the red and yellow spectrum of electromagnetic waves (~550–800 nm) has higher absorption levels than blue and green (~400–550 nm) (Nocerino et al., 2016), leaving a bluish hue in (b) due to the overall longer traveled distance. (Purser et al., 2017)
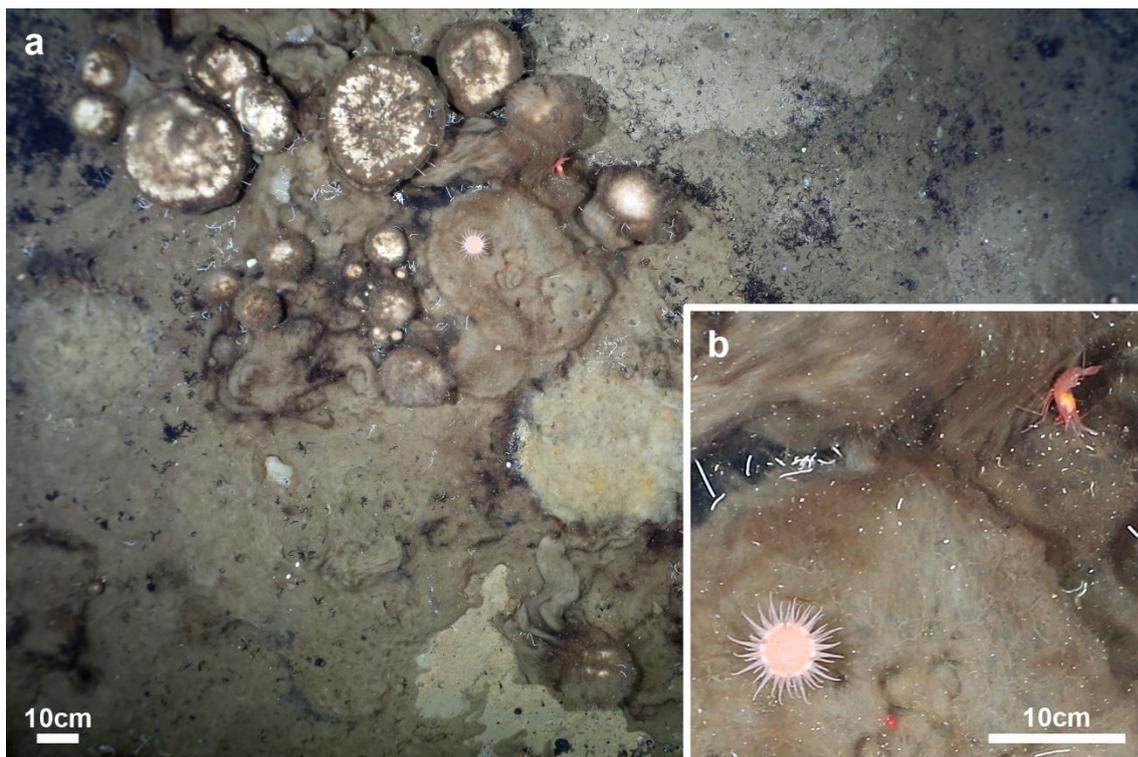
Figure 4-5: Image samples from dive PS101/169-1, area A. (a) Image in its full extend, (b) unscaled subsection of (a) at 300 ppi. The images is taken from an altitude of 2 m, resulting in an average pixel size of 0.5mm. Even smaller biological features like the tubeworm tubes can be recognized in great detail. (Purser et al., 2017)

storage, video files are compressed during recording (codec: *Apple ProRes 422 LT*), which adds additional quality loss.

While being of much lower overall quality compared to the still images, the video frames have one important advantage. With a constant framerate of 25 fps they assure complete visual coverage and are therefore crucial for the 3D reconstruction and to fill the gaps between still images.

Still images are timestamped on the fly via the 1 Hz Posidonia data stream, which is synchronized to the ships GNSS based timeserver (UTC). Additionally they are fitted with an extensive metadata file containing, besides timestamp and USBL position, all available camera parameters. The video frame grabs however do not contain any time code and have to be time referenced in post processing, as described in section 5.1.2. Table 4-1 shows some quantitative information on images and video frames used for the three sample areas.
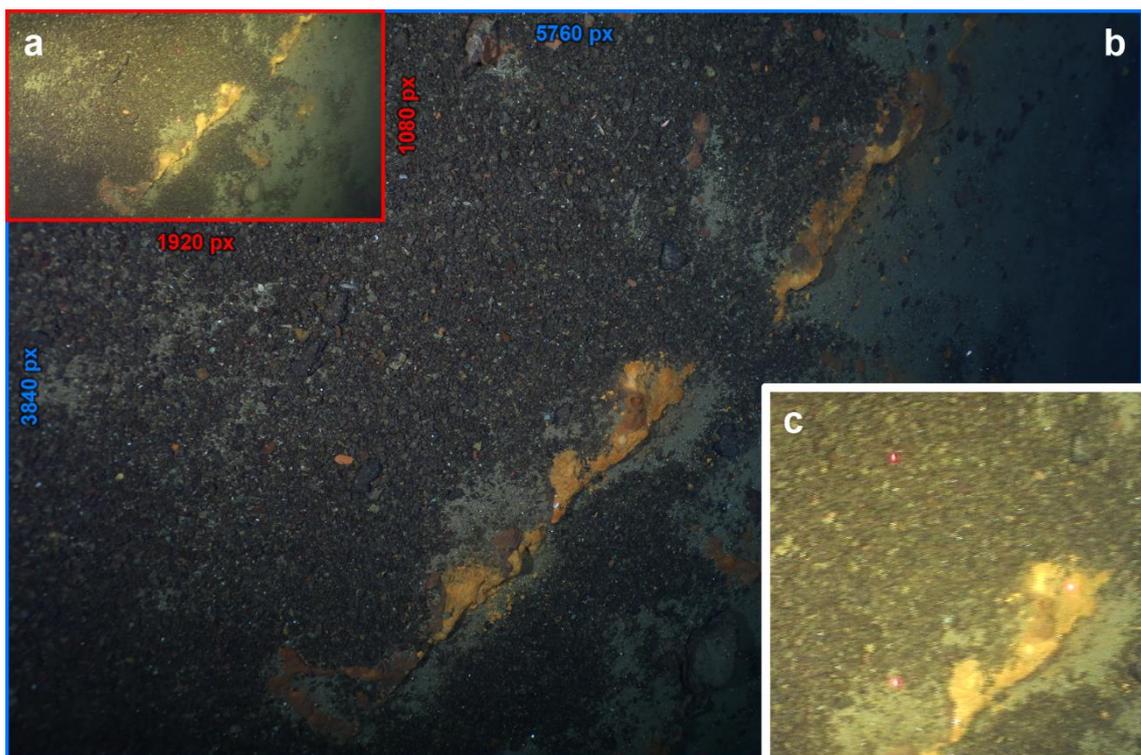
Figure 4-6: Image and video frame samples from dive PS101/179-1, area C. (a) shows a video frame recorded at the same time as the still image (b). The size ratio between (a) and (b) illustrates the actual resolution ratio between still images and video frames. (c) shows an unscaled subsection of (a) at 300 ppi to illustrate image quality of the video frames. (Purser et al., 2017)

	Area A	Area B	Area C
Still images			
No. of timer synched images	35	23	30
No. of hotkey images	11	7	36
Average file size per image	7 MB	5 MB	7.3 MB
Total file size	328 MB	150 MB	483 MB
Video frames			
Extraction framerate	1 fps	2.5 fps	1.25 fps
No. of video frames	728	1176	850
Average file size per frame	502 kB	420 kB	500 kB
Total file size frames	357 MB	482 MB	416 MB

Table 4-1: Data volume of still images and video frames for the sample areas

4.3 Sonar Data

EdgeTech 2205 Multiphase Echosounder

The MPES is controlled with the *EdgeTech Discover Bathymetric* software. Discover visualizes the side scan data live in a waterfall display (Figure 4-7) and has some additional visualization features for the bathymetry data (Figure 4-8). The data is stored in the EdgeTech JSF file format that contains both side scan frequencies and the binned bathymetry solution. Waterfall images can be saved as continuous grabs (e.g. every 500 m of data) for rapid analysis after the dive.
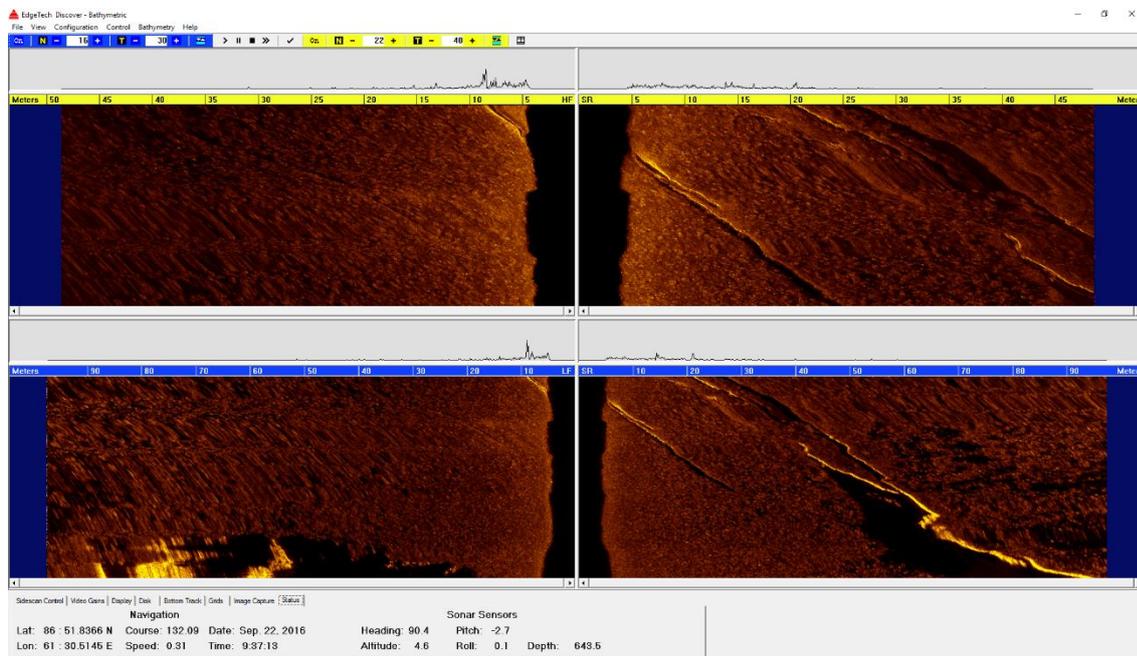
Figure 4-7: EdgeTech Discover Bathymetric – Main window. Side scan waterfall (upper: HF, lower: LF) showing across track fissures on the Northern Mount during dive PS101/120-1.
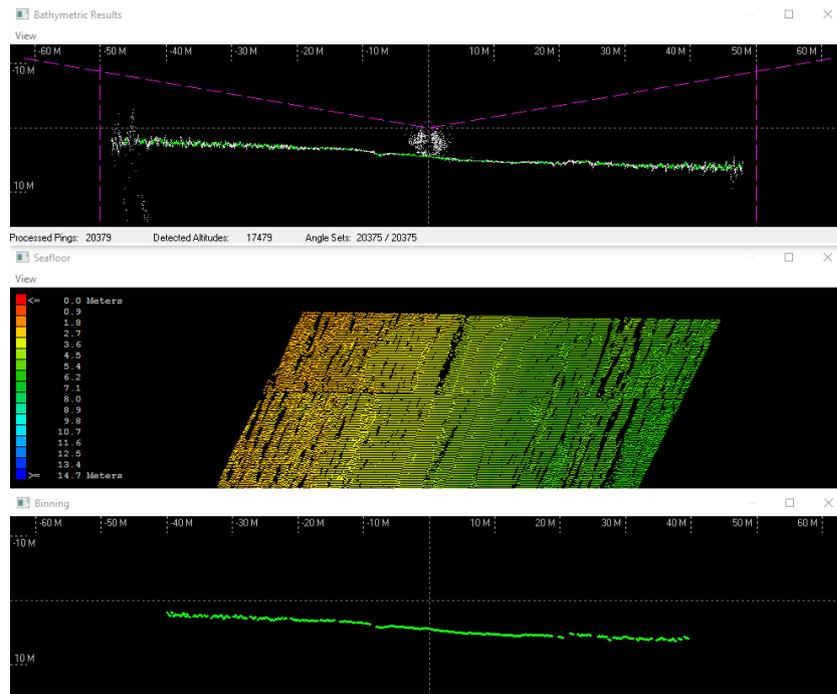
Figure 4-8: EdgeTech Discover Bathymetric – Bathymetry windows. (upper) Gates and filters, (middle) 3D seafloor waterfall, and (lower) binning results

Additional stave raw data files can be logged in order to replay files in post processing with different bathymetric binning and filtering parameters. As mentioned above, both attitude and position data is stored in the JSF files as well.

During the OFOBS dives throughout PS101, side scan data was collected with 100 m range on the LF, and 50 m on the HF. Longer ranges would be possible with the used system (see Table 2-1). However, with the comparatively low flight heights, data results beyond the set ranges are washed out and hardly usable since most of the energy is focused on closer ranges. Going for longer ranges would additionally reduce the ping rate, hence the data density.

The side scan sonar footprint changes with range both along and across track. While the along-track portion gets wider with increasing range, the across-track portion gets narrower (Lurton, 2004). For continuous wave signals, the across-track footprint depends on the pulse length. For frequency modulated signals, however, it is dependent on the (proprietary) signal processing (EdgeTech (Ed.), 2015a). Regarding personal correspondence with the manufacturer, the EdgeTech 2205 MPES produces reasonable bathymetric results with bin sizes of 10 cm and larger, with respect to the sonar footprint size within the typical PS101 survey setup. Following those recommendations, the bathymetry data was binned online with 10 cm equidistant spaced bins, in order to get the highest reasonable bathymetry resolution possible. With the maximum of 800 bins per ping, this results in an 80 m wide swath, 40 m to both sides of the vehicle. However, if needed, the recorded JSF stave files can be replayed in Discover Bathymetric with different parameters (equiangular, equidistant, bin size, range filter, etc.).

With the mentioned range settings, the 2205 sonar achieved ping rates of ~3.5 Hz for LF and ~7 Hz for HF. The recorded data volume comes down to approximately 17 MB/min for the binned JSF files and around 10 times as much for the raw stave files. All side scan and swath bathymetry data collected along OFOBS profiles during PS101 is archived and available in PANGAEA (Dreutter et al., 2017b).

BlueView M900-130 Forward Looking Sonar

The M900-130 FLS is controlled via the *BlueView ProViewer* software, which is recording the data in the SON format and gives a live representation of the sonar wedge (Figure 4-9). As mentioned earlier, the FLS is a very helpful tool for navigation purposes and obstacle avoidance. In the scientific sense of surveying, the data was recorded and archived post cruise. However, it was not processed for any further results within the scope of this thesis. A recommendation for future use of the data is given in chapter 7.4. All FLS data collected along OFOBS profiles during PS101 is archived and available in PANGAEA (Dreutter et al., 2017a).
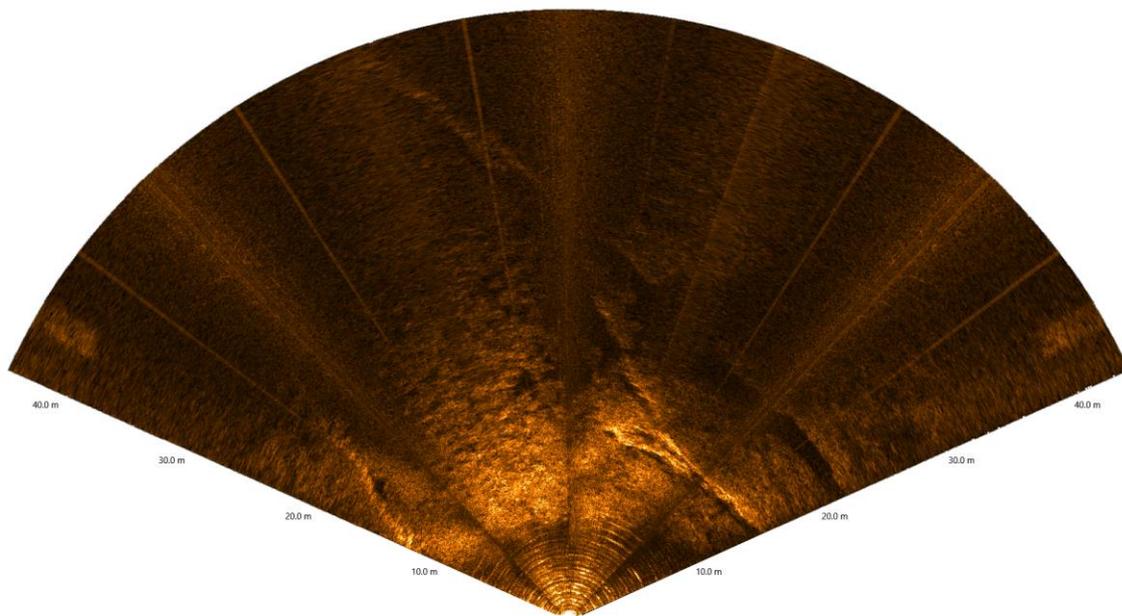
Figure 4-9: Representation of the FLS acoustic image wedge in BlueView ProViewer showing across track fissures on the Northern Mount during dive PS101/120-1. (Dreutter et al., 2017a)

5 Data Processing Workflow

The following section will go into detail on the workflow, developed to process the raw data in order to get a multilayer microbathymetric result.

Originally, the OFOBS was intended to conduct bathymetric surveys with its onboard sonar systems, while the optical data was meant for visual interpretation and statistical mapping, roughly georeferenced by the USBL position and the scaling lasers. However, throughout the experimental phase of the thesis, the optical datasets proved to be very valuable. Structure from Motion (SfM) techniques were investigated to align and georeference the imagery and to reconstruct 3D models of the captured seafloor. Combined processing approaches were incorporated in order to match the different datasets and to improve overall results. Especially due to the above mentioned harsh survey conditions, and the resulting inconsistencies in data quality, the multisensor approach showed its strengths.

The resulting workflow is not as straight forward as one might experience when working with ship-borne bathymetric survey data. It is, to a greater degree, an iterative process with the goal to achieve the best possible results from multiple data sources. An overview on the processing workflow is given in Figure 5-1. The individual subprocesses (colored in the diagram) will be explained in detail in the following subsections. The different resulting data products will be presented in chapter 6.
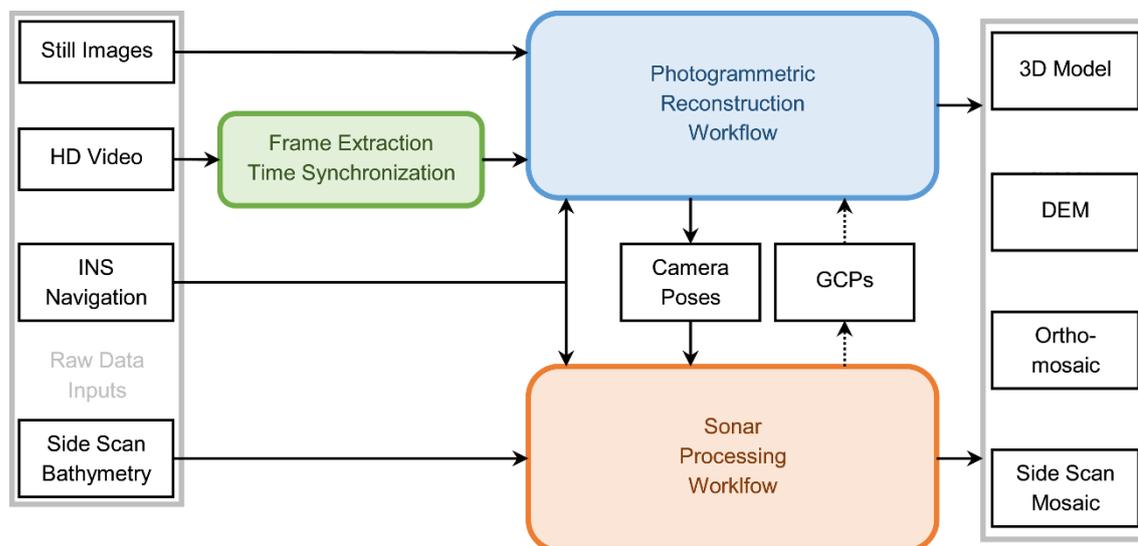
Figure 5-1: Data processing workflow – Overview

5.1 Photogrammetric Reconstruction

SfM techniques are widely used and well developed in land-based geodesy. Nowadays even low cost consumer grade sensors and small unmanned carrier platforms (e.g. aerial drones) are utilized to achieve reasonable photogrammetric results. Bundle adjustment algorithms allow for processing of large amounts of unstructured images to create up to city scale 3D models (Triggs et al., 2000). It proved to be a valuable tool for data mining of optically collected datasets of all sorts.

Underwater photogrammetry, however, is a field with a much smaller user group, but it is becoming more and more popular. Applications can be found in shallow waters as well as in the deep sea. Archeology uses photogrammetry to capture the current state of submerged objects of interest for further land-based studies as well as for digital conservation purposes (e.g. Zhukovsky et al., 2013; Balletti et al., 2015). Habitat mapping projects can utilize the technology to do inexpensive periodical resurveys of an area in order to monitor changes in biology (e.g. Pizarro et al., 2017). In the deep sea, photogrammetric surveys are conducted with unmanned vehicles for habitat mapping purposes (e.g. Kwasnitschka et al., 2016), or to do post dive virtual fieldwork on geological structures of interest, like outcrops (Kwasnitschka et al., 2013) or chimneys of black smokers (Sedlazeck et al., 2009).

Further research on the topic shows that photogrammetric applications under water have to overcome a few challenges that are inherently different to in-air applications. These issues are mostly with respect to image quality and the consistency of camera parameters. The main difference is the medium in which the survey is conducted. Water is much denser than air (~800 times), but more important, it is not as consistent as air (Nocerino et al., 2016). While pressure changes linearly with depth, density layers are forming in the water column due to changes in salinity and temperature or by currents of different origins. All the resulting density changes cause waves to refract at the interfaces. This and the wavelength dependent absorption of light in water leaves a high variability in overall photographic conditions.

While shallow water applications have advantages like the possibilities to do GNSS aided positioning of Ground Control Points (GCP) for higher position accuracy (e.g. Balletti et al., 2015; Pizarro et al., 2017), the optical environment is not consistent due to changing reflection pattern by the water surface waves and visibility is possibly limited due to turbidity (Menna et al., 2016). Artificial lighting conditions in the deep sea are usually more stable, hence resulting in more consistent images, but the survey accuracy solely depends on the subsea navigation data as accurate GNSS positioning of GCPs or the survey platform is impossible.

One thing both shallow and deep water applications have in common is the fact that underwater operations require water-tight pressure housings for the camera equipment. These housings can be of different characteristics and influence the camera parameters in various ways. Therefore, some preliminary considerations have to be made regarding the used camera setup. These considerations, some preparation steps, as well as the final alignment and reconstruction process will be outlined in the following subchapters.

5.1.1 Intrinsic Camera Parameters

The majority of camera lenses suffer from image distortions with the effect that the resulting rectangular image does not represent a rectangular area in the scene. 3D reconstruction of a scene with bundle adjustment is done by intersecting the light rays going from one individual point to several different camera poses. Therefore, the intrinsic camera parameters and the resulting image distortions play a crucial role in photogrammetry as they affect the direction of the rays. To calibrate cameras, a number of standard techniques are used, involving a known set of control points or checkerboards with known dimensions. Various software packages offer straightforward calibration workflows, such as *Agisoft Lens* or the *Camera Calibration Toolbox for MATLAB*.

Underwater applications, however, suffer from another optical component that adds extra uncertainty to the intrinsic parameters. When the light travels from the object towards the camera, it passes through additional interfaces before reaching the camera lens. First the interface between water and the transparent port of the underwater housing (usually made from glass), and secondly the interface between the port and the air within the housing. At these interfaces of media with different densities, the waves get refracted according to Snell's law (Nocerino et al., 2016).

Hemispherical dome ports, as the ones of the OFOBS cameras, consist of two surfaces. The outer surface at the water-glass interface and the inner surface at the glass-air interface. Ideally (and usually), these surfaces have different radii, but the same center of curvature. If the camera is positioned in the underwater housing as such that the entrance point of the lens (the center of perspective, also known as nodal point of the camera) is perfectly aligned with the center of curvature of the dome port, the rays would enter the housing along the surface normals of the port without any further refraction (Nocerino et al., 2016). This would fulfill the pinhole model as all rays are bundled in one point. In this case the housing would not additionally alter the path of the light and an in-air camera calibration model would as well be valid underwater (Menna et al., 2016).

Unfortunately, only slight offsets in alignment between camera and port induce significant nonlinear distortions. In this case, the rays would not be bundled in one point as refraction happens away from the perspective center of the lens, making the pinhole model invalid. Kunz & Singh (2008) illustrate that misalignment effect in further detail. These distortions can be approximated by traditional camera calibration. However, the resulting model would only be valid for a certain distance to the camera housing at which the calibration was conducted. Additionally, it would only be valid for the specific environmental characteristics at the time and place of the calibration. Changes in water density (due to pressure, salinity, or temperature variations) will change the refraction angles according to Snell's law, not to mention deformations of the underwater housing due to pressure (Nocerino et al., 2016). Łuczyński et al. (2017) present the *Pinax-model* which uses an in-air calibration model in combination with environmental parameters describing the refraction index of water in order to calculate the resulting overall distortion pattern. However, this model is only applicable for flat port underwater housings. Even though a flat port is basically a dome port with infinite radius and a largely misplaced camera position,

the refraction happening on a hemispherical dome port with respect to a misaligned camera lens can hardly be modeled a priori (Menna et al., 2016).

It becomes clear that image distortion in underwater camera systems is neither a very stable effect, nor can it be modeled to the same extend as for in-air applications. As mentioned above, the OFOBS cameras were never intended to be used for photogrammetric purposes and were therefore never properly calibrated. Regarding the alignment of the cameras within their housings, it is hard to quantify the offsets between nodal point and the center of curvature of the dome port. But since the cameras are frequently maintained, which requires opening the housing, it is fair to assume that the alignment changes from time to time.

Unfortunately, the absence of a camera calibration model has severe effects on the quality of the reconstruction results, especially with a lack of accurate position and orientation data (Sedlazeck et al., 2009; Kwasnitschka et al., 2013). Fortunately, for the OFOBS dataset, this information is available through the built in INS. Bundle adjustment algorithms can work with different kinds of input. If some information is missing, the algorithm might be able to resolve it up to some extent. Within the processing of the here presented data, the intrinsic camera parameters for both OFOBS cameras could be estimated sufficiently, which will be presented and discussed in chapter 7.1.1.

5.1.2 Input Preparation

As mentioned above, the video stream cannot directly be used for the photogrammetric reconstruction and therefore needs further preparation. Additionally, the different meta information for the bundle adjustment process needs to be collected and primed for the software. The aim of this step is to derive individual image files from the video material, to add sufficient timing information to each image, and to extract position and orientation for both video frames and still images from the INS log. Figure 5-2 outlines these processes.
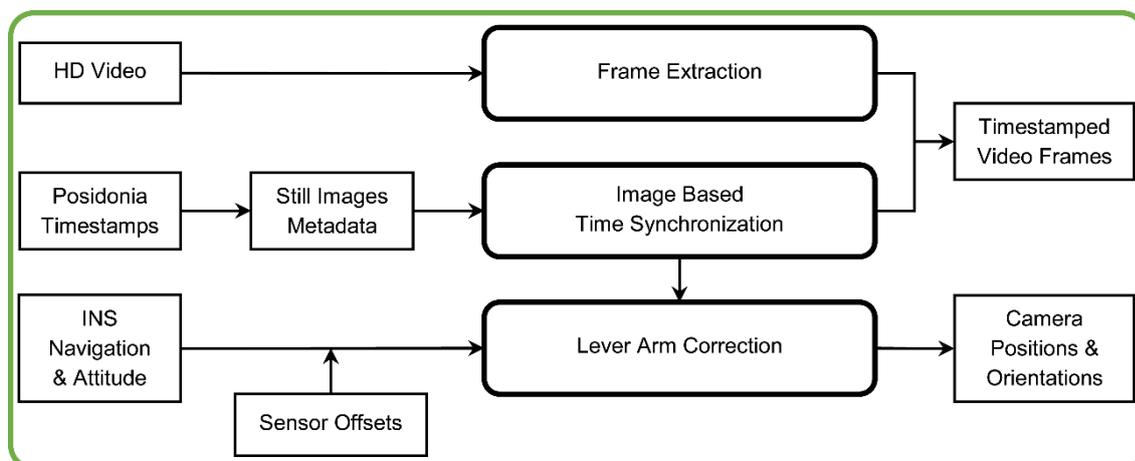
Figure 5-2: Workflow for preparation of the optical datasets
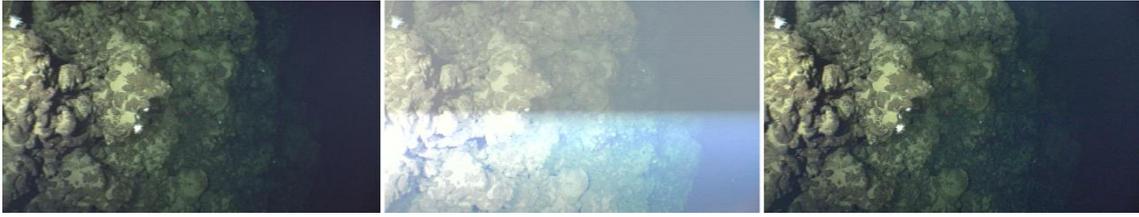
Figure 5-3: Three consecutive frames showing how the flash is visible in the video

The frame extraction was done with *FFmpeg*, a command line based collection of programs for processing of video and audio material. The video filter requires an input video file, a start time, the duration, and the desired extraction frame rate and can extract the video frames in several different output image formats. The frame rate is mainly dependent on the survey speed and the altitude over ground and needs to be adjusted so that individual points on the seafloor are covered by multiple frames to assure sufficient alignment and correct reconstruction. If the terrain is very complex or the image quality comparatively bad, it is advised to extract frames with a higher rate. However, it has to be mentioned that an increase in the overall number of images drastically increases the processing effort.

In order to timestamp the extracted frames, they were searched for visible flashes from the still image strobe lights. Figure 5-3 illustrates that the short light burst of a flash is visible in only one frame in the video stream. This flash corresponds to a still image that is timestamped by the Posidonia data stream. Every extracted video frame has a running number that, in combination with the extraction framerate, corresponds to a relative time offset to all other frames. A Python script was written that takes the frame number of the reference frame, the timestamp of the corresponding still image and the extraction framerate in order to calculate the UTC timestamp for all frames. The result can be verified with other frames showing a flash. After time synchronization, the frames containing a flash signal can be deleted as they are not usable for the reconstruction process.

As mentioned above, the result of the bundle adjustment process will improve with the amount and quality of the initial input data provided to the software. The position and attitude measurements of the OFOBS INS were recorded with 20 Hz. These measurements are with respect to the local position of the INS on the OFOBS subsea frame. In order to calculate the position and orientation of the two cameras, a self-written Python toolbox was utilized. The seven parameter transformation combines INS position, attitude, angular bias, and distance offset between the sensors (see Appendix A) to convert the measurements from the INS frame to the camera frames. The result is a list of geographic positions (latitude, longitude, depth) and orientation values (roll, pitch, yaw) for each video frame and still image that can directly be supplied to the next processing step.

5.1.3   Alignment & Reconstruction

The photogrammetric processing, aside from the auxiliary steps mentioned in the previous section, was entirely accomplished with *Agisoft PhotoScan Professional* (version 1.2). PhotoScan is

a SfM software that was originally created for aerial photogrammetry applications, but is now widely used in geodesy and for consumer level 3D modeling from photographs. Additionally, the software has proven very useful for various underwater applications (e.g. Zhukovsky et al., 2013; Balletti et al., 2015; Van Damme, 2015; Kwasnitschka et al., 2016). In its Professional Edition, PhotoScan offers a complete integrated toolset and a step-by-step workflow for photogrammetric reconstruction, georeferencing, and 3D modelling. The process is straightforward and structured in three simple steps to achieve a 3D model from input images. However, if desired, PhotoScan offers detailed fine tuning mechanisms for each step as well as additional tools for image preparation, point cloud cleaning, and manual improvements of the reconstruction result. Verhoeven (2011) gives a detailed explanation of the individual processing steps for aerial photographs. Additional info to each step is give in the well-structured PhotoScan User Manual (Agisoft (Ed.), 2016). Kwasnitschka et al. (2013) describe another project that uses PhotoScan for a 3D reconstruction survey in the deep sea with an unmanned camera vehicle. The general reconstruction workflow used during this thesis is outlined in the schematic in Figure 5-4.

At the beginning, a PhotoScan project was prepared for each of the three sample areas. The following overall process is mostly identical for all three areas, only with minor differences in some settings. Additionally, the processing of area C required another step, which will be described in chapter 5.3. The following figures, illustrating the different intermediate results, show the dataset of area B.

After creating the project, the video frames and still images are imported in the software and combined with the list of camera positions and orientations from the INS. Figure 5-5 visualizes
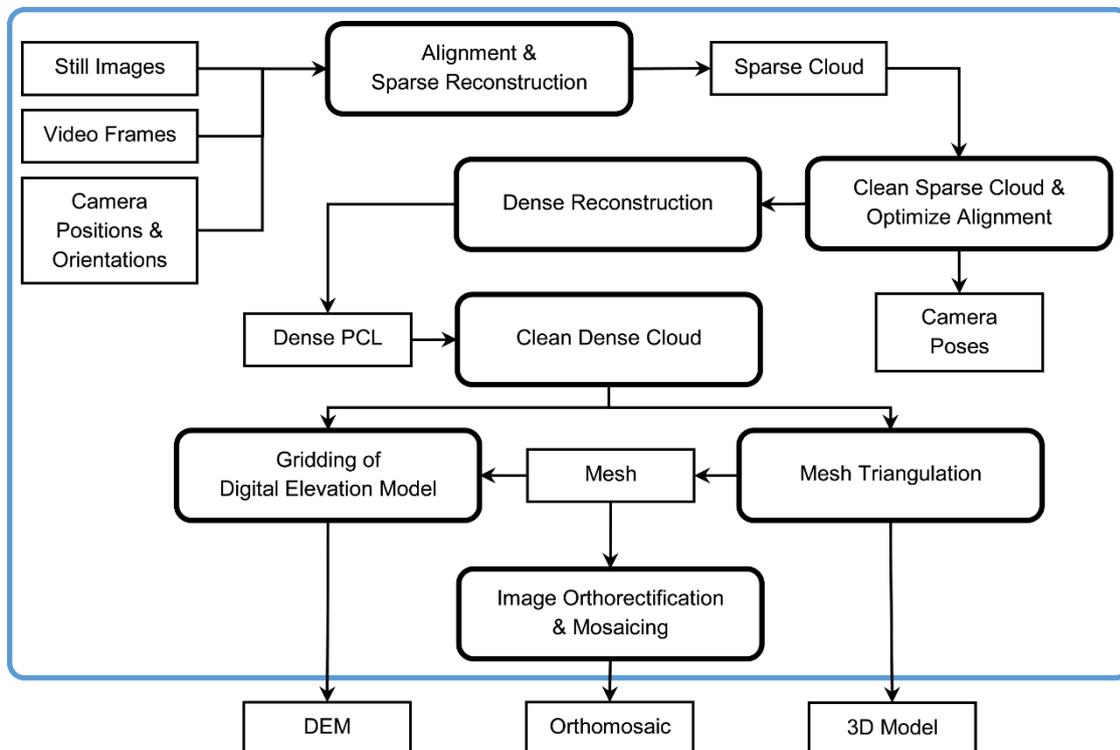
Figure 5-4: Alignment, reconstruction and processing workflow for the optical datasets
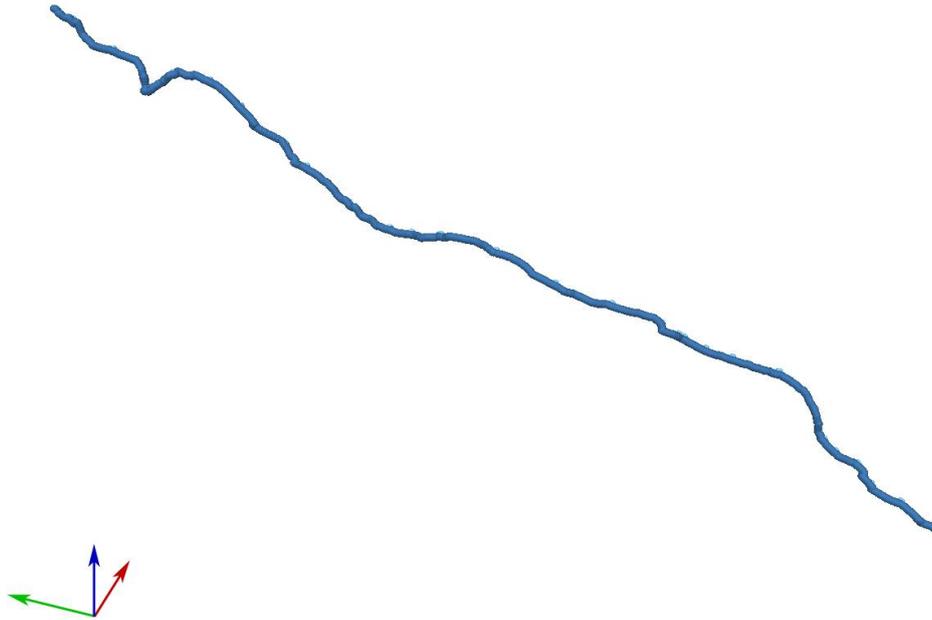
Figure 5-5: 3D view of raw input camera positions, area B

this step. The camera pose input should be extended with information on the accuracy of the input to improve the bundle adjustment. Theoretically, the position accuracy relative to the ship should be three times better than 0.2% of the slant range (we remember chapters 2.1.2 and 3.3). In area B, for example, it would be approximately 2 m. However, due to the circumstances described above, the realistic accuracy will be much lower than that. Different alignment tests were performed and the most successful for the overall reconstruction quality and error distribution was the rounded raw USBL accuracy. Unfortunately, only one accuracy value can be given for all three dimensions, even though in the deeper survey areas, the vertical position is more accurate and independent of the USBL quality due to the pressure sensor (3 dBar accuracy). For the angular accuracy of the camera orientation, it is similar. The INS gives standard deviation values for yaw, pitch and roll, which for area B would be around 1°, 0.004° and 0.004° accordingly. Since PhotoScan takes only one value for all three rotations as well as to account for installation misalignments, the accuracy of 2° was set for the input.

These preparations are followed by the alignment process, the first step of the reconstruction. The SfM algorithm performs a feature detection on all imported images in order to find matching points in multiple images. These tie points will be monitored throughout the image sequence. To ease the process, an initial pair preselection was performed, which groups images based on a rough image matching with low accuracy settings. The preselection can also be done based on the initial camera poses. This, however, did not give useful results for unknown reasons.

Part of the alignment process is the camera pose estimation including position and orientation, as well as the estimation of the intrinsic camera parameters (focal length, location of the nodal point, radial and tangential distortion coefficients). If any initial information is parsed to the algorithm, depending on the user settings (accuracy, fix calibration, etc.), this data will be used for the computation and adjusted throughout the process. During the sparse reconstruction, the detected multiview tie points are projected along their rays from the individual camera poses
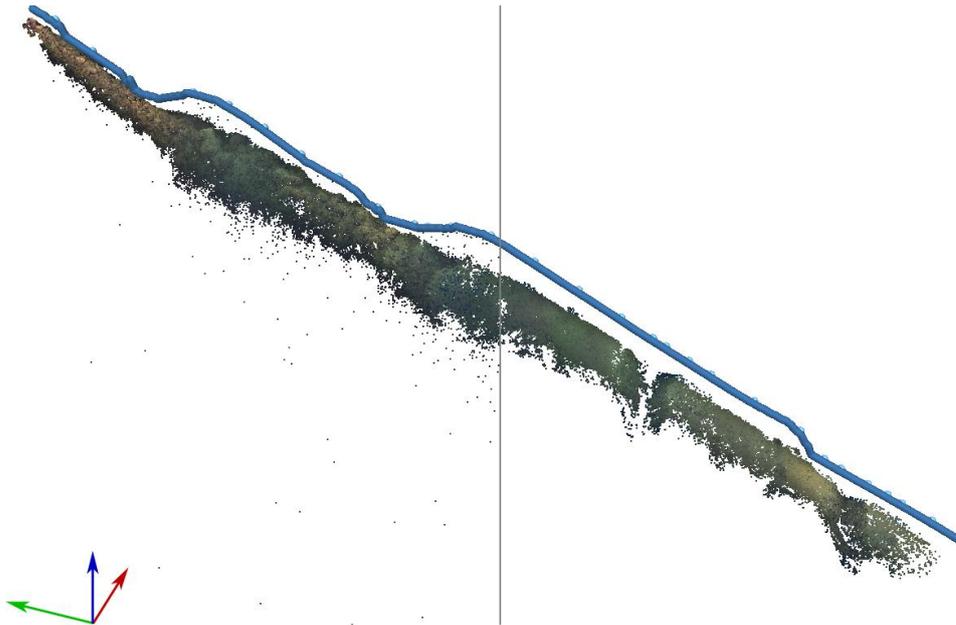
Figure 5-6: Reconstructed sparse cloud, area B. (left) Uncleaned, (right) filtered and manually cleaned. The improved camera positions estimated by bundle adjustment form a much smoother track than the raw input positions visible in Figure 5-5. Sudden vertical changes (blue axis) correspond to winch speed changes.

and written to a 3D sparse cloud. Each tie point contains statistical information about its reconstruction uncertainty and projection accuracy. This information can be used to automatically apply quality filters to the sparse cloud to reject outliers. After cleaning the sparse cloud, an optimization process improves the reconstruction points including all the above-mentioned parameters according to the revised tie points. Figure 5-6 shows the sparse cloud in its uncleaned and cleaned state as well as the improved camera positions.

The next step is the dense stereo reconstruction of the scene. The algorithm operates on a pixel level to compute depth maps for each of the aligned images and to generate a colored dense point cloud. The dense cloud has significantly more points than the sparse cloud (about 65 times for area B) and usually represents the scene in great detail. Depending on the image quality, the dense cloud also contains a number of outliers that have to be cleaned manually. The dense cloud of area B (both uncleaned and cleaned) can be seen in Figure 5-7.

The last step is to generate a triangulated mesh (Figure 5-8) from the dense cloud, which is more coherent as a digital representation of the scene. It can also be used for orthorectification of the images or to create smoother digital elevation models (DEM). PhotoScan offers two different methods for triangulation, *Arbitrary* or *Height Field* as well as parameters for the number of computed triangles, interpolation, and hole filling. For generating DEMs, the height field mesh would theoretically be preferred, since the process is much less time consuming. However, the resulting mesh contains inadequate levels of detail, even on the highest possible setting. Therefore, the arbitrary triangulation was performed on all sample areas. Despite the longer processing times, the result is of higher detail and contains overhangs, which might be significant for visualizing complex seafloor formations.
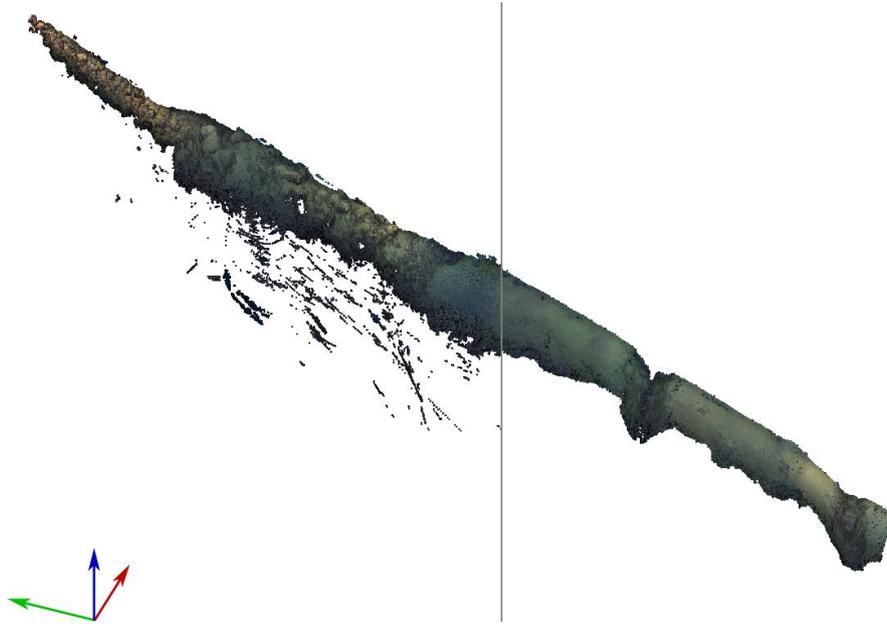
Figure 5-7: Reconstructed dense cloud, area B. (left) Uncleaned, (right) manually cleaned.

Figure 5-8: Triangulated mesh, area B, shaded and vertex colored according to the dense cloud.

5.2 Side Scan & Bathymetry

Processing the EdgeTech Sonar data was done with *Caris HIPS and SIPS* (version 10.2), an industry standard processing software for bathymetry, acoustic seafloor imagery, and water column data. HIPS and SIPS contains all necessary tools to import, adjust, correct, and clean the data and to create the final output grids for both bathymetry and side scan data. Figure 5-9 shows the used processing workflow for the acoustic dataset.

Raw EdgeTech JSF files contain all navigation and attitude data from the INS measurements. However, HIPS and SIPS does not successfully correct the vehicle depth, hence, all pings refer to mean sea level. An advantage to this is that a first grid can be computed in order to get an altitude over ground dataset to extract the flight height for each point on the track. However, to get reasonable bathymetry values the vehicle depth needs to be added to the survey lines. This can be achieved by parsing the INS log with the integrated *Generic Data Parser*.

An issue with line scanning devices, like swath bathymetry sonars, is their dependence on accurate knowledge of the sensor pose. Individual measurements (e.g. pings) cannot be aligned at other measurements and the result is therefore highly sensitive to errors in the navigation. Earlier figures have shown the quality of the navigation data and it becomes obvious that the quality of the acoustic data results is affected by that (Figure 5-10). As shown in chapter 5.1.3, the bundle adjustment conveniently improves the camera poses to a best fit for the photogrammetric
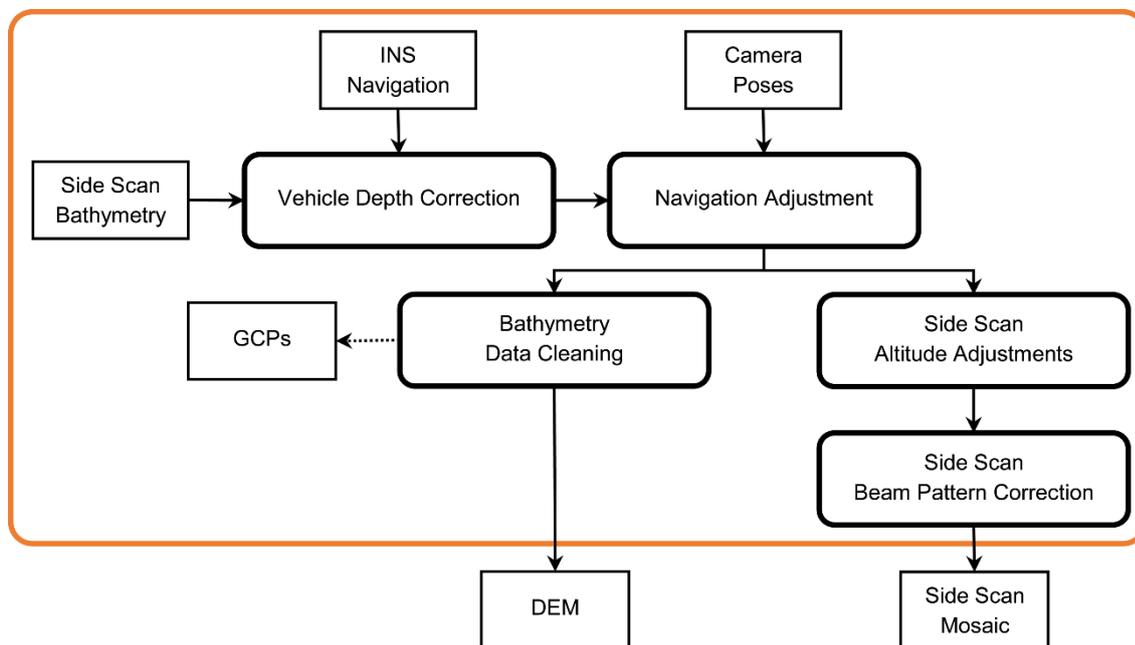
Figure 5-9: Processing workflow for the side scan and bathymetry dataset

reconstruction. Since the images were timestamped, the camera poses correspond to a point in time and can, with regards to the motion data, be transformed back to the INS position and parsed on the sonar survey lines. The low frequency (equals the video extraction framerate) of the resulting navigation data is not ideal since the sonar ping rate is higher and the positions for pings in between camera poses need to be interpolated. However, the OFOBS moves very steadily with little high-frequency position changes, so applying the adjusted camera navigation still improves the sonar data significantly.

The ranges of the binned bathymetry solution from EdgeTech Discover are corrected on the fly with the values from the attached SV probe. Despite the fact that it is almost impossible to get a reasonable set of close bottom SV profiles for the OFOBS survey areas, the small flight height limits the amount of significant vertical layering in the water column between the transducer and the seabed and the SV is not expected to change much on that distance. Additional SV correction was not contemplated for that reason.

Another correction, usually performed on bathymetric measurements, is the tide correction, in order to reference the depth information to a specified vertical datum. Without any tidal reference stations in the vicinity of the survey area, these corrections rely on the use of tide predic-
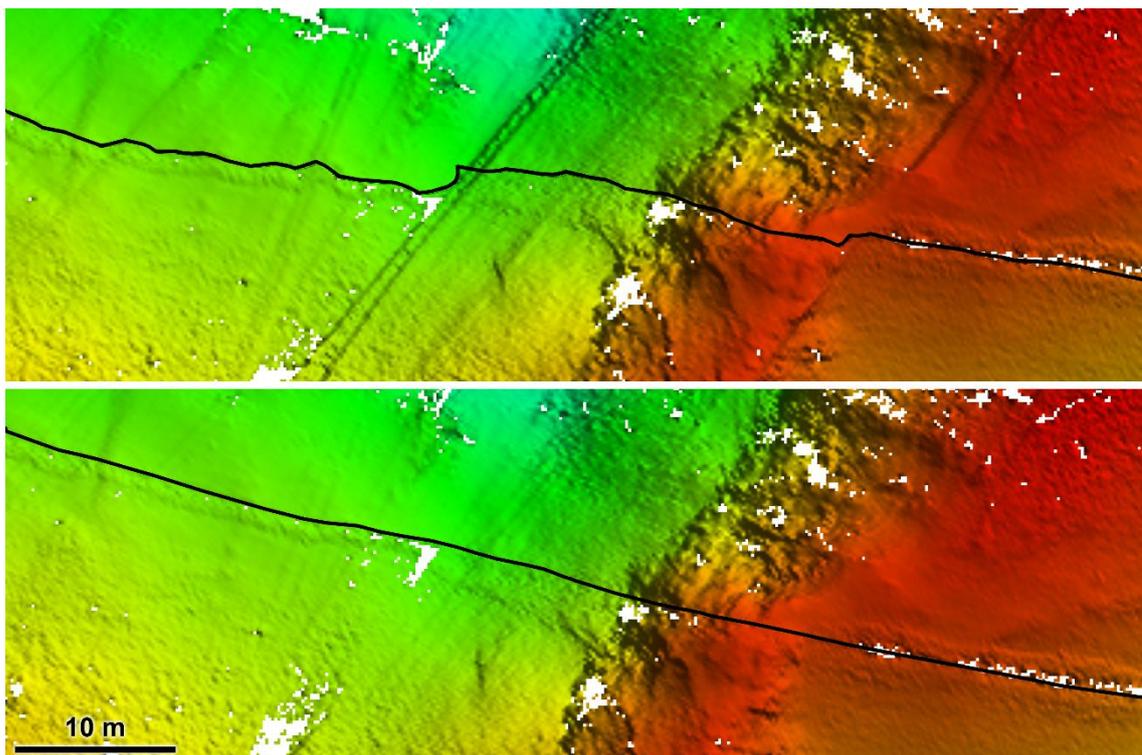
Figure 5-10: Bathymetry subset of area C and the corresponding track line. (Upper) shows bathymetry with raw navigation. Bigger artifacts in the grid clearly correspond to jumps in the navigation. (Lower) shows bathymetry with adjusted navigation from camera poses. Smaller jumps are still visible in the grid, but the overall quality has improved significantly.

tion models like the Arctic Ocean Tidal Inverse Model (AOTIM-5). In the Arctic Ocean, the predicted tidal amplitude maximum of 1.8 m lies in the southern Barents Sea. The predicted amplitude in the PS101 survey area is below 30 cm (Padman & Erofeeva, 2004). Since the pressure sensor accuracy is a multitude of that value, an additional tide correction is not useful. The pressure sensor was zeroed at sea level in the research area, hence processed depth measurements refer to mean sea level within approximately 3 m.

The bathymetry data was then cleaned with the HIPS and SIPS editors, namely *Swath* and *Subset Editor*. Even though the MPES data is comparatively clean after binning, some areas contain severe errors in bottom detection. This usually happens in steep terrain, where the grazing angle between the sonar beam and the seabed is too low and the return signal is very weak, or when the seabed rises above 100° from nadir, which is the maximum filter gate of the sonar (Figure 4-8, Figure 5-11). Additionally, the data contains a small nadir gap and survey points in the nadir area show artifacts, which might be due to the relatively low flight height during PS101. These areas were manually cleaned as well.

For the side scan data, the *SIPS Engine* in HIPS and SIPS was utilized to correct and mosaic the datasets, with identical processing steps taken for both HF and LF. Two main steps are necessary to improve the resulting side scan mosaics. Both are visualized in Figure 5-12.

The side scan waterfall is a plot of reflection amplitude over time of successive pings. The time between the signal transmission and the first bottom contact will give very little reflection from the water column and produce a gap in the bottom data. To properly georeference features in the data, this gap needs to be digitized and removed during mosaicking. Especially in areas with rapid altitude changes, this slant range correction significantly improves the result by undistorting the mosaic.

Due to transmission properties and changes in the grazing angle over time the signal reflection deviates, even on homogeneous seabed (Chang et al., 2010). To account for those deviations, a transducer specific beam pattern correction can be done in HIPS and SIPS. The beam pattern correction equalizes the reflectivity pattern over the whole swath resulting and in an even dataset allowing for better object identification or seabed classification.

To enhance the image quality, the data was additionally despeckled and gain-normalized. The speckle correction checks for inconsistencies in reflection between individual pixels and their neighbors and smooths over outliers by interpolating their values. The gain-normalization removes noise by averaging the reflection intensity over a number of subsequent pings and adjusts the gain for each ping for a more homogeneous result.
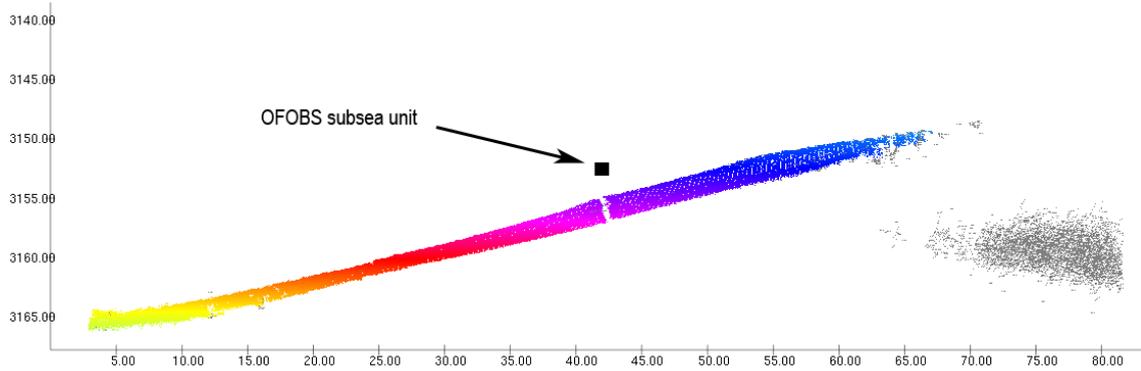
Figure 5-11: 2D rear view on a bathymetry point cloud subset in area C. Rainbow colored points are the accepted survey points, grey points are rejected outliers. The rectangle marks the approximate position of the OFOBS subsea unit with an altitude of 2.3 m above seafloor. The rejected soundings are a product of false bottom detection, assumingly because the actual seabed on the more distant starboard slope rises above the 100° (from nadir) filter gate. Below the transducer, the nadir gap is visible.
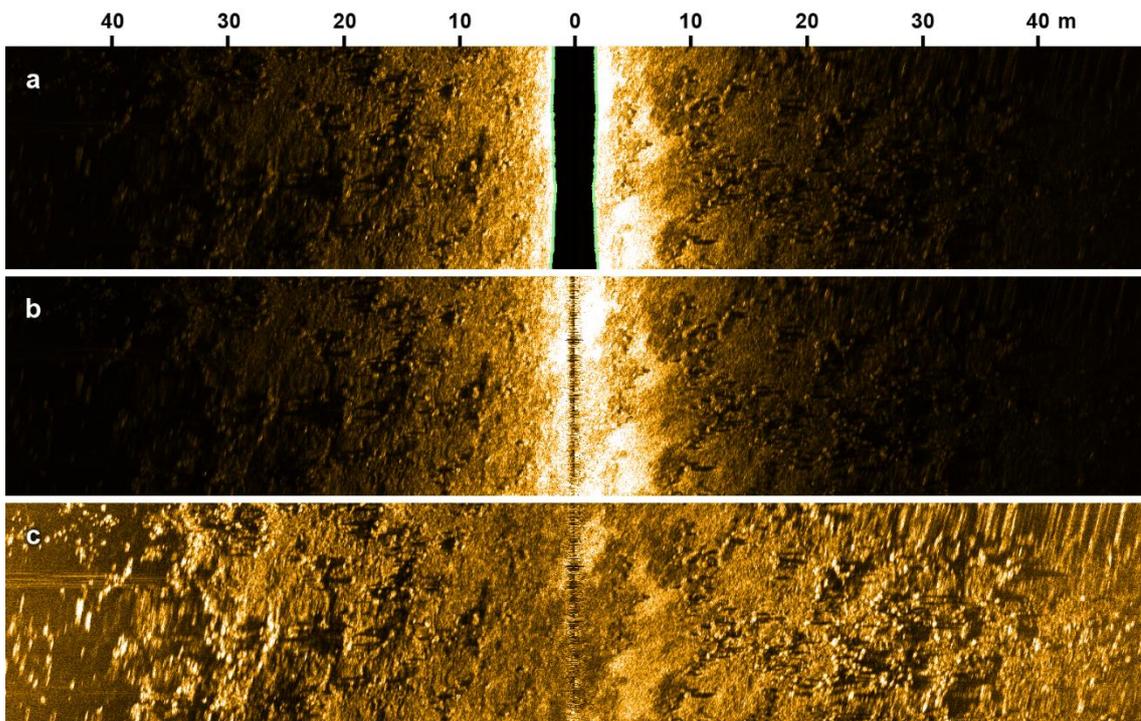
Figure 5-12: Side scan processing steps with HF waterfall data of area A. (a) Raw data with water column gap. The green line represents the first bottom contact. The gap width is twice the altitude over ground. (b) Slant range corrected data. Uneven brightness pattern indicate deviations in reflectivity due to grazing angle, range, and transmission properties. (c) Beam pattern corrected data with additional speckle correction and normalized gain, showing an even reflectivity pattern over the whole swath.

5.3 Combined Data Alignment

To confirm the successful alignment between the optical and acoustic datasets, difference surfaces between the photogrammetrically derived bathymetry and the MPES bathymetry were computed. For area A and B, these difference surfaces showed adequate alignment results. For area C, while visible feature align nicely horizontally, vertical offsets could be observed. The reason seems to lie in the fact that PhotoScan does not take separate accuracy values for horizontal and vertical positions and might have to do with a section in area C that suffers from poor image quality due to higher altitudes.

To correct the depth offset, artificial content based GCPs were placed in the reconstructed scene within PhotoScan, equally distributed over the whole area. The horizontal position for the GCPs was taken from the original photogrammetry grid. The depth, however, was taken from the MPES bathymetry. After adding the GCPs, the camera alignment was optimized once more, followed by the explained processing steps (dense reconstruction, dense cloud cleaning, and mesh triangulation). The result of this combined alignment approach is discussed in chapter 7.1.4.

6 Results

From the processing steps described in the previous chapter, a number of different data products were computed for each of the three sample areas. The following section will present examples for all types of results and give detailed information on the data characteristics. An overview on the three areas and the data results is give in the maps in Appendix C.

6.1 Acoustic Bathymetry

Surface grids were computed in HIPS and SIPS from the cleaned MPES bathymetry and exported as georeferenced raster DEMs. The maximum width of data around the navigation track is 40 m to both sides. The cell size for the grids was set to 20 cm to have at least two of the equidistant data points from each ping in one cell. With the points of subsequent pings, the resulting mean point density per cell for the three grids came out at 8, 14, and 12 for area A, B, and C accordingly. The variations in density correspond to different survey speeds for the different areas. The density is relatively high and higher grid resolutions could potentially be achieved. However, with the low flight heights, smaller objects can already cast an acoustic shadow in the MPES data, resulting in a hole in the grid. With a cell size of 20 cm a good balance was achieved between density and closed coverage. Nonetheless, prior to export, the holes in the surfaces were interpolated by their nearest neighbors with a 5x5 cell matrix for a more consistent representation. Figure 6-1 shows an example of the acoustic bathymetry grid in area A.
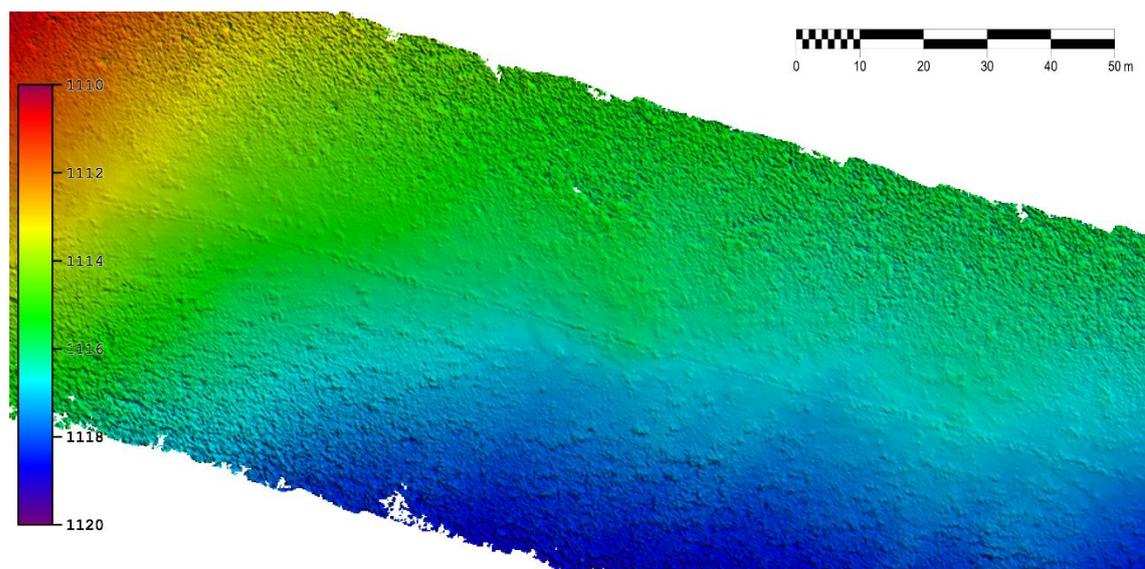
Figure 6-1: Bathymetry grid from MPES data (example from area A)

6.2 Side Scan Mosaics

From the corrected side scan data, mosaics were generated in HIPS and SIPS and exported as georeferenced backscatter imagery. HF data produced grids with 50 m, LF data grids with 100 m around the track line to both sides. With a cell size of 3 cm for both HF and LF, the grids have a mean density of 1.2 samples per cell. This ensures a very high resolution in the mosaics while minimizing the holes in the grid. Figure 6-2 illustrates the mosaics for the HF and the LF side scan data.
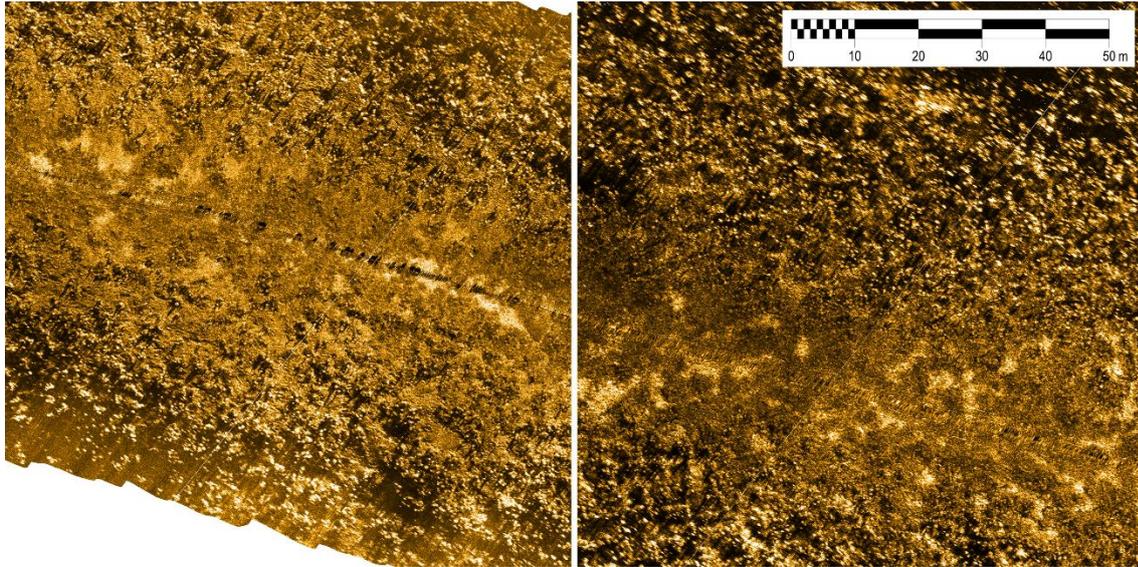
Figure 6-2: Side scan mosaic from MPES data (area A, same extend as Figure 6-1). (left) HF, (right) LF.

6.3 Photogrammetry derived Microbathymetry

For the optical data, microbathymetric grids were computed in PhotoScan from both the dense cloud and the triangulated mesh and were exported as georeferenced raster DEMs. The width of these grids varies with flight height and the resulting image coverage. The resolution for the dense cloud DEMs cannot be changed in PhotoScan but is automatically set according to the density of the cloud. For the mesh DEMs, this value can be adjusted and was rounded up to the next full millimeter. Table 6-1 lists the resulting cell sizes for the different grid results. Different resolutions for the different areas are a product of flight height, reconstruction uncertainty and image quality. Figure 6-3 shows an example subset of the photogrammetry derived micro-bathymetry grid in area B for both the mesh and the dense cloud DEM.

Sample area	Grid cell size	
	Dense cloud DEM	Mesh DEM
A	2.26 mm	3 mm
B	5.66 mm	6 mm
C	4.2 mm	5 mm

Table 6-1: Grid cell sizes for photogrammetric microbathymetry
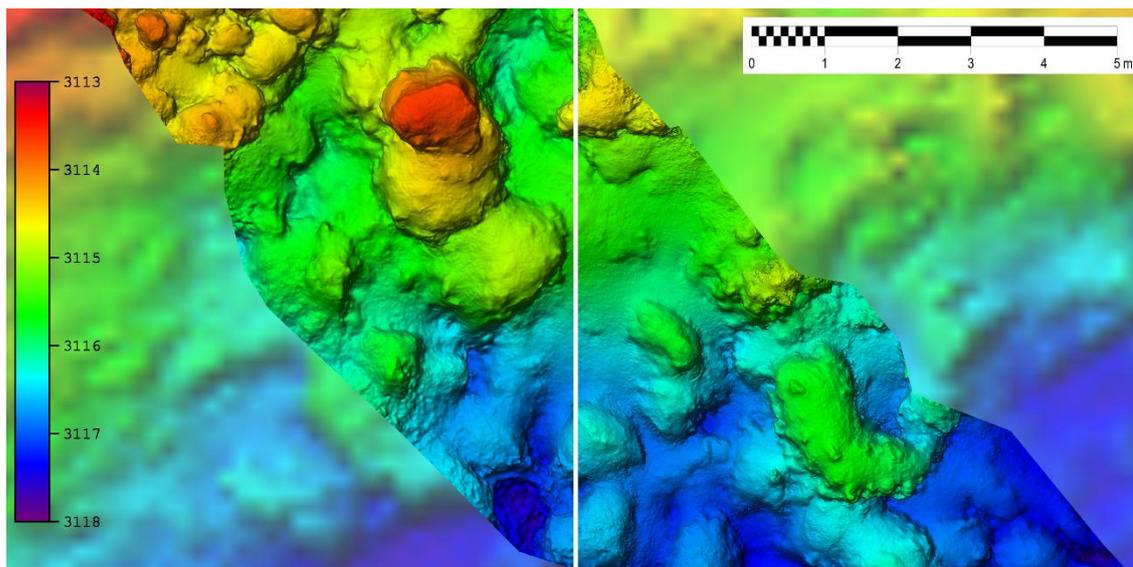
Figure 6-3: Photogrammetry derived microbathymetry grid (example from area B). (left) DEM from triangulated mesh, (right) DEM from dense cloud, overlaying the acoustic swath bathymetry. The difference between the two is in the detail. While the triangulation smooths over noisy regions, this noise is still visible in the dense cloud DEM in a close-up view.

6.4 Image Orthomosaics

The face count of the triangulated meshes was decimated to create smooth surfaces for orthorectification of the individual images. The rectified images were then mosaicked, grouped by the camera, resulting in a higher resolution mosaic for still images and a lower resolution mosaic for video frames. The pixel size for area B and C came out at 1 mm for the image mosaic and 2 mm for the video mosaic. For area A, due to the lower flight height, resolutions of 0.5 mm (images) and 1 mm (video frames) could be generated. The resulting GeoTIFFs had to be tiled to avoid conflicts with the 4 GB file size limitations on some file systems. Examples for the image mosaics can be seen in Figure 6-4 for the still images and Figure 6-5 for the video frames.
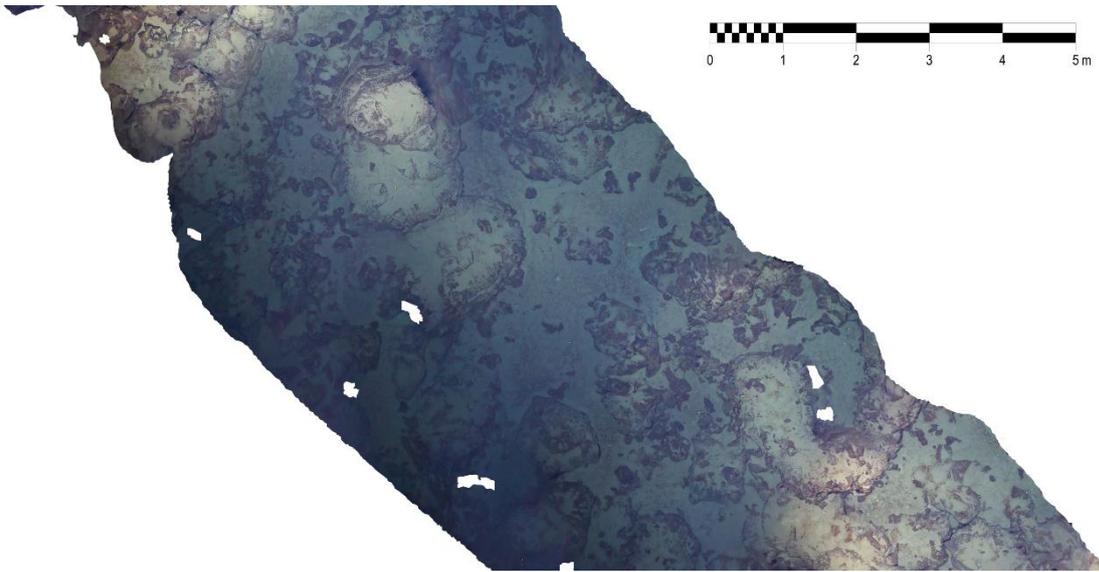
Figure 6-4: Orthorectified image mosaic from still images (area B, same extend as Figure 6-3). Mosaic is of very high resolution and quality but contains gaps when shadowed areas are not covered by a still image. Color absorption varies with slant range, resulting in an uneven coloration in the mosaic.
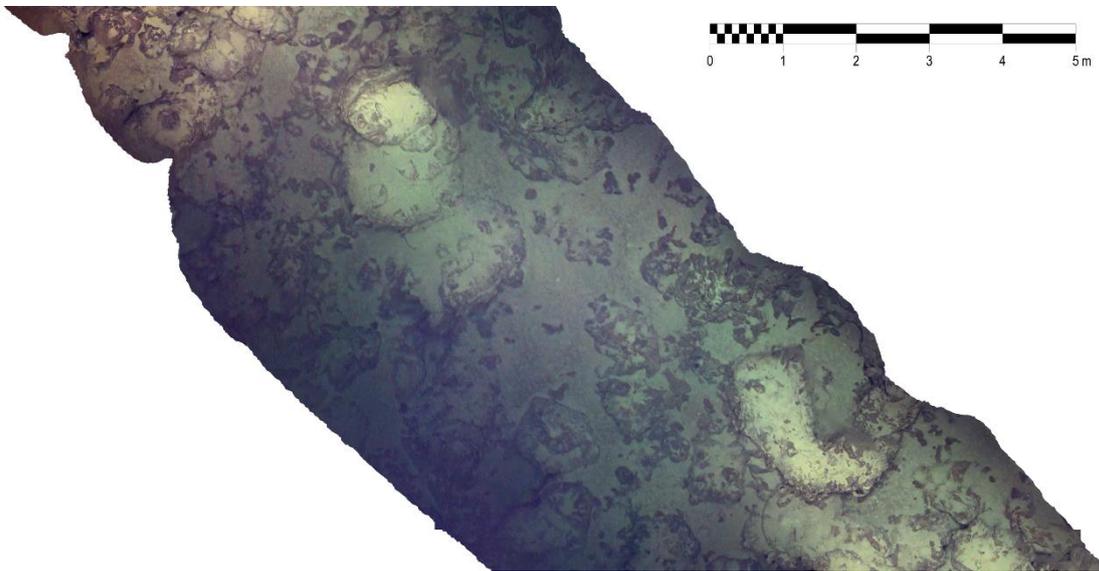
Figure 6-5: Orthorectified image mosaic from video frames (area B, same extend as Figure 6-3). Mosaic is of lower resolution and quality but has an even gap-free coverage due to the higher temporal resolution of the video frames. Color absorption varies with slant range, resulting in an uneven coloration in the mosaic.

6.5 3D Models

The triangulated mesh was used as an intermediate product for DEM generation and image or-thorectification. Yet, it is also a final product on its own. In PhotoScan, generated 3D models are, by default, colored according to the point colors of the dense cloud. Additionally, textures can be computed from the images and draped over the mesh for a greater realistic representation. Meshes can be generated for the whole area or any subset of the dense cloud if needed. The models can then be exported to various 3D file formats from PhotoScan and used in additional software for further processing or scientific analysis (Kwasnitschka et al., 2013). The mesh of area B in its full extent could be seen in Figure 5-8. Additional examples for the generated 3D models can be seen in Figure 6-6 and Figure 6-7.

One thing worth mentioning is the amount of data generated during mesh triangulation. For example, the complete model from area B in full detail consists of more than 38 million triangles. While this mesh can conveniently be used for DEM computation, it is rather resource demanding to simply view it, not to mention, virtually navigating through it. The detail of the mesh should always be adjusted to the individual needs prior to export. Fortunately, PhotoScan offers a mesh decimation functionality to adjust the amount of faces within the software.
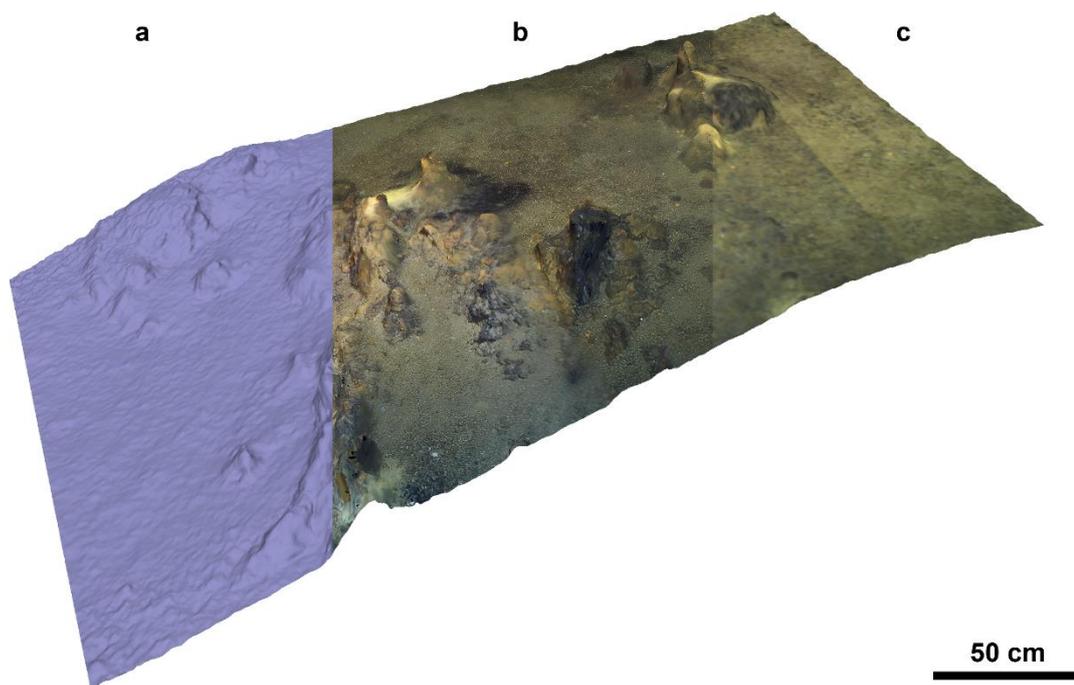
Figure 6-6: 3D model of a patch of hydrothermal chimneys (subset of area C). (a) Uniform colored, (b) texturized, and (c) colored by dense cloud. The image texture was created from both still images and video frames to ensure full coverage of the model. The scale bar is referenced to the center of the model.

Figure 6-7: Close-up view of a sponge 3D model (subset of area A). Represented as (left) a textured model and (right) edges of the triangulated mesh. The crustacean on the sponge (~7 cm in length), even though being present in the geometry of the mesh, cannot be recognized as such from the 3D model alone. The textures significantly increases interpretability. The scale bar is valid for the image depth of the crustacean.

7 Discussion

The following section will discuss the results presented in chapter 6. As a multisensor network, the OFOBS dataset accumulates a couple of uncertainties, some of which come from sensor inaccuracies and some from issues with the raw data. The first subchapter will discuss those uncertainties and evaluate the ability of the processing workflow to overcome some of them. This is followed by a general evaluation of the OFOBS survey method with respect to alternative technology for deep-sea, high-resolution habitat mapping. Chapter 7.3 will then give recommendations for future improvements, regarding setup changes of the system as is, as well as potential hardware extensions. Finally, the last subchapter will give a brief list of ideas on potential use cases for the presented data in further research, as well as an outlook on future work related to the OFOBS project.

7.1 Consideration of Uncertainties

In land-based photogrammetry, there is often the possibility to verify surveying accuracies with the help of GCPs. These GCPs can be either already present in the area or additionally added with reliable geodetic methods. In the case of deep-sea applications, setting up GCPs would be theoretically and technically possible, but it would not be useful from an economic standpoint, especially in polar regions, where the harsh conditions require more ship time and specialized equipment. Therefore, to estimate the global survey uncertainties, one has to rely on the theoretical achievable accuracies of the individual systems while considering the survey environment.

Estimating survey uncertainties for the OFOBS dives during PS101 however, is a rather impossible task as there are a large number of factors to be considered, some of which cannot be quantified (e.g. subsea position deterioration due to sea ice). The following section will briefly list those uncertainties from the sky down to the seafloor. Additional detailed discussions on some of the major points in the overall topic of uncertainties will follow in the subchapters.

For bathymetric measurements, individual soundings, or data points, need to be positioned in a global frame in order to get georeferenced data results. To achieve this, a multisensor network needs to be combined to transform the measurements from the sensor frame to the vessel frame and from the vessel frame to the global frame. For USBL positioned subsea vehicles like the OFOBS, additional transformations are needed, since the vehicle is only positioned relative to the ship. Throughout these transformations, all the measurement uncertainties of the individual utilized sensors add up, resulting in a TPU for the survey data.

From the sky to the seafloor, this process starts with a GNSS, used for positioning the ship. *RV Polarstern* uses a Trimble MS750 dual frequency GPS receiver combined with an iXBlue HYDRINS

INS. This setup could work with additional differential position corrections, both in real time or post processing. However, in the open Arctic Ocean there are no sufficient nearby reference stations usable for correction input and the available Satellite Based Augmentation Systems (SBAS) do not cover these high latitudes (Gao et al., 2011). Hence, the global horizontal position accuracy lies around 10–15 m. The HYDRINS has very similar performance values as the OFOBS' onboard PHINS. This adds another uncertainty in angle measurements to the following subsea positioning.

Titcomb et al. (2012) state that while most USBL systems claim a position accuracy of 0.2% of the slant range, they rarely achieve this in real world applications. The special environmental circumstances in Arctic sea ice conditions and close seabed applications, as outlined in chapter 3.3, most certainly reduce the USBL accuracy significantly. As shown in chapter 4.1, the INS on the OFOBS improves the raw USBL measurements by smoothing over severe outliers. The global position however does not improve much during this process.

All those combined measurement uncertainties result in relatively low position accuracy for the OFOBS subsea unit, especially with regards to the high resolution of the acquired data, resulting in noticeable errors in the bathymetric measurements. Fortunately, these errors can be divided in global position errors and local errors in the results. While the global position errors have to be accepted as is, the multisensor data of the OFOBS and the described workflow offer additional possibilities to reduce the local errors and improve the relative results (see chapter 5.2 and 7.1.3).

7.1.1 Camera Calibration

Chapter 5.1.1 outlines the importance of the knowledge of the intrinsic camera parameters for a successful and accurate photogrammetric reconstruction. During the bundle adjustment process, PhotoScan estimates these parameters to a best fit from all the input datasets, both for the video and the stills camera. The resulting distortion vector plots can be found in Appendix B.

In PhotoScan, the individual images can be grouped into calibration groups. These groups are then assumed to have the same intrinsic parameters and exactly one camera calibration is estimated per group. Logically, it makes sense to group the images according to the used camera, in this case one group for the still images and one for the video frames, as it was done within the workflow of this thesis. This, however, does not take care of the distance depended distortions that may arise from poorly positioned cameras within their dome port, as described in chapter 5.1.1.

One way to verify the reconstruction results is to measure the distances between the laser dots in the orthorectified still image mosaic. The dots should ideally have a constant distance to each other as the three lasers are positioned around the stills camera with equal spacing, parallel to the looking direction of the camera. Table 7-1 shows the statistical results of those measurements. Foremost it has to be mentioned that most of the reference measurements are close to

	Mean	Min	Max	StD	No. of samples
Area A	50.0	48.9	51.7	0.9	13
Area B	52.0	49.5	54.1	0.9	14
Area C	51.0	48.9	52.1	1.1	16

Table 7-1: Statistics of laser dot distances (in cm). For each sample, the distances were measured between all of the three laser dots. The samples were evenly distributed over the different still image orthomosaics.

or within the calibration uncertainty of the laser distances (50 cm, +/- 1 cm). However, it becomes clear that the distances in area B and C have higher variations, possibly because of the significant changes in flight height throughout the acquisition. This indicates distance depended variations in the intrinsic parameters as well as slightly misplaced laser installation angles.

One option would have been to reuse the estimated camera calibration from the first sample area as an additional input for the two following datasets. However, not to assume one of the three sample areas to be better suited than the others, the calibration was estimated from scratch for all of them. This additionally accounts for possible changes in camera placement between the two dives. As an additional verification of the reconstruction quality it can be said that the three calibration results, each for both the stills and the video camera, showed very similar results with only slight variations. These variations are most likely caused by the different characteristics of the sample areas in topography and imagery, as described in chapters 3.4 and 4.2.

To test the capabilities of the software, the dataset of area A was used to do a reconstruction without initial input of navigation or attitude information. The sparse cloud and the camera distortion plots can be seen in Figure 7-1. In comparison to the calibration model created during reconstruction with navigation and attitude input, this illustrates the need for auxiliary input for the bundle adjustment algorithms. Further on, it illustrates how important the correct camera calibration model is for the quality of the reconstruction. The displacement of the focal point causes a systematic decrease in estimated flight height and scaling towards the end of the dataset. Similar results could be observed when only few images where equipped with navigation data to be used for the reconstruction, which underlines the effectiveness of the approach, described in chapter 5.1.
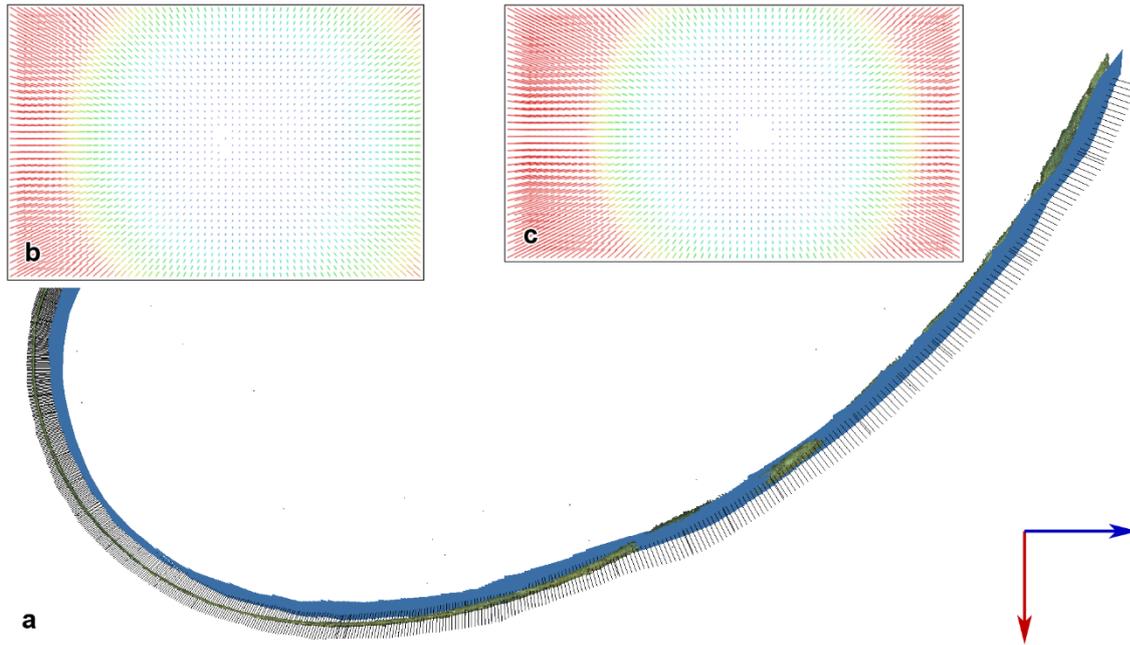
Figure 7-1: Dataset of area A reconstructed without initial input of navigation. (a) The reconstructed sparse point cloud after the alignment process shows severe systematic errors, as the dataset should be along a linear track above flat terrain with very little variations in topography. The resulting camera distortion plots for (b) the stills camera and (c) the video camera show a noticeable displacement of the focal point from center.

7.1.2 Attitude Estimation

Part of the reconstruction process is the camera pose estimation, which includes not only the position, but also the attitude of the camera. These attitude estimates were exported from PhotoScan to be compared to the measurements of the INS. Figure 7-3, Figure 7-4, and Figure 7-5 show the attitude plots for yaw, pitch, and roll for the dataset of area B, as it is most representative for the discussion. Since the INS measurements are of very high accuracy, this comparison can be used for additional quality verification of the reconstruction. However, this brings up the need for further discussion on the topic.
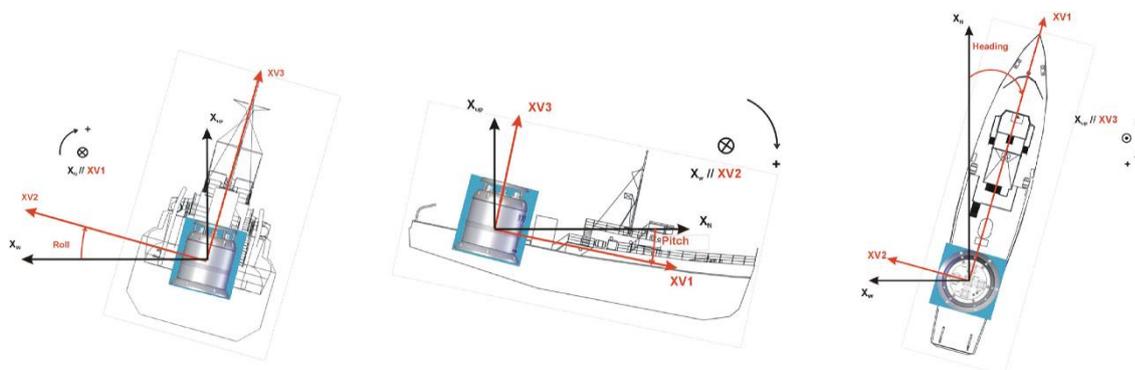
Figure 7-2: PHINS attitude convention for roll, pitch and yaw. (IXSEA (Ed.), 2010a)

One important thing worth mentioning is the convention on motion. Yaw, pitch, and roll are angular rotations around the three axes. The PHINS convention (Figure 7-2) considers yaw the rotation around the vertical axis, positive towards starboard, pitch the rotation around the across-track axis, positive nose down, and roll the rotation around the along-track axis, positive towards starboard. For PhotoScan, no definition could be found in the literature, but from analysis of the attitude data, the convention was determined identical, except for pitch being positive nose up. The cameras of the OFOBS are mounted approximately 90° with respect to the travel direction, which means, the INS roll becomes negative pitch and the INS pitch becomes negative roll in PhotoScan. Since the installation angles of the OFOBS cameras have never been properly investigated, it is possible that they are not exactly mounted at 90°. This would have the effect that a portion of the frame's pitch rotation would be measured as roll, and vice versa.
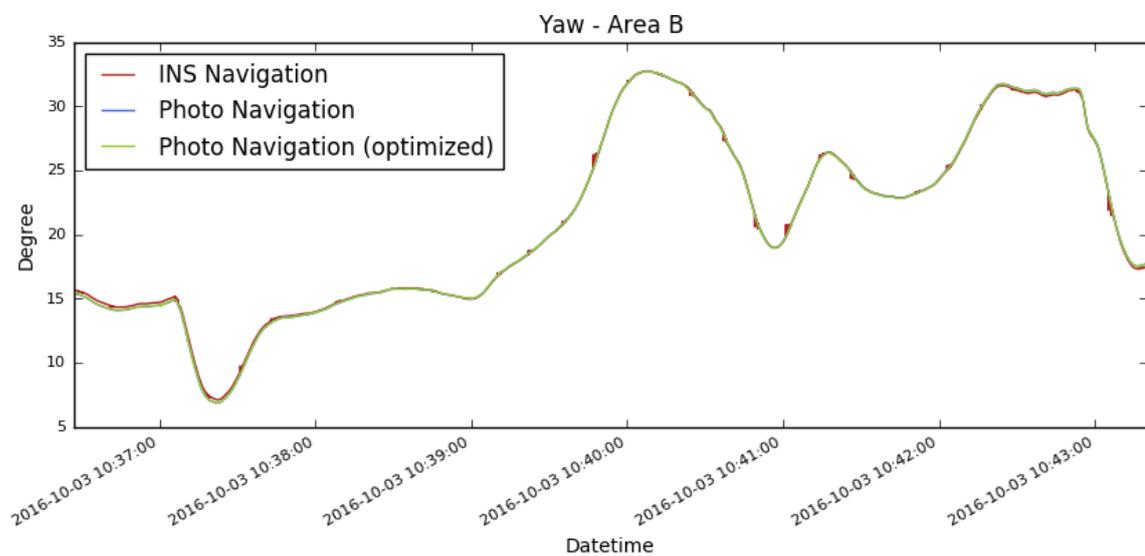
Figure 7-3: Yaw plot, area B
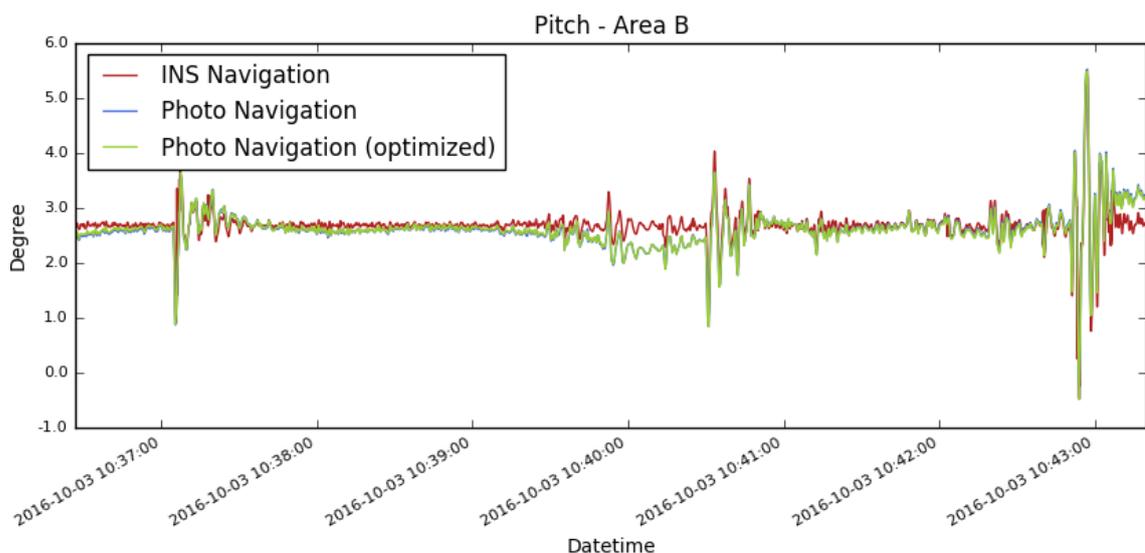
Figure 7-4: Pitch plot, area B

67
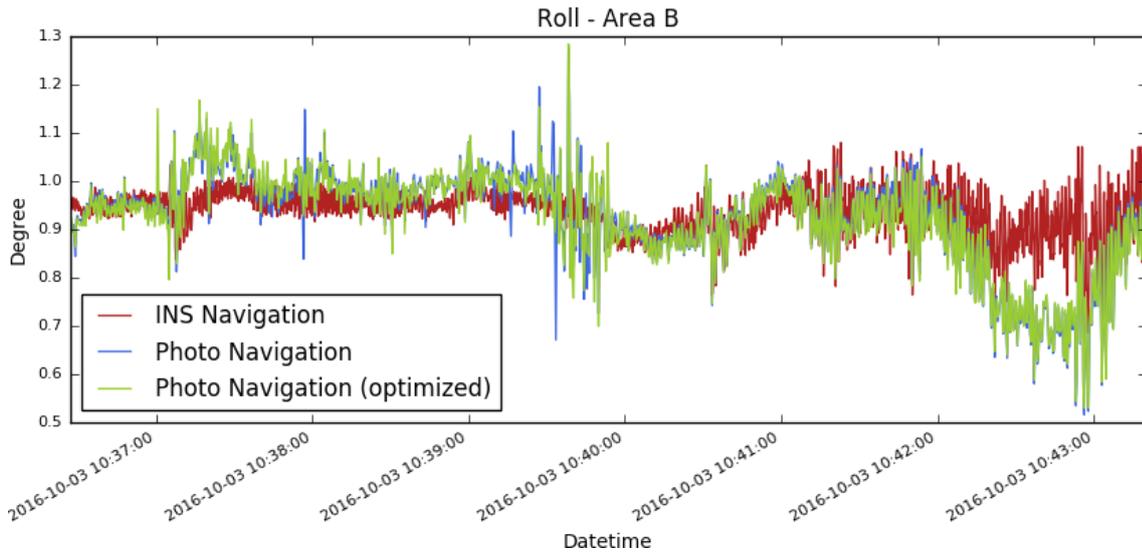
Figure 7-5: Roll plot, area B

Looking at the yaw (Figure 7-3) and pitch (Figure 7-4) plots, slight deviations of the estimated motion from the INS measured values can be observed from time to time. These deviations are possibly a product of some sort of internal stress of the bundle adjustment process to find the best fit for all considered parameters. Since the accuracy was set to 2° for the attitude input within PhotoScan, local reconstruction uncertainties can easily be loaded onto the attitude estimation error. This is particularly visible in the roll data plot (Figure 7-5), as this rotation shows the smallest overall amplitudes due to the high roll stability of the OFOBS subsea frame.

Figure 7-6 shows the attitude errors, meaning the offsets between estimated attitude and INS measurements, for all three rotations in area B. While there are still sections with larger error values, the overall estimation can be considered as very successful. The sections that show larger errors can be clearly correlated with the pitch and roll data. When comparing those plots to the navigation track line in Figure 7-9, it becomes clear that these sections are linked to changes in the vertical acceleration of the subsea unit.

Worth mentioning at this point is that especially the pitch plot (Figure 7-4) nicely illustrates the hydrodynamic behavior of the OFOBS subsea unit. The frame was originally balanced to be level in air. Yet, in water, the frame tilts towards ~2.5° (nose down). When being heaved gradually, the angle changes to a somewhat stable value of ~2.8°. Whenever the vertical acceleration changes very sudden (winch stopped, change of speed or direction), the frame starts to rock around the across-track axis with values around +/-3°, sometimes higher.

These sudden rotational accelerations are a source of error for the attitude estimation. This however is not necessarily due to reconstruction errors. The data of the INS, hence the navigation and attitude input to PhotoScan, is time based. Therefore, another uncertainty comes from the time synchronization of the frames and images. The time stamps of the still images, to which the video frames are referenced (we remember chapter 5.1.2), are referenced to the Posidonia data stream. This data stream is received by the OFOS software package with 1 Hz resulting in an accuracy of one second for the time stamps. The high frequency changes in the error curve
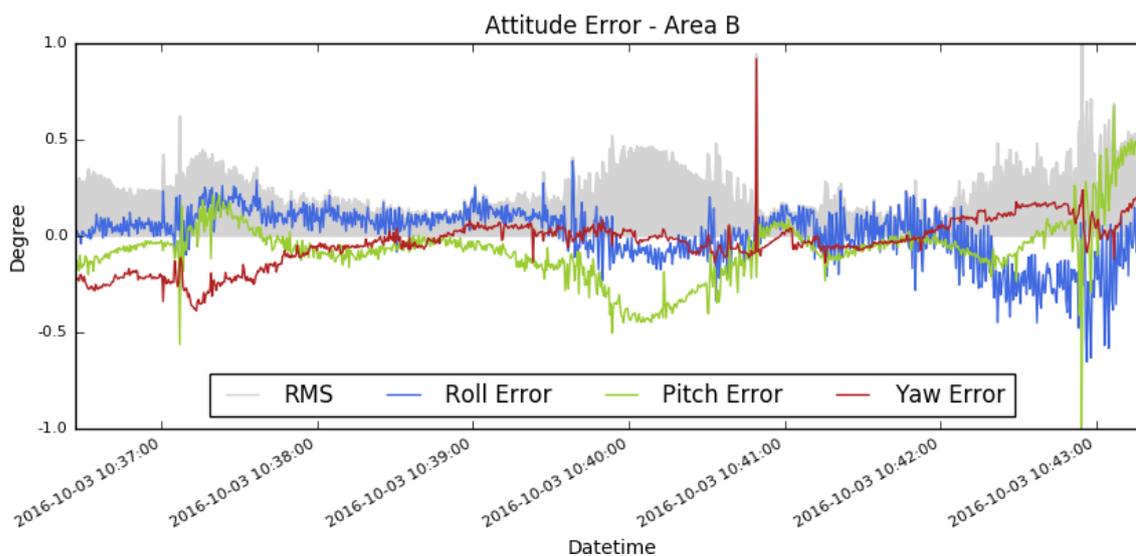
Figure 7-6: Attitude error plot, area B

are most likely a product of a slight time offset, as they occur primarily in area with high amplitude motion, as well as in the roll data, a curve of a generally high frequency character in the case of the OFOBS.

7.1.3 Navigation Improvements

It was explained in chapter 5.2 that the exported camera poses were used for navigation adjustment on the sonar data to improve the bathymetry and side scan results. It needs to be noted again that these adjustments cannot be verified with any GCPs along the track and quality evaluation of the results can only be done on a subjective level. To do so, the individual raw images and the video material can be used as a reference in order to get an impression of shapes and sizes of seafloor objects as well as an idea on the general motion characteristics of the OFOBS subsea frame.

Additional verification can be done with the bathymetry and side scan grids themselves. Deviations of the navigation data from the actual track line produce noticeable distortions in the side scan mosaics as illustrated in Figure 7-7. Ideally, these distortions are resolved to some level after the navigation adjustment. Another indicator are vertical jumps in the bathymetry. Since depth steps, as they are visible in Figure 5-10, are rarely found on the natural seafloor, they can be identified as artifacts, especially when they occur parallel to the line of soundings of one individual ping. These steps in the OFOBS bathymetry can usually be linked to horizontal (not vertical) jumps in the navigation data and their intensity increases with the slope inclination angle of the seafloor beneath.

Figure 7-8 shows the position error in the three dimensions in area B. Here, *error* means the offset between the input navigation and the estimated camera poses. The term was adapted from PhotoScan, where the input navigation is considered true and the deviations of the estimates are considered as errors. In the case of the OFOBS data, it is fair to say that the logic turns around and the errors can more likely be considered as offsets of the INS navigation from the actual track, or otherwise said, can be considered as navigation improvements with respect to the subjective measures mentioned above.

One thing that becomes clear in the graph is the higher vertical position accuracy of the INS data, as it was already explained in chapter 5.1.3. While the horizontal proportions in area B deviate from the estimated track up to 4 m, the vertical offset stays below 50 cm. This could also be observed in the position errors in area A. Area C on the other hand shows larger vertical offsets, which will be discussed in the following chapter.

The navigation track, both from the INS and the camera pose estimates is again visualized in Figure 7-9 for a more intuitive representation. As mentioned above, the attitude data can clearly be correlated to the acceleration pattern throughout the track.
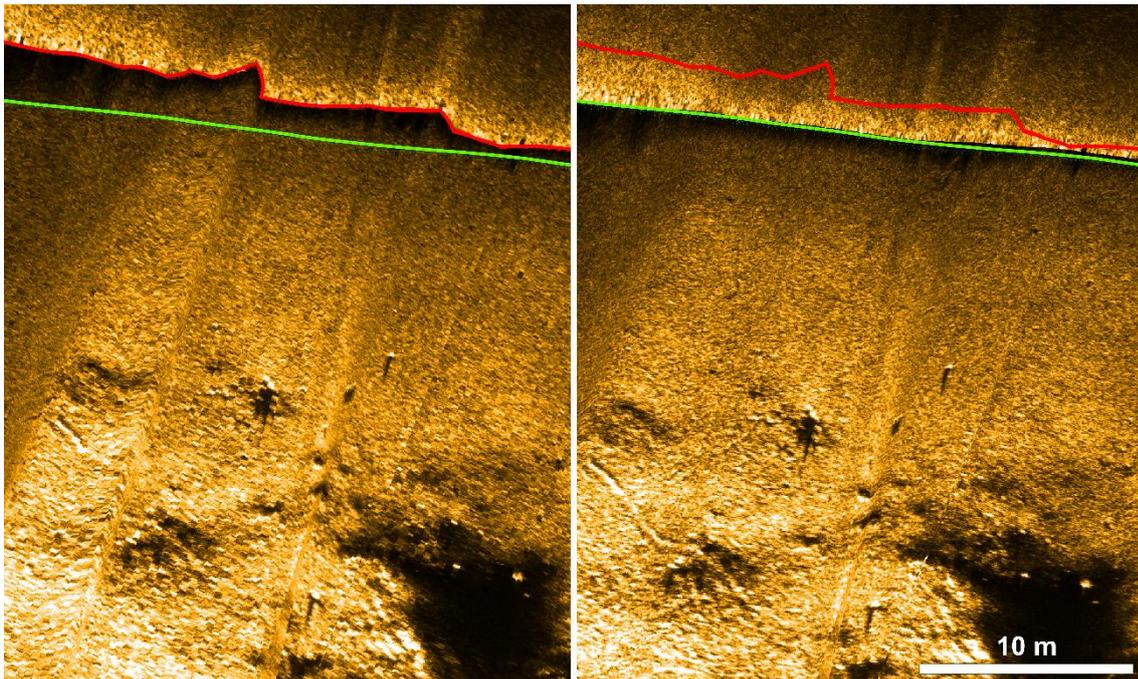
Figure 7-7: HF side scan mosaic, (left) before and (right) after navigation adjustment. The mosaic, especially the feature in the lower left, shows significant distortions that correspond to the offset between the original navigation track (red) and the adjusted track (green).
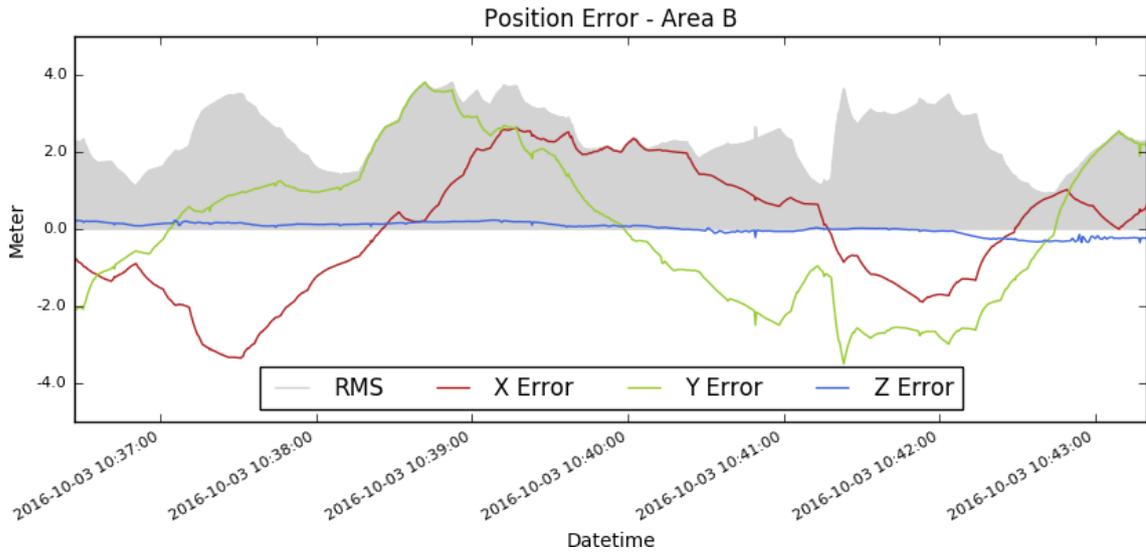
Figure 7-8: Position error plot, area B. Colors correspond to axis colors in Figure 7-9.
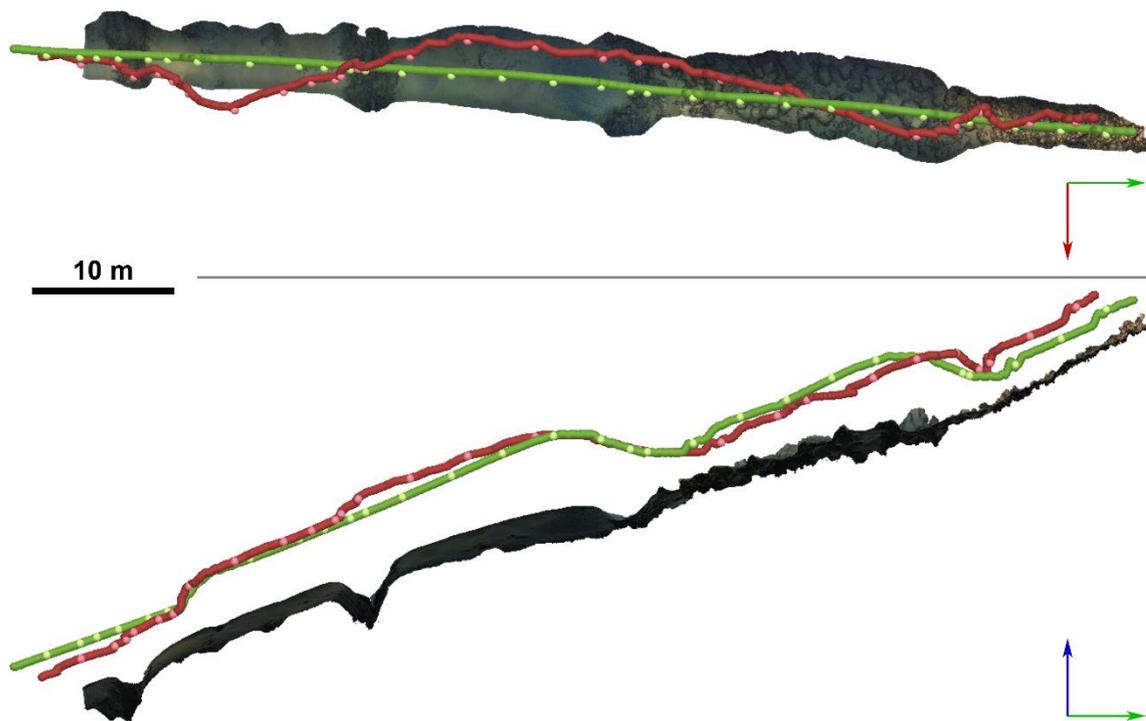
Figure 7-9: Navigation Adjustment in area B. (upper) Top view, (lower) side view on the model. Red spheres mark camera positions imported from the INS log, green spheres mark bundle adjusted camera positions after alignment and optimization. Lighter colored spheres represent still images, darker colored spheres video frames.

7.1.4 Misalignment in area C

Chapter 5.3 already introduced an issue with the photogrammetric reconstruction in area C that needs to be discussed in further detail. While the other two datasets gave sufficient results after the processing steps described in chapter 5.1, the photogrammetry derived bathymetry in area C showed significant vertical offsets to the sonar bathymetry. The difference surfaces are shown in Figure 7-10, before and after the combined data alignment.

Looking at the position errors before the combined alignment (Figure 7-11), it becomes clear that the vertical offsets are a product of faulty camera pose estimates instead of actual image depth calculations. This is supported by the consistency of the camera calibration models throughout the three datasets (Appendix B). While the vertical position offset in area A and B is relatively low, as discussed in the previous chapter, the values in area C are suspiciously large (around 1 m and higher).

Clearly, there are a couple of factors adding up to the total error budget, many of which were discussed in the previous sections. Area C however, shows the weakness of the SfM approach in underwater applications when lighting conditions are less than ideal. During the transect, the OFOBS passed two steep slopes, coming from uphill. Because of the latency of the winch and the resulting inability to keep a constant altitude, the distance to the seafloor increased rapidly up to 10 m before being decreased again by winch operation. Due to the poor lighting at this high altitude, the seabed at the foot of the slope showed little contrast in texture for the feature detection to work with (Figure 7-12).

This is well represented in the pixel error of the reconstruction for the individual video frames. The pixel error is a statistical value within PhotoScan that gives the RMS reprojection error, meaning the pixel offset between the position a point can be projected onto the original photo and the position of the 3D point in the multiview sparse cloud, calculated over all detected feature points in the individual photos (Agisoft (Ed.), 2016). Looking at the frames with a pixel error greater than 1.0 (145 out of 850), a significant majority (140) of those frames lies above the two slopes in area C.
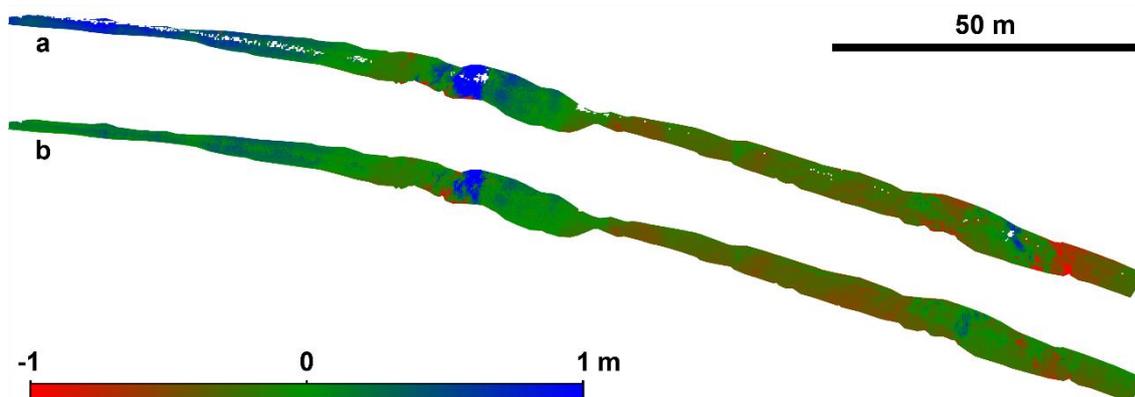
Figure 7-10: Differences surfaces of area C, mesh DEM minus sonar bathymetry. (a) is the difference surface prior to the combined data alignment, (b) is the final difference surface.
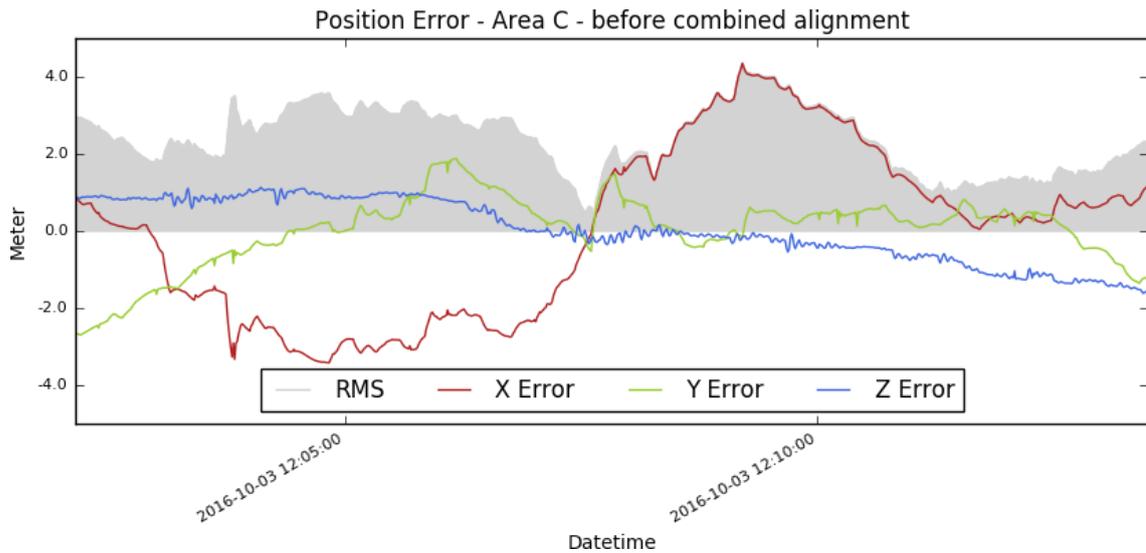
Figure 7-11: Position error plot, area C, before combined alignment

After vertical adjustment, the dense cloud was recomputed. The different dense reconstruction results are shown in Figure 7-13. Adding the artificial GCPs means, correcting the photogrammetry dataset according to the sonar bathymetry, which was originally navigation-corrected according to the camera pose estimates, hence the name *combined data alignment*. This process is not ideal, as it adds additional uncertainties to the final results. Nonetheless, the improvement can be verified with the reconstruction results of the dense cloud. Before adding the GCPs and
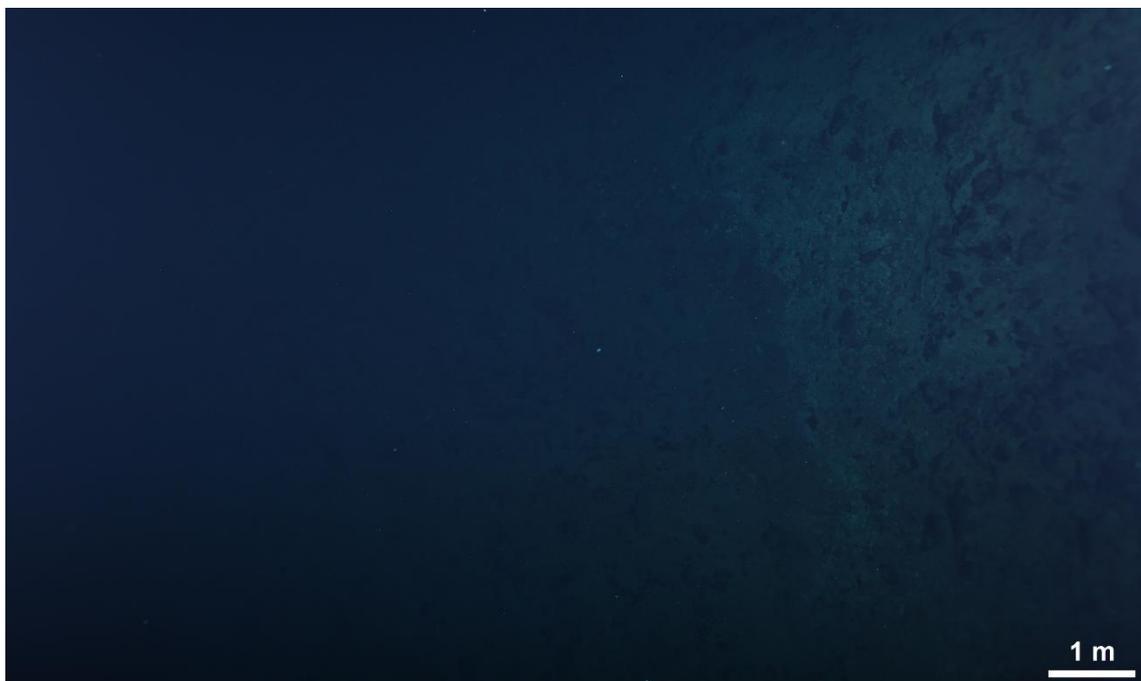
Figure 7-12: Lighting conditions behind a steep slope, area C. (Purser et al., 2017)

reoptimizing the alignment, the area of highest flight height, just above the foot of the slope, could not be reconstructed properly, resulting in whole in the dense cloud and significant model distortions. After the combined alignment, the dense cloud was created without gaps over the whole dataset. Figure 7-14 shows the final position errors for area C. The vertical offset was reduced to values below 70 cm and even the Latitude (Y) offset decreased significantly.
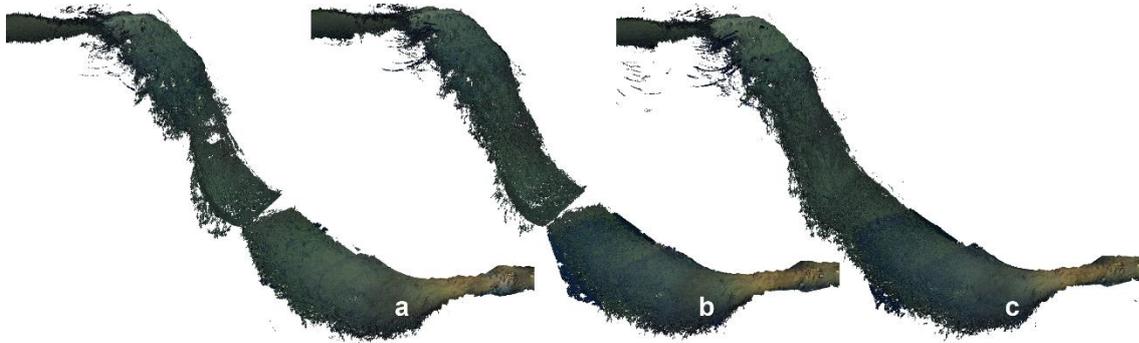
Figure 7-13: Dense cloud of one of the two steep slopes in area C. (a) shows the dense cloud after the initial alignment, (b) after the first optimization, and (c) after the additional combined alignment.
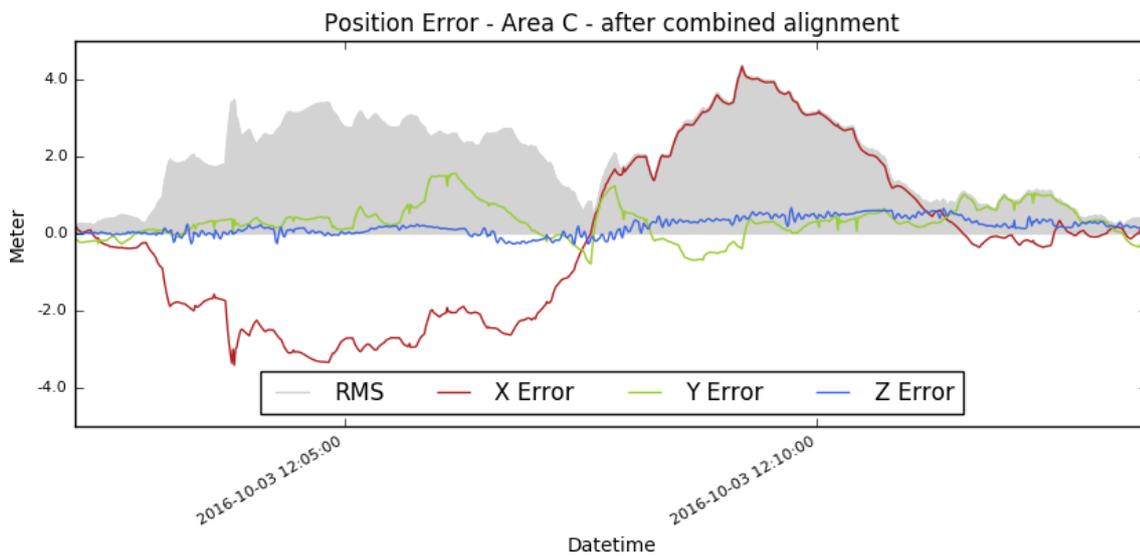
Figure 7-14: Position error plot, area C, after combined alignment

7.2 Evaluation of the Survey Method

While the concept of deep-towed acoustic systems (e.g. Dorschel et al., 2009), deep-towed camera systems (e.g. Barker et al., 1999; Solan et al., 2003; Bergmann et al., 2011), and even the simultaneous optical and acoustical surveying approach (e.g. Pfingsthorn et al., 2016; Caress & Barr, 2017) has been around for some time, the here presented way of data acquisition is a novel approach for high resolution multisensor microbathymetric habitat mapping in deep sea environments. The OFOBS stands out for its individual combination of sensors and its versatility regarding the range of environments it can be operated in. The following section will evaluate the OFOBS as a surveying tool and discuss its capabilities in comparison with similar deep sea survey systems.

To begin with, let's briefly summarize the key points, characterizing the OFOBS surveying technique. The OFOBS is a 6000 m rated deep-towed sensor frame that is usually operated at a survey speed around 0.5–1 knots, winched down from the towing vessel to an altitude of 1.5–10 m above the seabed. Its two onboard cameras capture a constant video stream at 25 Hz and high resolution still images every 20 seconds, plus additional manually triggered still captures. At an altitude of 2 m, the average bottom pixel resolution of the still images is approximately 0.5 mm. To augment the optical systems, the frame was equipped with a bathymetric side scan sonar, a forward looking imaging sonar, and some auxiliary navigational sensors. The ranges/coverages of the downward facing and lateral sensors are illustrated in Figure 7-15. The FLS covers an area of maximum 100 m radius with 130° opening angle, resulting in roughly 90 m lateral coverage to both sides ahead of the vehicle.
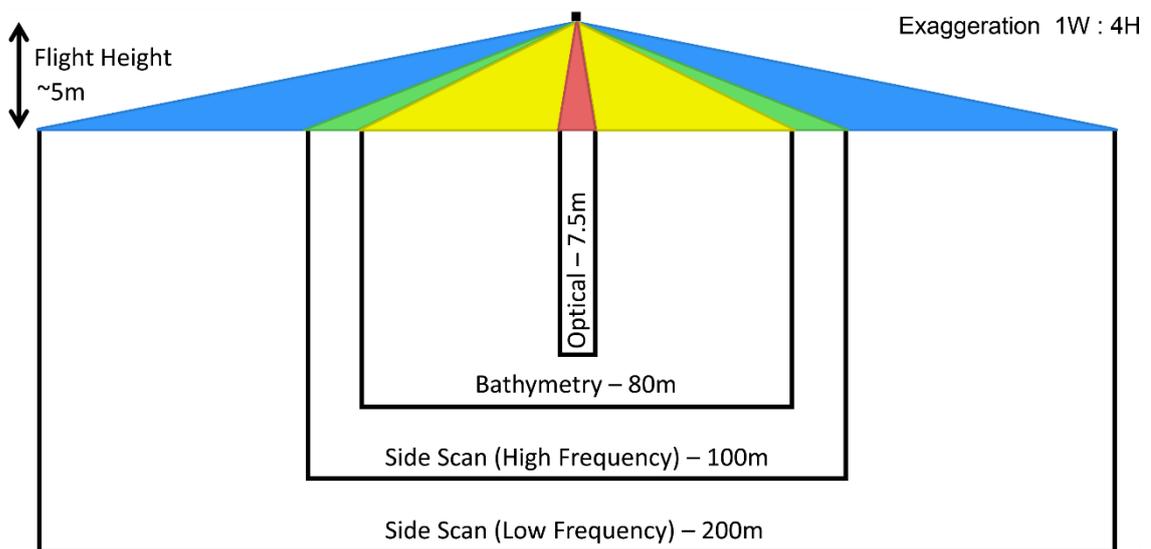
Figure 7-15: Schematic coverages of the OFOBS sensors. Flight height is exaggerated by a factor of four with respect to the swath width, in order to properly visualize the individual ranges. The coverage for the camera is only an approximation as it is highly dependent on the topography below the frame. The ranges of the acoustic systems are not altitude dependent and can actually be increased further. Yet, for the here described survey, the shown ranges have proven to be useful for a balance between range, data quality, and temporal resolution of the soundings.

In the medium air, optical methods can be used to survey the earth's surface from large distances with great resolution. Yet, in hydrographic applications, acoustic technology greatly exceeds the capabilities of optical systems with respect to the achievable range, as visibility and lighting are very limited in aquatic environments. With ship-mounted echosounders, surveyors are capable of covering shallow areas with high resolution and low uncertainty measurements to describe the topography of the seabed in great detail. Adapted to the individual needs, lower frequency echosounders can reach all depth ranges up to 11 km and more. Deep-sea applications, however, cannot keep up the spatial resolution due to large acoustic footprints and a reduced number of measurement points with respect to the covered area (Figure 7-16). For high resolution mapping in the deep sea, researchers and surveyors have to rely on subsea vehicles. Especially when conducting habitat mapping on a smaller biological scale, close-range surveying devices are necessary to resolve the fine geomorphological structures (ridges, steps, slopes, flats, etc.) that influence the settling behavior of the different benthic populations.

Nowadays, for subsea surveys, there are a number of different vehicle technologies available that come in a variety of setups and sensor combinations, all of which have their specific ad-
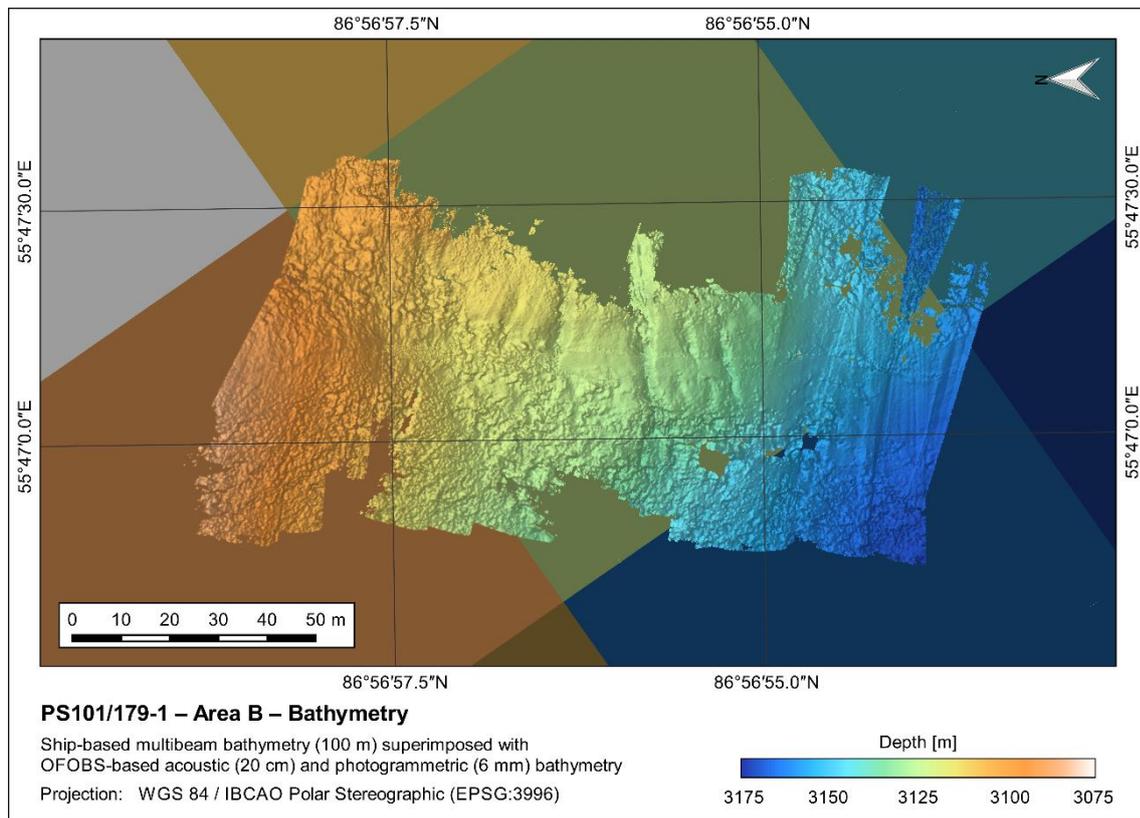
Figure 7-16: Combined bathymetry map of area B. Background bathymetry is from multibeam surveys, conducted during PS101 (Dorschel & Jensen, 2017), superimposed by the OFOBS sonar and photo bathymetry. Depth values in the ship's bathymetry fit well to the OFOBS results. However, small-scale geomorphological structures are not resolved in the grid. Detailed habitat analysis requires higher resolution datasets.

vantages and disadvantages. While there are many examples for acoustic-only surveys with sub-sea vehicles, this discussion will put a focus on optical acquisition as this generally poses a more challenging task.

In the last decade, AUVs have become a popular tool for deep-sea research and industrial surveys as they are very versatile platforms, adaptable for different tasks (Bowen et al., 2014; Kwasnitschka et al., 2016). AUVs are usually built for higher survey speeds and are therefore a good choice for high coverage efficiency. The autonomous operation creates some level of freedom to conduct additional research program in parallel, at least for the time of operation, which is limited by the capacity of the AUV's onboard batteries. Yet, optical mapping with an AUV brings additional limitations and requires a larger amount of survey preparation. For a successful AUV dive, especially in low range applications, a detailed reconnaissance survey is advised prior to mission planning. This is necessary to make sure that the vehicle is in fact capable of carrying out its task in the environment in question. Fin-steered AUVs often have a minimum speed required for maneuvering, which limits the amount and intensity of topographic variability of the seafloor in which the vehicle can keep a constant low flight height over the seabed. Depending on the depths in the area and the resolution of the ship based MBES, these terrain variations might not be resolved in sufficient detail by the reconnaissance survey. Even with obstacle avoidance mechanisms, deploying an AUV in extreme environments leaves a high risk of collision and vehicle loss (Cressey, 2009). In the case of autonomous systems, vehicle loss equals data loss.

A technology, suited for subsea photogrammetric survey, which minimized vehicle and data loss, are ROVs (Sedlazeck et al., 2009; Kwasnitschka et al., 2013; Caress & Barr, 2017). That is for two reasons, both of which also apply to towed sensors. Tethered camera systems can give a direct feedback of the data to the topside unit, allowing operators to react on environmental changes with low latency, hence decreasing the risk of collisions and other accidents. Furthermore, an online connection to the sensors enables safe topside data logging. Raw data can be investigated, evaluated, and processed right away for rapid analysis. While being less efficient with regards to survey coverage. Tethered systems can potentially be powered from the ship, leading to much longer operations times, hence ship time can be made good by saving on recovery and relaunch periods. Additionally, the maneuverability of remotely steered systems has another great advantage over autonomous systems. Due to the instant sensor feedback, areas of particular interest can be investigated in further detail by short-term mission adjustments.

HROVs, a hybrid approach combining autonomous and remotely operated modes into one vehicle, pose additional potential (Bowen et al., 2014; Boetius & Purser, 2017). The area can be observed roughly in remote operation to support decision making and mission planning before switching to the more efficient autonomous survey mode. These systems tend to be limited in operation time due to battery power, but offer high versatility in operation.

One problem with AUV and ROV technology is the overall deployment costs. While these kind of vehicles have a large range of surveying capabilities and can be adapted to various tasks, they tend to be rather expensive, both in hardware and in terms of support. Especially on research expeditions, berths on the ship are limited. Yet, complex vehicles usually require larger groups of technical staff for pre-dive setup, mission programming, launch procedure, piloting, recovery,

and post-dive maintenance. Towed devices on the other hand are cheap to deploy and the personnel requirements are manageable. In the case of the OFOBS, a minimum of two technical engineers is needed to run the system, additional to the ship's crew. Launch and recovery do not require specialized installations, but can be performed with any crane suitable for the air weight of the subsea unit. The lack of thrusters and other motorized moving parts on the OFOBS frame not only minimizes the post-dive maintenance, but additionally creates a noiseless environment, well suited for biological habitat mapping with low acoustic impact on the living populations (besides the ultrasonic signal of the acoustic sensors).

The sensor payload of the OFOBS is highly customizable with regards to the available bandwidth and power requirements. The setup used during PS101 gave suitable results for a wide range of scientific analysis. Especially the simultaneous combination of acoustic and optical instruments created a versatile multilayer dataset. It was mentioned that these two types of sensors tend to create a conflict of interest regarding range, resolution, and quality. This would apply for conventional MBES as the swath width would be greatly limited by the low altitudes. The bathymetric side scan sonar on the other hand gives impressive coverage even on altitudes as low as 2 m and is therefore nicely combinable with short-range, high-resolution optical imaging.

The online sensor stream can be used to optimize the flight height during acquisition in order to find the sweet spot for all onboard sensors. At lower altitudes, the cameras cover a smaller area with increased resolution. The side scan data gives higher contrasts in the imagery, which is great for object identification. However, at lower altitudes, smaller objects or nearby slopes can fully obstruct the side scan signal and areas at higher ranges might not be ensonified due to acoustic shadows.

Increasing the altitude leads to a loss in photographic quality and the side scan data loses contrast. On the other hand, the energy of the MPES is distributed more evenly on the ensonified range. Less lateral acoustic obstacles lead to a better bathymetry coverage. Even though, the following example does not fit in the logic, the higher, the better, but the result of unobstructed coverage can be seen in the bathymetry map of area A compared to the other two areas (Appendix C). This, however, is influenced by the even terrain on the Karasik saddle in contrast to the rough topography of the Vent Mount slopes.

Going up to altitudes higher than ~10 m, the camera data becomes unusable for seafloor observations due to light attenuation and can only be used for water column observations. It needs to be mentioned again that these values refer to the experiences made during PS101. The optical data quality is highly dependent on the water column properties and would be reduced drastically if, for example, a high amount of suspended matter or other marine snow is present. The sonars, however, can still be operated to cover the seafloor at higher altitudes and ranges can be increased to reach the full potential of the two frequencies (HF: 150 m, LF: 250 m, bathymetry: 120 m) (EdgeTech (Ed.), 2015a). This underlines the versatility of the OFOBS. Nonetheless, the combined survey in the lower altitude ranges has proven to be very useful (photogrammetry, navigation adjustments, ground truthing).

Side scan sonars deliver backscatter intensity results that are influenced by the transmitted energy levels, slant range, incidence angle, water properties, transducer characteristics, and other

factors. Therefore, they do not give discrete information on the seabed as such (Lurton, 2004). While the data can be used for object identification according to the shape and size of acoustic shadows in the imagery, amplitude data needs ground truthing of any kind in order to do a correct seabed classification. After the initial side scan survey, locations of different backscatter intensities can be identified to do post-survey ground truthing by taking samples from the seafloor (Dorschel et al., 2009; Hass et al., 2016; Michaelis et al., 2017). In deep-sea environments, this process is error prone due to large position uncertainties. In addition to that, it can become very time consuming, depending on the number of samples ought to be taken. The combined optical and acoustic setup of the OFOBS allows for instant ground truthing up to a certain level, as the interpretation of the camera data can be extrapolated onto the swath width of the side scan data. Clearly, objects and seafloor types that only appear in the outer ranges of the covered area cannot be verified with the camera data. Nonetheless, the OFOBS does not exclude additional investigation after the dive and conventional ground truthing methods can still be applied.

7.3 Recommendations

The acoustic extension of the OFOBS was planned, purchased, and put together within less than a year and the combined system had its first sea trial during the PS101 expedition. During acquisition, the focus was on running and testing the newly installed subsystems. As mentioned earlier, the original OFOS was never intended to be used for photogrammetric reconstruction and this process was added within this thesis project. The processing workflow for the additional datasets (acoustic sensors) and the legacy data (photogrammetric bathymetry from images and videos) was developed and specifically tailored for the data characteristics and the environment they were collected in, as described in chapter 5. While there is most likely room for improvement, the process was developed to the author's best knowledge, by considering the theoretical background gained from literature research, as well as some level of trial and error to evaluate setting alternatives, to minimize overall reconstruction errors, and to subjectively improve the results (as discussed in chapter 7.1).

Nonetheless, from the gained experience during this process, there are a number of recommendations that can be made for future surveys, especially if the photogrammetric microbathymetry is of main interest. As mentioned, the developed workflow is rather complex and less straightforward due to the specific requirements for the individual datasets. Parts of the raw datasets lack certain information that needed to be retrieved manually in post processing with some extra uncertainty. Some of these lacks may be possible to avoid by additional preparation and calibration of the systems prior to the dives.

Additionally, the used software occasionally showed incompatibilities with the dataset and workarounds needed to be developed (e.g. HIPS and SIPS not accepting the vehicle depth records). There are a number of self-written scripts connecting and bridging the different software products and one focus in the future work of this project should be to streamline the processing workflow and gradually incorporate software compatibilities.

7.3.1 Sensor Pre-calibration

In chapter 5.1.1 a brief introduction is given on the effects and the importance of camera calibration. The calibration results from the bundle adjustment for the three sample areas are discussed in chapter 7.1.1. While the obtained results may be sufficient for the presented datasets, a pre-calibration of the OFOBS cameras would be a good way to decrease the level of uncertainty in the reconstruction and stabilize the success rate in case of datasets with stretches of poor imagery or low quality navigation and attitude information.

One approach would be to do an in-air calibration of the two cameras and ensure perfect positioning of the nodal point on the center of curvature of the dome port. While this would theoretically work, it is advised to do an additional in-water calibration at multiple altitudes, using the checkerboard technique to correct for possible misplacement of the camera lenses. Ideally, this calibration would be conducted in the environment of the survey in terms of water properties and refraction indices. Unfortunately, it is a very ambitious task to calibrate underwater cameras in the deep sea.

Another source of uncertainty are the angular offsets between cameras, MPES, and INS. As an input to the SfM process, the position and orientation for the individual images and video frames was calculated from the INS measurements and the theoretical camera installation angles from the design drawings (Appendix A). It is expected that there is an offset between the assumed and the actual angles. These biases can for example be determined by surveying an area (even in air) with known features or reference points. By supplying a correct camera model and position information on the reference points but no initial position and orientation, the bundle adjustment algorithm would estimate the camera poses according to the reconstruction and the obtained results can be compared to the INS measurements to calculate the offsets.

In chapter 2.1.4 it was mentioned that the MPES was roll calibrated during a pool (23L x 19W x 8H m) trial prior to PS101. Unfortunately, the circumstances under which the patch test was performed are not ideal due to limitations of the calibration environment and a shortcoming of technical availability (only simulated USBL). The determination of the yaw bias requires two parallel tracks with sufficient distance and a detectable object located between the survey lines, and the pitch calibration requires a gradual slope on the bottom of the area (IHO, 2005), both of which was not present/possible in the pool. Fortunately, the long dimension of the MPES transducers in along-track direction (Figure 2-5) create sufficient lever arms along the central structure of the bathymetry extension, which minimizes the offset between desired and actual installation angles in yaw and pitch. The roll bias on the other hand could be determined within the calibration environment. Nonetheless, this leaves another possible source of error and an additional full patch test would be advised. This patch test should be conducted in open waters to overcome space limitations and to avoid technical shortcomings. High quality navigation data is required, which limits the calibration area to shallow seas. For additional navigation improvements, a network of long baseline (LBL) transponders or even a GNSS antenna for close-to-surface operation can be considered.

Another approach might be to determine the three angular offsets with a terrestrial laser scanner, by accurately measuring the orientation of the transducer plains with respect to the orientation of the INS pressure housing. This would be a novel method for vessel sensor surveys providing a hypothesis for further investigation. With this approach, it might be possible to determine the orientation of the camera pressure housings in order to estimate the offsets between cameras, MPES, and INS. Hurtós et al. (2010) present a technique to additionally determine the rotation matrix between the sensor frames of a camera and a MBES. This may as well be applicable for the OFOBS cameras and the MPES and could be subject to further research.

7.3.2 Navigation

From various discussions above, it becomes clear that the USBL positioning has the largest contribution to the TPU. This chapter will discuss possibilities to improve the navigation data in the future. Several options shall be listed in order of their feasibility, some of which require additional hardware, while others could potentially be implemented into the system as is.

It is shown that SfM can be used to improve the local navigation. Processing longer track sections would distribute position errors on a larger distance, potentially improving the global position of the dataset. Yet, as mentioned in chapter 5.1.2, processing of large areas, hence higher numbers of input photographs exponentially increases the processing time and effort. The two most time consuming processes are the initial image alignment and the dense reconstruction. While the dense cloud is necessary for higher detail product generation, the alignment process itself is enough to export estimated camera poses used for navigation adjustment. However, aligning larger tracks requires a somewhat constant image quality. Chapter 7.1.4 discusses the effect of poor image quality on the outcome of the SfM process. Slightly longer stretches of bad image quality can lead to gaps in the sparse reconstruction. This would require a large amount of manual tie point definition in the images in order to get a seamless navigation track.

A real time alternative to the post processing approach would be to incorporate simultaneous localization and mapping (SLAM) mechanisms to utilize the video stream and a topside processing computer for real time camera pose estimation (Singh et al., 2007; Pfingsthorn et al., 2016). An additional delayed Kalman filtered solution could be computed from the INS data stream combined with the SLAM calculations. It might also be possible to integrate the FLS into the SLAM framework for an additional input (Hurtós et al., 2014).

A clear recommendation is the additional installation of a Doppler velocity log (DVL). DVLs are widely used on subsea vehicles as an aid for the inertial navigation solution (Titcomb et al., 2012; Kwasnitschka et al., 2013; Bowen et al., 2014; Pfingsthorn et al., 2016; Boetius & Purser, 2017). The DVL acoustically measures the vehicles velocities in the water in all directions according to the Doppler effect (frequency shift) of acoustic signals. While USBL measurements have no drift over time (good accuracy), they have a comparatively low precision. DVLs on the other hand have a bad position accuracy as they do not perform a real position measurement, but the precision of local velocity measurements is very high. Combining those characteristics with the inertial navigation of the INS would improve the computed outcome, as the extra input can be

used to better estimate the internal error model in order to improve the efficiency of the Kalman filter. The onboard PHINS is DVL ready (iXBlue (Ed.), 2014), hence, installing a DVL would not require a new INS but only a thorough calibration of the two sensors.

A more costly venture would be the use of LBL transponders. LBL networks are often used in AUV surveys so that the subsea positioning does not require the presence of the ship in the close vicinity of the subsea vehicle as it does for USBL based positioning (Bowen et al., 2014; Linke & Lackschewitz, 2016). Well-calibrated LBL networks generally have a much higher positioning accuracy due to the longer baseline measurements. In the case of polar surveys, an additional advantage would be the detachment of the influence of sea ice on the USBL positioning quality. However, the benefit of an LBL network highly depends on the individual survey specifications. During PS101, an LBL network of three transponders was placed on the flat Karasik crest (Boetius & Purser, 2017). While this was sufficient for an AUV based research program, it would not be useful for the OFOBS dives. The high topographic variability and the enormous depth changes during the individual dives would require a much higher number of transponders to ensure full coverage, hence more ship time for deployment and recovery, still leaving the uncertainty caused by double echo in the rough terrain of the Langseth Ridge seamounts. An alternative could potentially be an LBL network of sea surface transponders installed on sea ice buoys, positioned via GNSS. It is questionable, if the position accuracy and precision, especially on a local scale between the individual transponders, is sufficient for the travel time difference measurements of the acoustic signal. Thus, this discussion leaves room for further research.

7.3.3 Optical Data

Throughout the duration of this thesis, the value of the optical datasets steadily increased due to its large scope of use (DEM, orthomosaic, navigation adjustment, ground truthing). However, a number of issues could be identified in the process that can potentially be avoided. This chapter will discuss those issues and give recommendations for improvements.

Multisensor applications of any kind usually rely on accurate timestamps to combine the different datasets. SfM on the other hand works content based and time information is not a necessity. Yet, when combining the images with navigation and attitude information for an initial camera pose input, or when reusing the camera poses for time based navigation adjustments, these timestamps are again of significant importance.

As previously outlined, in the OFOBS setup the still images are timestamped by the Posidonia data stream, hence the ship's GNSS based timeserver, and the raw video data has no absolute time information. The one second accuracy for the still image timestamp is not ideal. Chapter 7.1.2 already discusses the misalignment of camera pose data and INS attitude estimation as a potential product of incorrect timing. With an average survey speed of 0.5 knots the OFOBS travels around 25 cm within this uncertainty interval. To pose a more confident navigation source for the bathymetry, a maximum of half the cell size for the position uncertainty should be aimed for. Thus, the timing accuracy should be increased significantly (here: 10 cm, resulting in 0.4 s or less). This can easily be achieved by synchronizing the still image acquisition PC with

the ship's timeserver and save the accurate timestamps in real time to the metadata for the images. Regarding the video, the same procedure should be performed, if technically possible. Otherwise, improved methods for time synchronization in post processing should be investigated.

Another concern is the image quality of the imagery. The still images are generally of high resolution and quality. However, recording raw sensor data from the Canon camera would increase the possibility for post dive image enhancement. The video compression is another subject for investigation. Especially at higher survey speeds, the current compression causes unfortunate motion artifacts in the extracted frames. However, all image quality and compression related changes would increase the data volume that needs to be transferred over the fiber optic cable. Hence, the available bandwidth needs to be taken into consideration. Alternatively, data could be transferred in lower quality in real time and additionally logged on local storage in the OFOBS subsea unit for post dive data retrieval.

In the future, additional hardware changes regarding the camera systems should be investigated. First off, the strobe lights cause a substantial delay on the still image rate due to their recharging time and power consumption. For non mosaic-based statistical analysis, this is sufficient, since still images should not overlap to avoid statistical errors by double counting of benthic individuals. In georeferenced mosaics, this is not an issue, as multiple records of the same individual are merged together. Creating mosaics from barely overlapping still images however creates larger image distortions in the orthorectification process and inconvenient lighting conditions in the longer image ranges. Finding a solution to increase the rate of high resolution still image captures would improve the quality and coverage of the still image mosaics.

Further on, additional across-track cameras could be mounted on the frame to increase coverage of the optical dataset. Parallel cameras would potentially improve the photogrammetric reconstruction as the dataset would become less susceptible to error distribution along the roll rotation. For these additional cameras it wouldn't be necessary to use high resolution still cameras, nor do they need to be incorporated into the live data stream. Additional HD video cameras, recording the data locally, would suffice. The presented datasets show, how the lower resolution video frames can be used to achieve high quality reconstruction results, even though the still images are better suited for mosaic generation.

7.4 Contribution to related Research and Outlook

The main task of this thesis project was to acquire and investigate the datasets and prepare the presented resulting products for further scientific analysis by the associated scientific working groups. This chapter will give an outlook on potential use of the resulting data and the ongoing investigations regarding the acquired raw data.

Firstly, it needs to be mentioned that the OFOBS data is already an important asset during the cruise prior to onshore data processing. During PS101, subsequent to the individual dives, side scan mosaics and bathymetry grids were computed along the raw INS navigation. These grids

show severe artifacts in areas with bad navigation data. However, despite their overall position uncertainty, they could be used for detailed station planning for related research. The success of sediment sampling devices like gravity or multi corer (in this case: television multi corer, TV MUC), for example, logically depends on the presence of sedimentary layers. In abyssal plains or other flat, sedimented areas, their success rate is comparatively high. Yet, in volcanic sea-mount terrain, the chances of hitting rock covered areas or unsuited terrain are high, leading to unsuccessful sampling stations, a significant loss in ship time, and potentially damage of the sampling device itself. The OFOBS video observations already indicate the type of seafloor cover and possible sampling locations can be logged throughout the dive. The side scan mosaics can then be used to extrapolate those observations on a larger area to verify the extend of a sediment patch and to pin point locations suitable for further sampling (Figure 7-17). Nonetheless, detailed post processing of the data significantly improves the quality of the results, as discussed above, which poses additional potential for scientific analyses.

Benthic megafaunal populations are often very sensitive to slight geomorphological variations. Subjective observations made from the OFOBS video data showed that, for example, the settling behavior of large Geodia sponge communities highly depends on the slope inclination of the terrain. Chapter 7.2 already discusses the necessity for high-resolution survey data to conduct
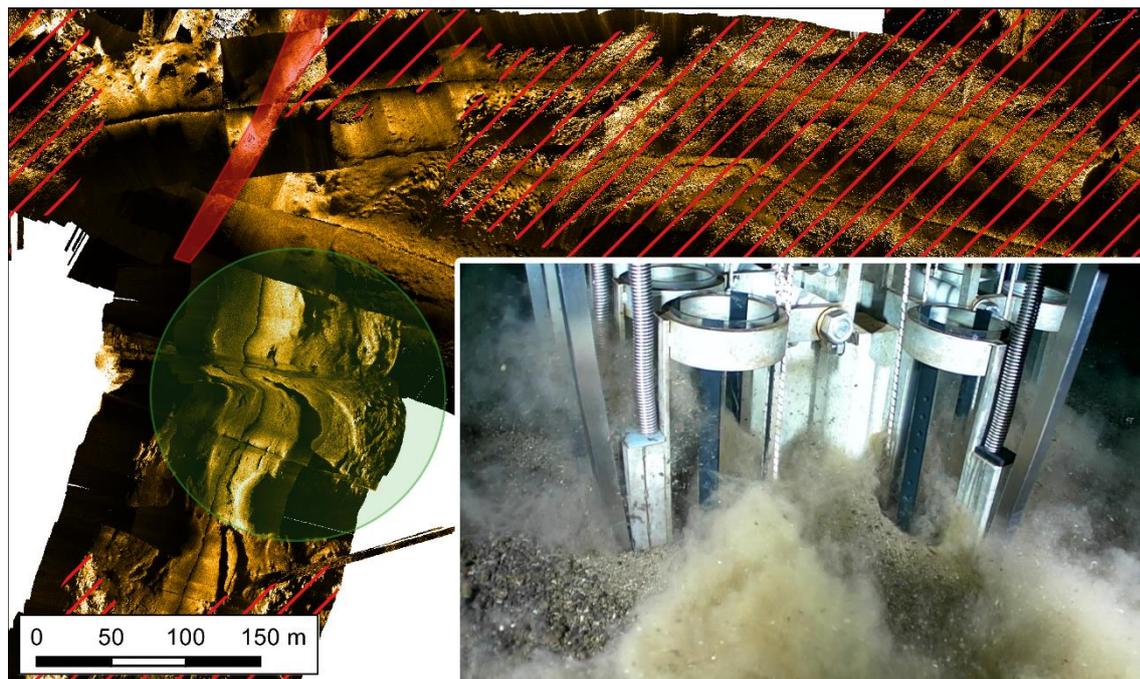
Figure 7-17: Side scan mosaic used for TV MUC station planning. The background map shows the compiled side scan mosaic from dives prior to TV MUC station PS101/167-1. The solid red area marks a steep cliff, hence, unsuited terrain for core sampling. The striped red area marks large fields of pillow basalts, hence, unsuited seabed for core sampling. The remainder of the mapped area is primarily covered by a layer of sediment and the green circle marks the approximate location of the station. The foreground images shows the penetration of the sediment by the TV MUC. (Dreutter et al., 2017b)
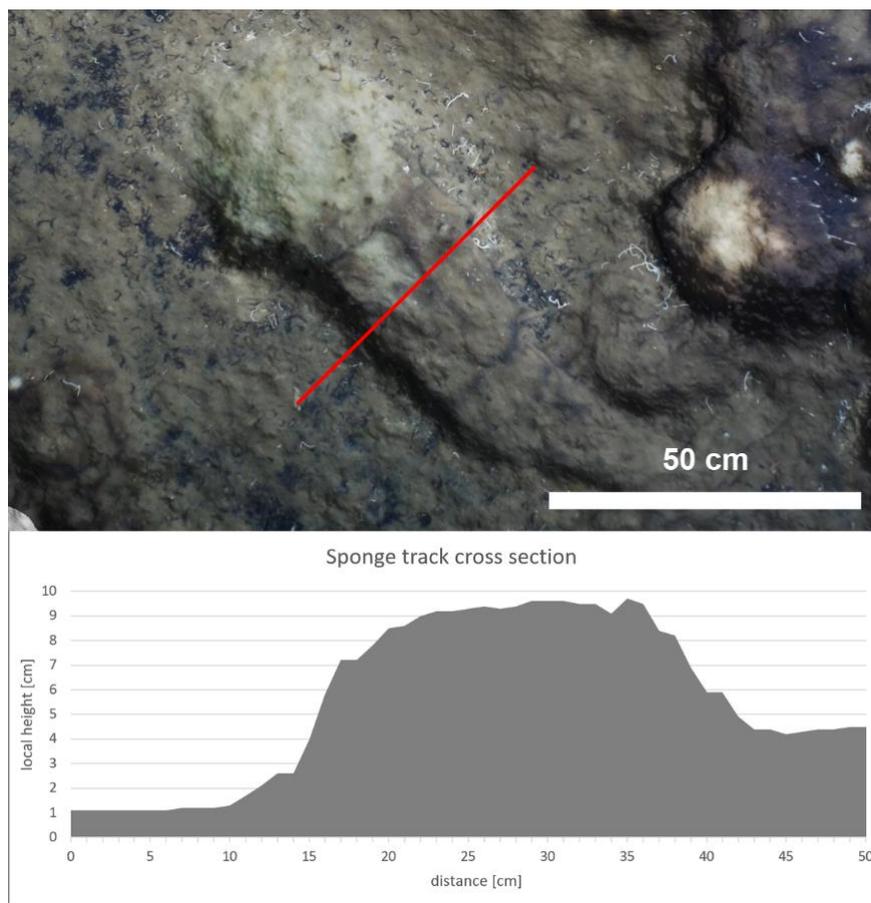
Figure 7-18: Cross section of a track of spicules behind a dead sponge colony. The orthorectified still image is draped over the shaded bathymetry to enhance relief in the imagery. The red line represents the location of the 2D cross section.

small-scale habitat analysis. The OFOBS bathymetry is of such high resolution that these fine topographic variations can be resolved. While the results show larger global position uncertainties (chapter 7.1), the presented navigation corrections result in a more accurate local geometry reconstruction, suitable for thematic interpretation with little artifacts obscuring statistical or visual results. The datasets are fit for a number of habitat characterizing analyses like rugosity, aspect, curvature, slope inclination, bathymetric position index, etc. (Verfaillie et al., 2007; Sen et al., 2016). These results can be combined with geostatistical observations made in the ground truthing image mosaics to perform ecological niche factor analysis or similar statistical analyses (Tong et al., 2012; Marcon & Purser, 2016).

The combination of microbathymetry and imagery holds additional verification capabilities. Often small-scale, three-dimensional shapes of features can hardly be determined from the two dimensional images or video sequences alone. Figure 7-18 shows another example for merging the two results for more advanced interpretation. The 3D models can additionally be used for volume calculations of geological features or biomass estimation by model subtraction. Sufficient methods for reducing the model to the underlying seabed need to be investigated.

One dataset that has not yet been processed is the FLS imagery. This is subject to further research in the OFOBS project. Suman et al. (2015) already demonstrate a pipeline for bathymetric mapping of steep slopes with FLS data. As outlined in chapter 2.2.3, this would be of particular interest for the PS101 dataset, especially since the quality of the MPES bathymetry often deteriorates at cliffs or other steep formations. While it was mentioned in chapter 7.3.2 that the FLS measurements could potentially be incorporated into the navigation scheme for the OFOBS, Hurtós et al. (2014) also present a technique for image registration, mosaicking, and SNR improvement of the sonar frames. The MPES data shows poor image quality and bathymetric results in the close nadir area, which can be filled by the photogrammetry DEM and the orthomosaics. However, having a higher quality sonar mosaic overlying the camera data in the nadir region would pose additional capabilities in ground truthing of the acoustic datasets.

8 Conclusion

This work has introduced the deep-towed *Ocean Floor Observation and Bathymetry System (OFOBS)* as a novel survey tool for close-range, high-resolution, wide-swath habitat mapping in extreme environments of the deep sea. Throughout the project, a processing workflow was developed to produce multilayer microbathymetric results from datasets acquired during the PS101 cruise on *RV Polarstern* along the mountain ranges of the Langseth Ridge in the high Arctic. This workflow was described in detail in chapter 5 and the resulting data products were presented in chapter 6.

The OFOBS showed immense capabilities for deep-sea habitat mapping. By simultaneously logging optical and acoustic survey data, the system creates multiple datasets with different characteristics that can be co-registered in post processing. Compared to traditional towed camera systems, the acoustic data significantly increase the covered area, which may be mapped during a single tow. At the same time, the optical dataset fills gaps in the acoustic data (nadir region) and provides additional capabilities for ground truthing of the sonar imagery. Despite the comparatively large overall position uncertainty of the results presented herein, the local offset between optical and acoustic data is not affected by this positioning error, as it may well be the case with a separated ground truthing approach in deep-sea applications. In addition to the advantage of having multiple datasets for a larger number of potential analyses, the multisensor approach proved to be very beneficial for local corrections within the different processing steps. This led to considerable improvement of the subjective quality and the local accuracy of the results (chapter 7.1.3).

As discussed in chapter 7.2 the survey method holds certain disadvantages over comparable technologies (AUV, ROV, HROV), in terms of coverage efficiency, vehicle maneuverability, and short-term mission adjustment. However, the technique offers several advantages as well. Continuous power supply and topside data storage through the tethered design provides for long operation time, allowing large-scale survey transects to be conducted without in-between recovery and relaunch of the vehicle. The towed setup enables a high variability in flight-height adjustment to adapt the resolution and coverage to the specific research needs in real time during acquisition. With the hydrodynamics of the designed frame, the tethered OFOBS subsea unit moves in a very stable manner, well suited for steady and unobstructed side scan results (accurate navigation data provided). Yet, the biggest advantage, specifically over autonomous vehicles, is the capability of conducting surveys in extreme deep-sea environments like volcanically produced seamounts with steep cliff formations. The forward looking sonar (FLS) creates a high level of confidence for keeping a close range to the seabed while steering the system through rough topography, both up and downhill.

As the system is newly developed and had its first sea trial during PS101, a number of issues were identified during processing of the datasets. These issues were addressed in chapter 7.3 along with recommendations for the further improvement of the system and optimum setup of

existing components for future surveys, with a particular focus on the optical datasets and the vehicle navigation scheme. After all, good scientific survey practice requires constant optimization of the used instruments to the surveyor's best knowledge.

The resulting data products enable a large range of scientific analyses. A non-exhaustive list of possible use cases was discussed in chapter 7.4. The sonar bathymetry is of such high resolution that topographic features of less than one meter in size can be resolved within the swath width of 80 m. This poses high potential for detailed geomorphological and terrain based habitat classifications. The side scan mosaic can be used for object identification and seabed classification within a swath width of 100 m for the HF and 200 m for the LF data. Observations made along the orthorectified photo mosaics can potentially be extrapolated onto the significantly wider area of sonar imagery. It was mentioned, that the photogrammetric DEM and the photo mosaics conveniently fill the nadir gap of the sonar data. However, the subcentimeter resolution of the microbathymetry and the submillimeter resolution of the imagery hold additional potential for very detailed investigations. The DEM resolves megafaunal communities and even smaller candidates such as the crustacean presented in Figure 6-7. Individual sponge colonies can be reconstructed into a 3D model that shows their outer shape and structure, as it is barely visible in 2D observations from the optical data. Combined with the co-registered imagery, this enables detailed structural analysis and high-resolution habitat investigation in post dive digital fieldwork by the associated scientific working groups.

9 References

Agisoft (Ed.) (2016): *Agisoft PhotoScan User Manual: Professional Edition. Version 1.2*. Online: *http://www.agisoft.com/pdf/photoscan-pro_1_2_en.pdf* (Accessed: 2016-11-02).

AML Oceanographic (Ed.) (2015): *Micro-X – User Manual – v1.97*. Online: *http://www.subseatechnologies.com/media/files/page/333011bf/Micro_X_User_Manual_v 1.97_STI.pdf* (Accessed: 2016-09-10).

Baker, E. T. & H. B. Milburn (1997): *MAPR: A new instrument for hydrothermal plume mapping*. RIDGE Events, 8(1), 23-25.

Balletti, C., C. Beltrame, E. Costa, F. Guerra & P. Vernier (2015): *Underwater photogrammetry and 3D reconstruction of marble cargos shipwreck*. The International Archives of Photogrammetry, Remote Sensing and Spatial Information Sciences, 40(5), 7-13. doi:10.5194/isprsarchives-XL-5-W5-7-2015

Barker, B. A. J., I. Helmond, N. J. Bax, A. Williams, S. Davenport & V. A. Wadley (1999): *A vessel-towed camera platform for surveying seafloor habitats of the continental shelf*. Continental Shelf Research, 19(9), 1161-1170. doi:10.1016/S0278-4343(99)00017-5

Bergmann, M., T. Soltwedel & M. Klages (2011): *The interannual variability of megafaunal assemblages in the Arctic deep sea: Preliminary results from the HAUSGARTEN observatory (79°N)*. Deep Sea Research Part I: Oceanographic Research Papers, 58(6), 711-723. doi:10.1016/j.dsr.2011.03.007

Blondel, P. (2009): *The Handbook of Sidescan Sonar*. Chichester, Springer.

Boetius, A. (2016): *Expedition Programme PS101*. *Expeditionsprogramm Polarstern*. Bremerhaven, Alfred Wegener Institute for Polar and Marine Research, 36. doi:10013/epic.48104

Boetius, A. & A. Purser (2017): *The Expedition PS101 of the Research Vessel POLARSTERN to the Arctic Ocean in 2016*. *Berichte zur Polar- und Meeresforschung = Reports on Polar and Marine Research*. Bremerhaven, Alfred Wegener Institute for Polar and Marine Research, 706, 230 p. doi:10.2312/BzPM_0706_2017

Boetius, A. & S. Roessler (2016): *Underwater track data from USBL system IXSEA Posidonia during POLARSTERN cruise PS101 (ARK-XXX/3), links to track files in 1 sec resolution*. PANGAEA. doi:10.1594/PANGAEA.869118

Bowen, A. D., D. R. Yoerger, C. C. German, J. C. Kinsey, M. V. Jakuba, D. Gomez-Ibanez, C. L. Taylor, C. Machado, J. C. Howland, C. L. Kaiser, M. Heintz, C. Pontbriand, S. Suman, L. O. Hara, J. Bailey, C. Judge, G. McDonald, L. L. Whitcomb, C. J. McFarland & L. Mayer (2014): *Design of Nereid-UI: A remotely operated underwater vehicle for oceanographic access under ice*. 2014 Oceans - St. John's, 1-6. doi:10.1109/OCEANS.2014.7003125

Brisson, L. N. & T. Hiller (2015): *Multiphase Echosounder to Improve Shallow-Water Surveys*. *Sea Technology*, August 2015, 10-14.

Brisson, L. N. & D. A. Wolfe (2014): *Performance Analysis of the EdgeTech 6205 Swath Bathymetric Sonar*. Online: *https://www.edgetech.com/wp-content/uploads/2013/09/Performance-Analysis-of-the-EdgeTech-6205-Swath-Bathymetric-Sonar.pdf* (Accessed: 2016-07-29).

Caress, D. W. & N. Barr (2017): *Ocean Imaging Expedition*. Online: *http://www.mbari.org/at-sea/expeditions/ocean-imaging-expedition/* (Accessed: 2017-04-29).

Chang, Y.-C., S.-K. Hsu & C.-H. Tsai (2010): *Sidescan Sonar Image Processing: Correcting Brightness Variation and Patching Gaps*. Journal of Marine Science and Technology, 18(6), 785-789.

Cochran, J. R., G. J. Kurras, M. H. Edwards & B. J. Coakley (2003): *The Gakkel Ridge: Bathymetry, gravity anomalies, and crustal accretion at extremely slow spreading rates*. Journal of Geophysical Research: Solid Earth, 108(B2), 2116. doi:10.1029/2002JB001830

Cressey, D. (2009): *Trapped under ice*. Nature News. doi:10.1038/news.2009.174

de Souza, L. A. P., M. da Silva, T. Hiller, D. A. Wolfe & L. N. Brisson (2015): *Reservoir monitoring using a multi-phase echo sounder: A case study*. Acoustics in Underwater Geosciences Symposium (RIO Acoustics), 2015 IEEE/OES, Rio de Janeiro. doi:10.1109/RIOAcoustics.2015.7473602

Dick, H. J. B., J. Lin & H. Schouten (2003): *An ultraslow-spreading class of ocean ridge*. Nature, 426(6965), 405-412. doi:10.1038/nature02128

Dorschel, B. & L. Jensen (2017): *Swath sonar bathymetry during POLARSTERN cruise PS101 (ARK-XXX/3) with links to multibeam raw data files*. PANGAEA. doi:10.1594/PANGAEA.871047

Dorschel, B., A. J. Wheeler, V. A. I. Huvenne & H. de Haas (2009): *Cold-water coral mounds in an erosive environmental setting: TOBI side-scan sonar data and ROV video footage from the northwest Porcupine Bank, NE Atlantic*. Marine Geology, 264(3–4), 218-229. doi:10.1016/j.margeo.2009.06.005

Dreutter, S., A. Purser, L. Hehemann & A. Boetius (2017a): *Forward looking sonar data collected along OFOBS profiles during POLARSTERN cruise PS101 (ARK-XXX/3)*. PANGAEA. doi:10.1594/PANGAEA.874128

Dreutter, S., A. Purser, L. Hehemann & A. Boetius (2017b): *Side scan sonar and swath bathymetry collected along OFOBS profiles during POLARSTERN cruise PS101 (ARK-XXX/3)*. PANGAEA. doi:10.1594/PANGAEA.873046

EdgeTech (Ed.) (2015a): *2205 Sonar System – General System Manual – 0017471_REV_B*. (Supplied with hardware).

EdgeTech (Ed.) (2015b): *EdgeTech Multi Phase Echo Sounder Technology*. (Supplied with hardware).

Edmonds, H. N., P. J. Michael, E. T. Baker, D. P. Connelly, J. E. Snow, C. H. Langmuir, H. J. B. Dick, R. Muhe, C. R. German & D. W. Graham (2003): *Discovery of abundant hydrothermal venting on the ultraslow-spreading Gakkel ridge in the Arctic Ocean*. Nature, 421(6920), 252-256. doi:10.1038/nature01351

Gao, G. X., L. Heng, T. Walter & P. Enge (2011): *Breaking the ice – Navigation in the arctic*. 24th International Technical Meeting of the Satellite Division of the Institute of Navigation 2011, ION GNSS 2011, 3767-3772.

Gauger, S., T. Hartmann, J. Hatzky & H. W. Schenke (2002): *Swath sonar bathymetry during POLARSTERN cruise ARK-XVII/2 (PS59, AMORE) with links to multibeam raw data files*. PANGAEA. doi:10.1594/PANGAEA.763422

Hass, H. C., F. Mielck, D. Fiorentino, S. Papenmeier, P. Holler & A. Bartholomä (2016): *Seafloor monitoring west of Helgoland (German Bight, North Sea) using the acoustic ground discrimination system RoxAnn*. Geo-Marine Letters. doi:doi:10.1007/s00367-016-0483-1

Hurtós, N., X. Cufi & J. Salvi (2010): *Calibration of optical camera coupled to acoustic multibeam for underwater 3D scene reconstruction*. OCEANS 2010 IEEE-Sydney, IEEE, 1-7. doi:10.1109/OCEANSSYD.2010.5603907

Hurtós, N., D. Ribas, X. Cufí, Y. Petillot & J. Salvi (2014): *Fourier-based Registration for Robust Forward-looking Sonar Mosaicing in Low-visibility Underwater Environments*. Journal of Field Robotics, 32(1), 123-151. doi:10.1002/rob.21516

International Hydrographic Organization (IHO) (Ed.) (2005): *Manual on Hydrography*. *Publication C-13*. Monaco, International Hydrographic Bureau, 1st edition, May 2005.

International Hydrographic Organization (IHO) (Ed.) (2008): *IHO Standards for Hydrographic Surveys*. *Special Publication N° 44*. Monaco, International Hydrographic Bureau, 5th edition, February 2008.

International Oceanographic Commission (IOC) & International Hydrographic Organization (IHO) (Eds.) (2003): *Sixteenth Meeting of the GEBCO Sub-Committee on Undersea Feature Names (SCUFN) – Summary Report.* International Hydrographic Bureau, Monaco.

iXBlue (Ed.) (2011): *USBL-BOX – Positioning System – User Guide*. Online: *http://www.igp.de/manuals/MU_USBLBOX_AN_001_B.pdf* (Accessed: 2016-11-15).

iXBlue (Ed.) (2014): *Phins 6000 – FOG-based high-performance subsea Inertial Navigation System for deep water*. Technical Specifications. Online: *https://www.ixblue.com/sites/default/files/downloads/ixblue-ps-phins_6000-02-2014-web.pdf* (Accessed: 2016-09-02).

iXBlue (Ed.) (2016): *Posidonia II – Ultra-deep, long-range USBL*. Technical Specifications. Online: *https://www.ixblue.com/sites/default/files/downloads/ixblue-ps-posidoniaii-05-2016-web.pdf* (Accessed: 2017-01-10).

IXSEA (Ed.) (2010a): *PHINS 6000 – Quick Start Guide*. (Supplied with hardware).

IXSEA (Ed.) (2010b): *PHINS 6000 – Technical Description*. (Supplied with hardware).

IXSEA (Ed.) (2010c): *PHINS 6000 – User Guide*. (Supplied with hardware).

Jakobsson, M., L. Mayer, B. Coakley, J. A. Dowdeswell, S. Forbes, B. Fridman, H. Hodnesdal, R. Noormets, R. Pedersen, M. Rebesco, H. W. Schenke, Y. Zarayskaya, D. Accettella, A. Armstrong, R. M. Anderson, P. Bienhoff, A. Camerlenghi, I. Church, M. Edwards, J. V. Gardner, J. K. Hall, B. Hell, O. Hestvik, Y. Kristoffersen, C. Marcussen, R. Mohammad, D. Mosher, S. V. Nghiem, M. T. Pedrosa, P. G. Travaglini & P. Weatherall (2012): *The International Bathymetric Chart of the Arctic Ocean (IBCAO) Version 3.0*. Geophysical Research Letters, 39(12). doi:10.1029/2012GL052219

Jakobsson, M., L. Mayer & D. Monahan (2015): *Arctic Ocean Bathymetry: A Necessary Geospatial Framework*. ARCTIC, 68(5), 41-47. doi:10.14430/arctic4451

Jokat, W. & M. C. Schmidt-Aursch (2007): *Geophysical characteristics of the ultraslow spreading Gakkel Ridge, Arctic Ocean*. Geophysical Journal International, 168(3), 983-998. doi:10.1111/j.1365-246X.2006.03278.x

Kunz, C. & H. Singh (2008): *Hemispherical refraction and camera calibration in underwater vision*. OCEANS 2008, 1-7. doi:10.1109/OCEANS.2008.5151967

Kwasnitschka, T., T. H. Hansteen, C. W. Devey & S. Kutterolf (2013): *Doing fieldwork on the seafloor: Photogrammetric techniques to yield 3D visual models from ROV video*. Computers & Geosciences, 52, 218-226. doi:10.1016/j.cageo.2012.10.008

Kwasnitschka, T., K. Köser, J. Sticklus, M. Rothenbeck, T. Weiß, E. Wenzlaff, T. Schoening, L. Triebe, A. Steinführer, C. W. Devey & J. Greinert (2016): *DeepSurveyCam—A Deep Ocean Optical Mapping System*. Sensors, 16(2), 164. doi:10.3390/s16020164

Linke, P. & K. Lackschewitz (2016): *Autonomous Underwater Vehicle „ABYSS "*. Journal of large-scale research facilities JLSRF, 2, 79. doi:10.17815/jlsrf-2-149

Łuczyński, T., M. Pfingsthorn & A. Birk (2017): *The Pinax-model for accurate and efficient refraction correction of underwater cameras in flat-pane housings*. Ocean Engineering, 133, 9-22. doi:10.1016/j.oceaneng.2017.01.029

Lurton, X. (2004): *An Introduction to Underwater Acoustics – Principles and Applications*. Chichester, Springer.

Marcon, Y. & A. Purser (2016): *PAPARA(ZZ)I 2.0: an open-source software interface for annotating deep-sea imagery data*. PANGAEA. doi:10.1594/PANGAEA.861907

Menna, F., E. Nocerino, F. Fassi & F. Remondino (2016): *Geometric and Optic Characterization of a Hemispherical Dome Port for Underwater Photogrammetry*. Sensors, 16, 48. doi:10.3390/s16010048

Michaelis, R., F. Mielck, S. Papenmeier, L. Sander & C. Hass (2017): *Characterisation of hard-substrate habitats in the German Bight (SE North Sea) from video observation*. European Geosciences Union - General Assembly 2017. Vienna - Austria. doi:10013/epic.49689

Nocerino, E., F. Menna, F. Fassi & F. Remondino (2016): *Underwater calibration of dome port pressure housing*. The International Archives of Photogrammetry, Remote Sensing and Spatial Information Sciences, XL-3/W4, 127-134. doi:10.5194/isprsarchives-XL-3-W4-127-2016

Padman, L. & L. Erofeeva (2004): *Arctic Ocean Barotropic Tides – Model Detail*. Online: *https://www.esr.org/AOTIM/arctic_detail.html* (Accessed: 2017-04-04).

Pfender, M. & H. Villinger (2002): *Miniaturized data loggers for deep sea sediment temperature gradient measurements*. Marine Geology, 186(3–4), 557-570. doi:10.1016/S0025-3227(02)00213-X

Pfingsthorn, M., R. Rathnam, T. Luczynski & A. Birk (2016): *Full 3D navigation correction using low frequency visual tracking with a stereo camera*. OCEANS 2016 - Shanghai, 1-6. doi:10.1109/OCEANSAP.2016.7485520

Pizarro, O., A. Friedman, M. Bryson, S. B. Williams & J. Madin (2017): *A simple, fast, and repeatable survey method for underwater visual 3D benthic mapping and monitoring*. Ecology and Evolution, 7(6), 1770-1782. doi:10.1002/ece3.2701

Purser, A., L. Hehemann, S. Dreutter & A. Boetius (2017): *Seabed photographs taken along OFOS profiles during POLARSTERN cruise PS101 (ARK-XXX/3)*. PANGAEA. doi:10.1594/PANGAEA.871550

Purser, A., Y. Marcon, S. Dreutter, U. Hoge, B. Sablotny, L. Hehemann, J. Lemburg, B. Dorschel, H. Biebow & A. Boetius (In review): *OFOBS – Ocean Floor Observation and Bathymetry System: A new towed camera / sonar system for deep-sea habitat surveys*.

Schauer, U. (2012): *The expedition of the research vessel "Polarstern" to the Arctic in 2011 (ARK-XXVI/3 - TransArc)*. Bremerhaven, Alfred Wegener Institute for Polar and Marine Research, 649. doi:10013/epic.39934

Sedlazeck, A., K. Köser & R. Koch (2009): *3D reconstruction based on underwater video from ROV Kiel 6000 considering underwater imaging conditions*. OCEANS 2009-EUROPE, 1-10. doi:10.1109/OCEANSE.2009.5278305

Sen, A., H. Ondréas, A. Gaillot, Y. Marcon, J.-M. Augustin & K. Olu (2016): *The use of multibeam backscatter and bathymetry as a means of identifying faunal assemblages in a deep-sea cold seep*. Deep Sea Research Part I: Oceanographic Research Papers, 110, 33-49. doi:10.1016/j.dsr.2016.01.005

Singh, H., C. Roman, O. Pizarro, R. Eustice & A. Can (2007): *Towards High-resolution Imaging from Underwater Vehicles*. The International Journal of Robotics Research, 26(1), 55-74. doi:10.1177/0278364907074473

Solan, M., J. D. Germano, D. C. Rhoads, C. Smith, E. Michaud, D. Parry, F. Wenzhöfer, B. Kennedy, C. Henriques, E. Battle, D. Carey, L. Iocco, R. Valente, J. Watson & R. Rosenberg (2003): *Towards a greater understanding of pattern, scale and process in marine benthic systems: a picture is worth a thousand worms*. Journal of Experimental Marine Biology and Ecology, 285–286, 313-338. doi:10.1016/S0022-0981(02)00535-X

Suman, S., C. L. Kaiser, M. V. Jakuba & J. C. Kinsey (2015): *Integration and algorithm development for forward looking imaging sonars on hybrid and autonomous underwater robots*. OCEANS 2015 - MTS/IEEE Washington, 1-6. doi:10.23919/OCEANS.2015.7404417

Teledyne BlueView (Ed.) (2015): *M900 Series – Datasheet*. Online: *http://www.blueview.com/assets/Uploads/downloads/m900-series-2d-product-leaflet.pdf* (Accessed: 2016-08-05).

Teledyne BlueView (Ed.) (2016): *User's Manual – M-Series Sonars*. Online: *http://www.blueview.com/assets/Uploads/downloads/205608-00-REV-.pdf* (Accessed: 2016-08-05).

Thiede, J. (2002): *POLARSTERN ARKTIS XVII/2 : Cruise Report: AMORE 2001 (Arctic Mid-Ocean Ridge Expedition)*. Bremerhaven, Alfred Wegener Institute for Polar and Marine Research, 421. doi:10013/epic.10426

Titcomb, J., M. Girault & F. Napolitano (2012): *INS and DVL for Out-of-Straightness Surveying*. Hydro International, 16(2).

Tong, R., A. Purser, V. Unnithan & J. Guinan (2012): *Multivariate Statistical Analysis of Distribution of Deep-Water Gorgonian Corals in Relation to Seabed Topography on the Norwegian Margin*. PLOS ONE, 7(8), e43534. doi:10.1371/journal.pone.0043534

Triggs, B., P. F. McLauchlan, R. I. Hartley & A. W. Fitzgibbon (2000): *Bundle Adjustment — A Modern Synthesis*. International Workshop on Vision Algorithms, Corfu, 298-372. doi:10.1007/3-540-44480-7_21

Van Damme, T. (2015): *Computer Vision Photogrammetry for Underwater Archaeological Site Recording in a Low-Visibility Environment*. The International Archives of Photogrammetry, Remote Sensing and Spatial Information Sciences, 40(5), 231-238. doi:10.5194/isprsarchives-XL-5-W5-231-2015

Verfaillie, E., P. Doornenbal, A. J. Mitchell, J. White & V. Van Lancker (2007): *The bathymetric position index (BPI) as a support tool for habitat mapping*. Worked example for the MESH Final Guidance, 14 pp.

Verhoeven, G. (2011): *Taking computer vision aloft–archaeological three-dimensional reconstructions from aerial photographs with photoscan*. Archaeological Prospection, 18(1), 67-73. doi:10.1002/arp.399

Wessel, P., D. T. Sandwell & S.-S. Kim (2010): *The global seamount census*. Oceanography, 23(1), 24-33. doi:10.5670/oceanog.2010.60

Zhukovsky, M. O., V. D. Kuznetsov & S. V. Olkhovsky (2013): *Photogrammetric techniques for 3-D underwater record of the antique time ship from Phanagoria*. The International Archives of Photogrammetry, Remote Sensing and Spatial Information Sciences, 40, 717-721. doi:10.5194/isprsarchives-XL-5-W2-717-2013

Appendix A – OFOBS Design Drawings
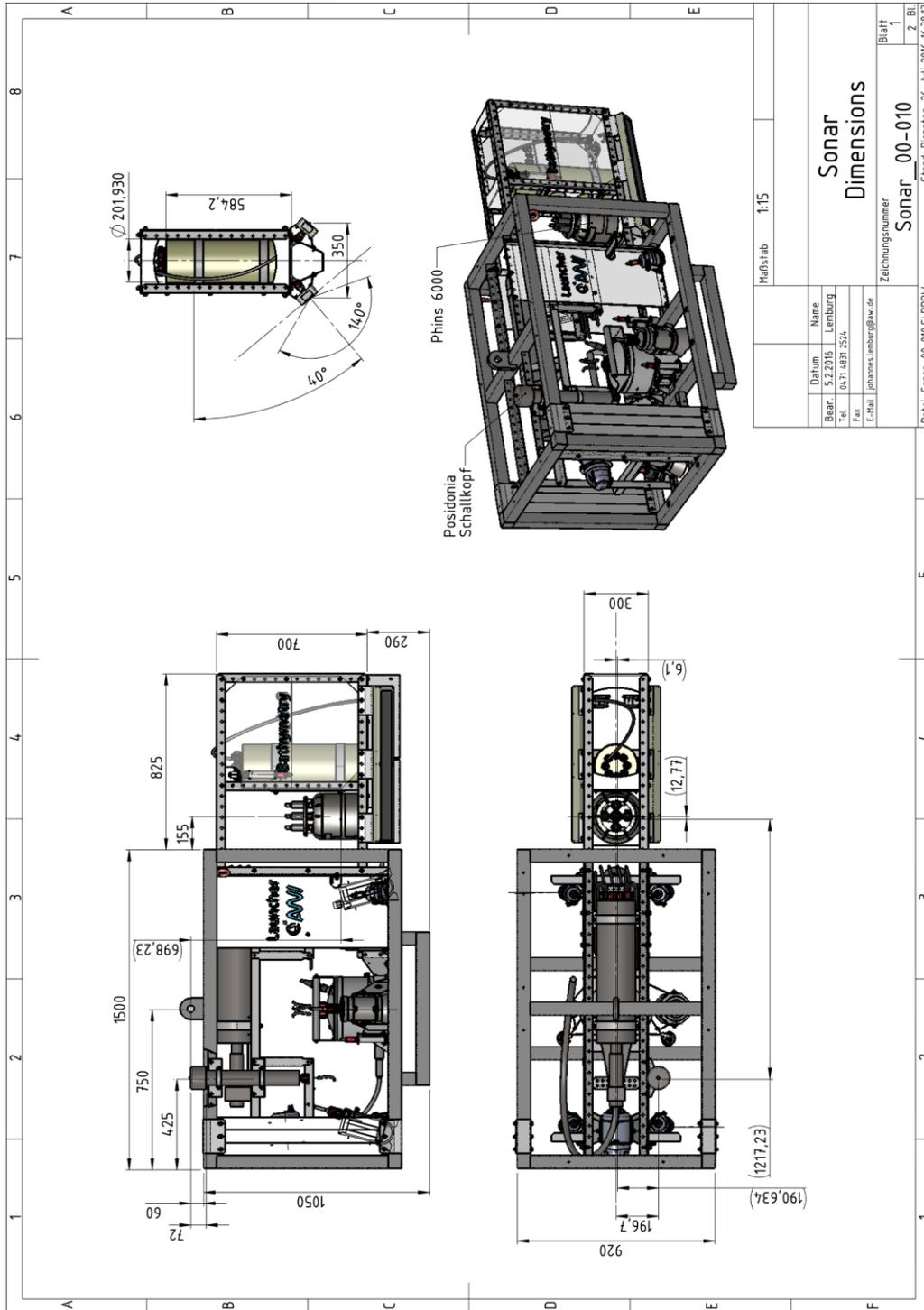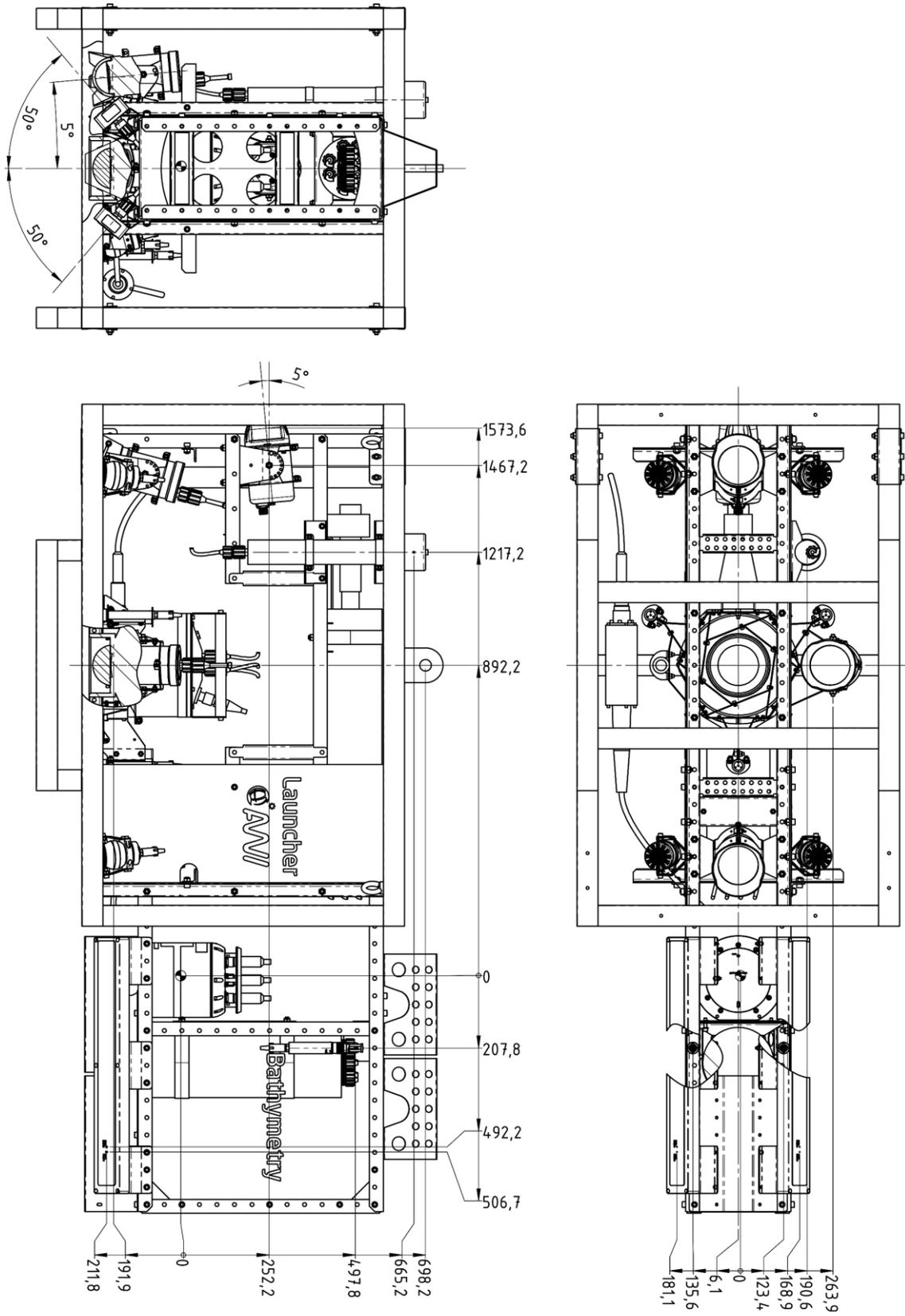
Appendix B – Camera Distortion Plots
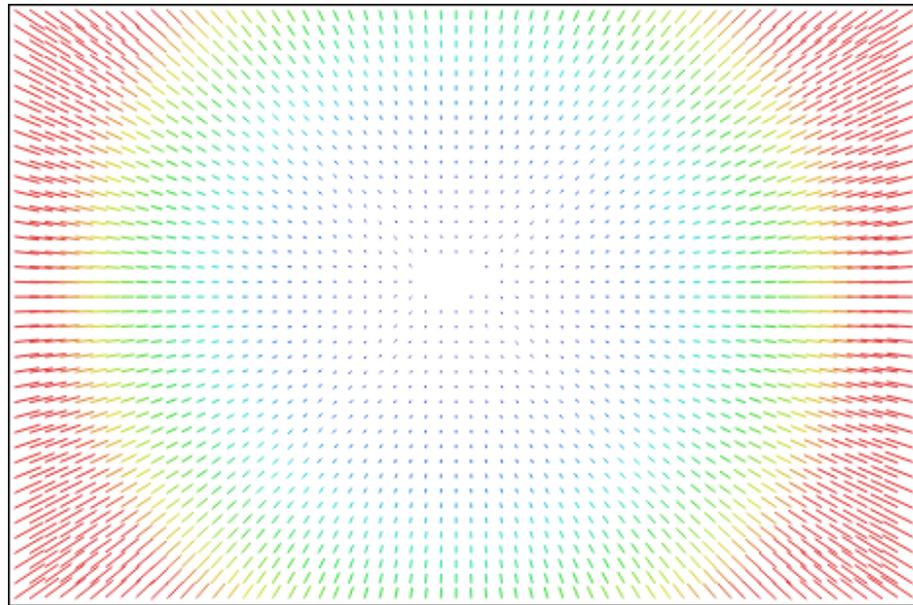
618 pix

Distortion Plot – Stills Camera – Area A
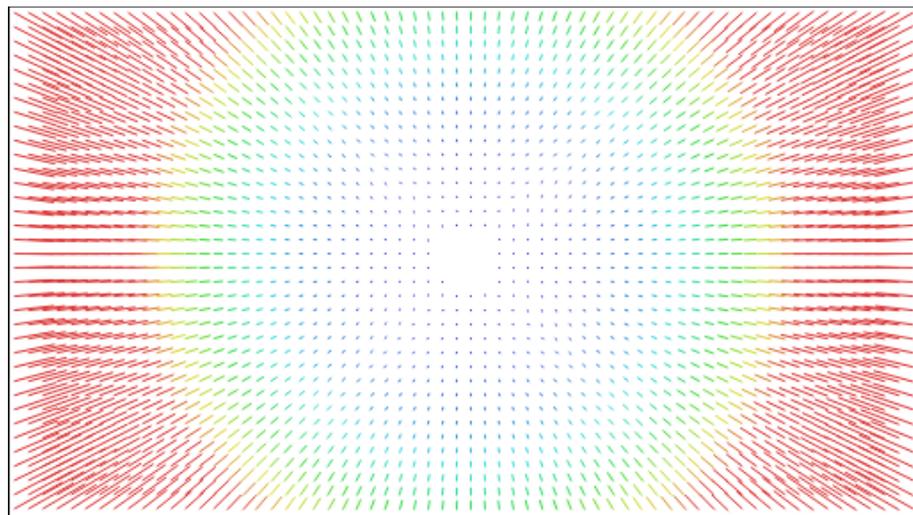
187 pix

Distortion Plot – Video Camera – Area A
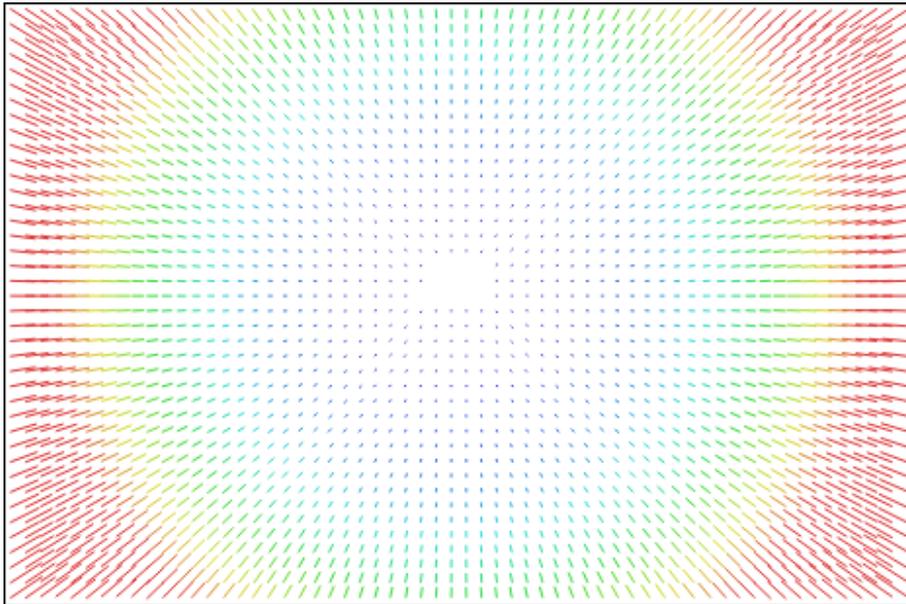
618 pix

Distortion Plot – Stills Camera – Area B
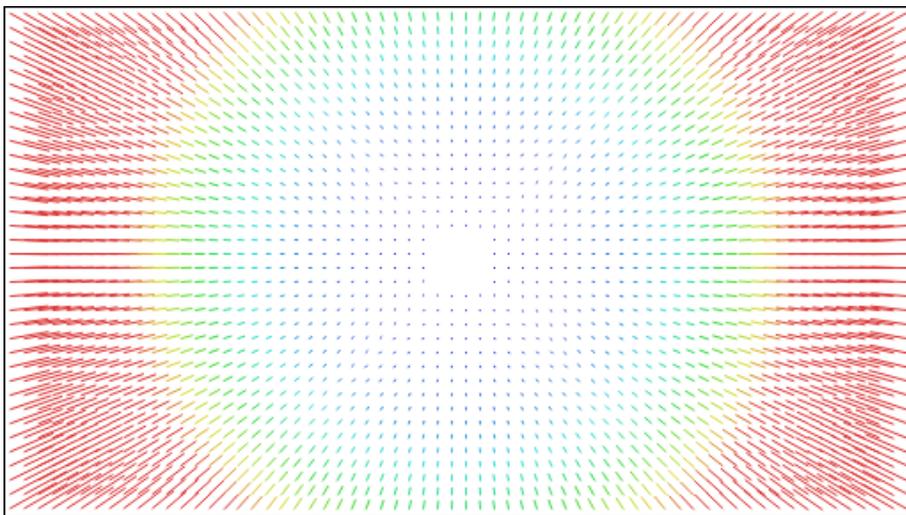
187 pix

Distortion Plot – Video Camera – Area B
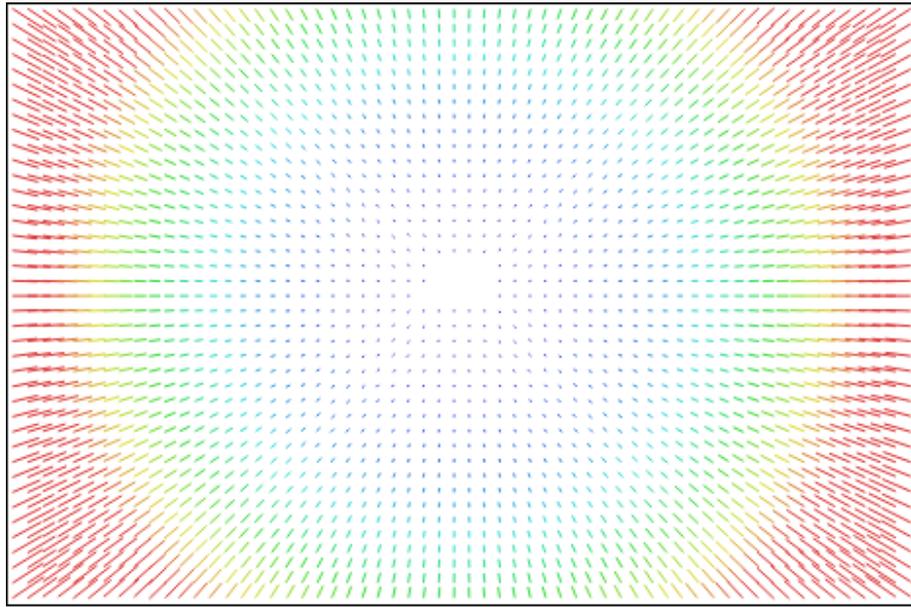
618 pix

Distortion Plot – Stills Camera – Area C
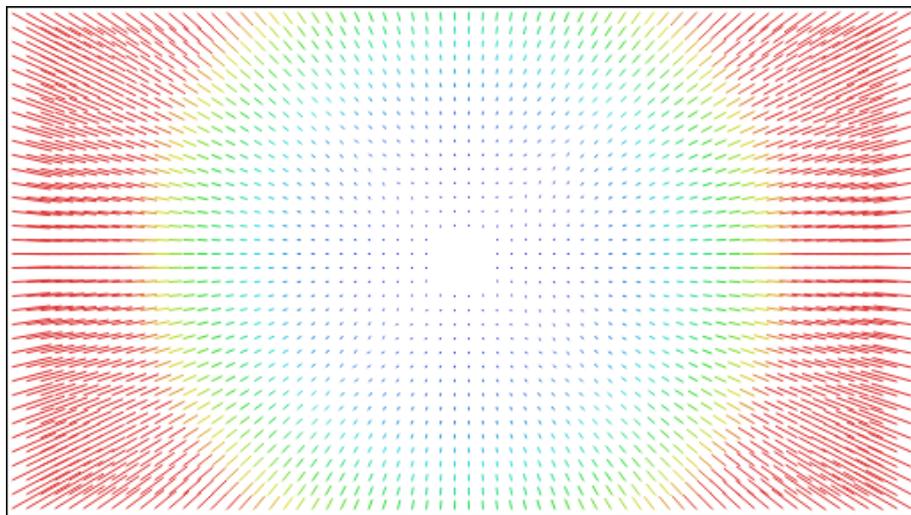
187 pix

Distortion Plot – Video Camera – Area C

Appendix C – Maps
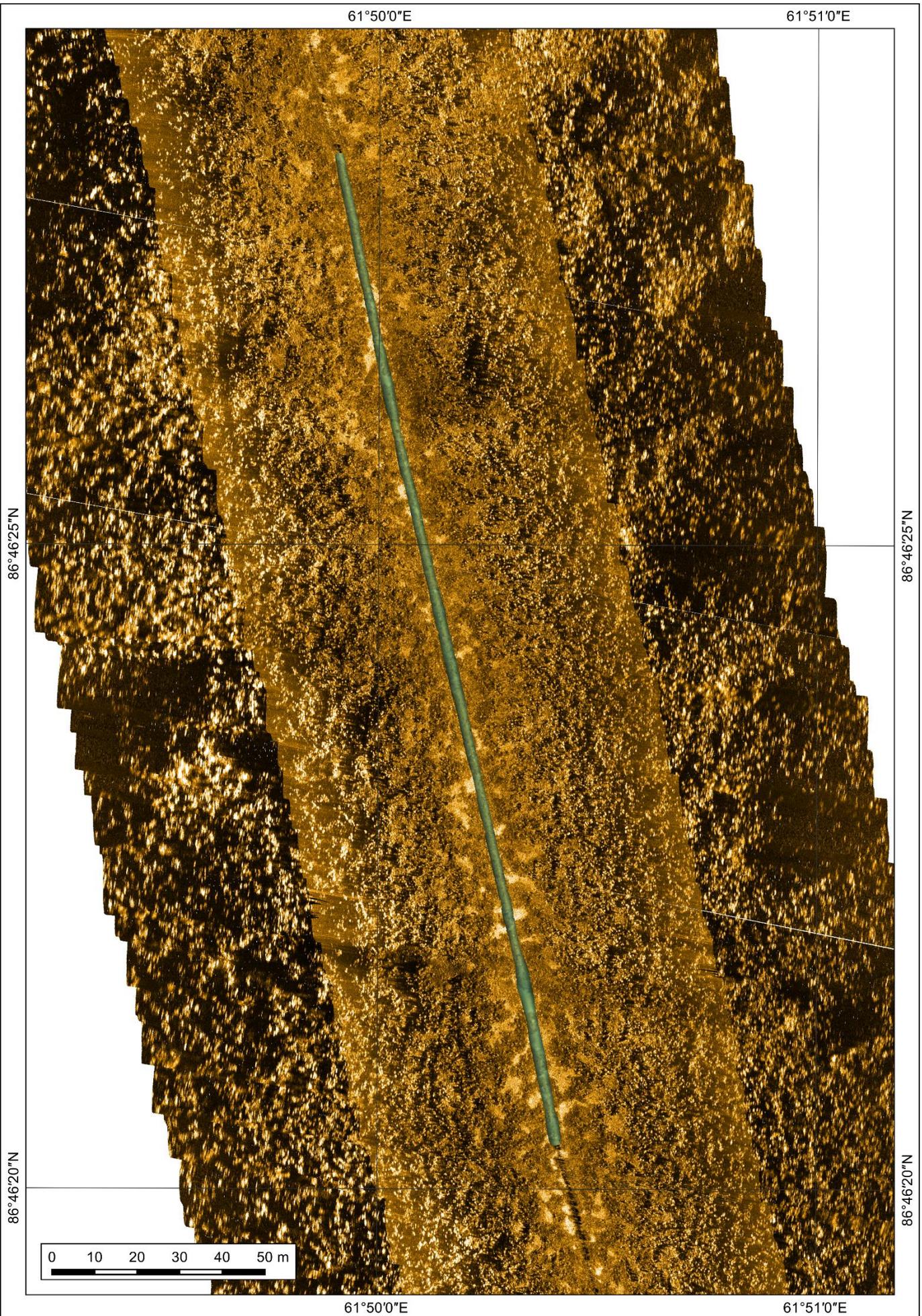
PS101/169-1 – Area A – Side Scan Mosaic & Image Orthomosaic

230 kHz side scan mosaic superimposed with 540 kHz side scan mosaic
and image orthomosaic

Projection: WGS 84 / IBCAO Polar Stereographic (EPSG:3996)

PS101/169-1 – Area A – Bathymetry

540 kHz swath sonar bathymetry superimposed with
photogrammetry derived microbathymetry

Projection: WGS 84 / IBCAO Polar Stereographic (EPSG:3996)

Depth [m]

1120   1115   1110

55°47'0.0"E   **55°47'30.0"E**

86°56'57.5"N

86°56'55.0"N

0   10   20   30   40   50 m

55°47'0.0"E   **55°47'30.0"E**
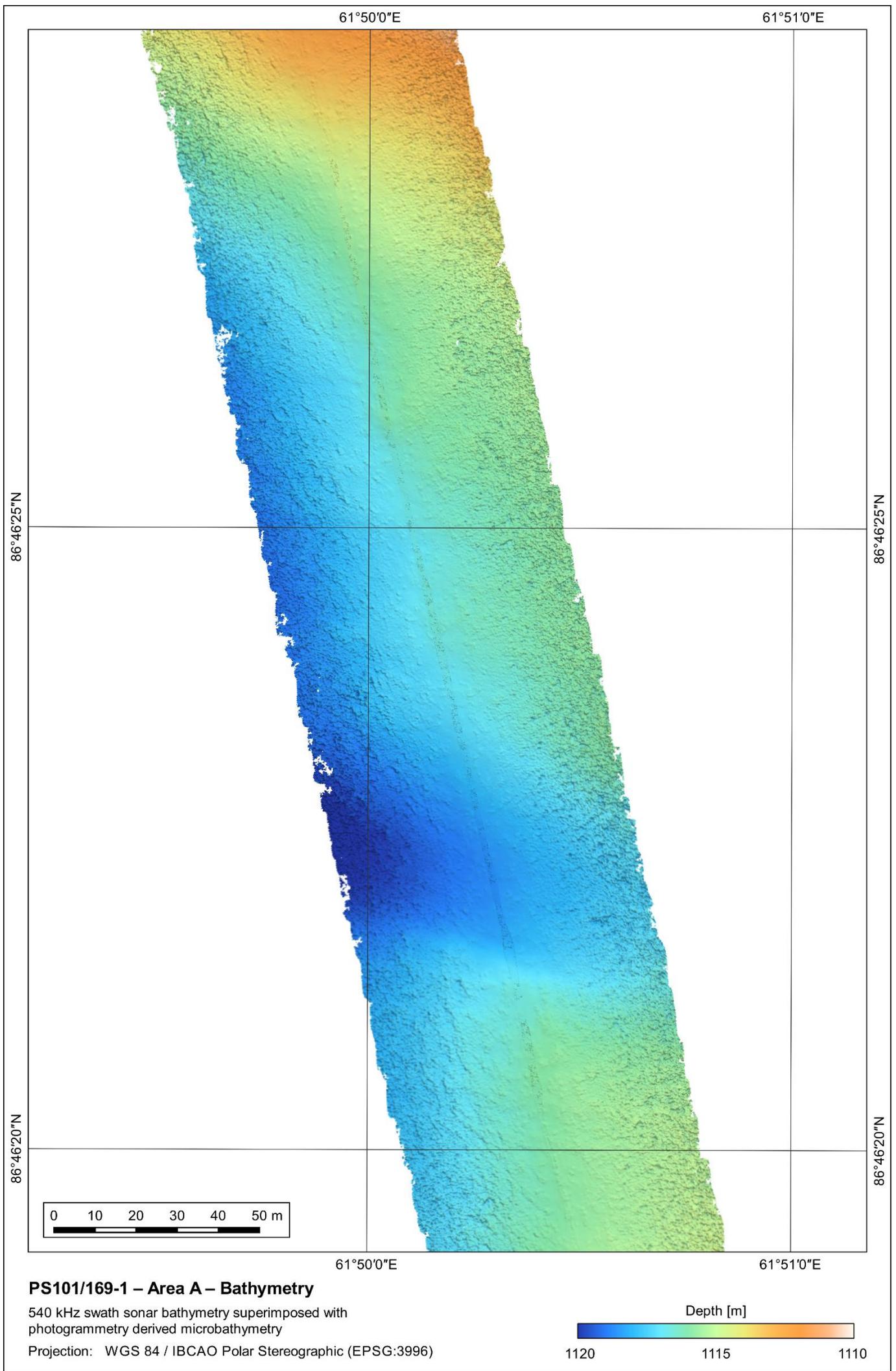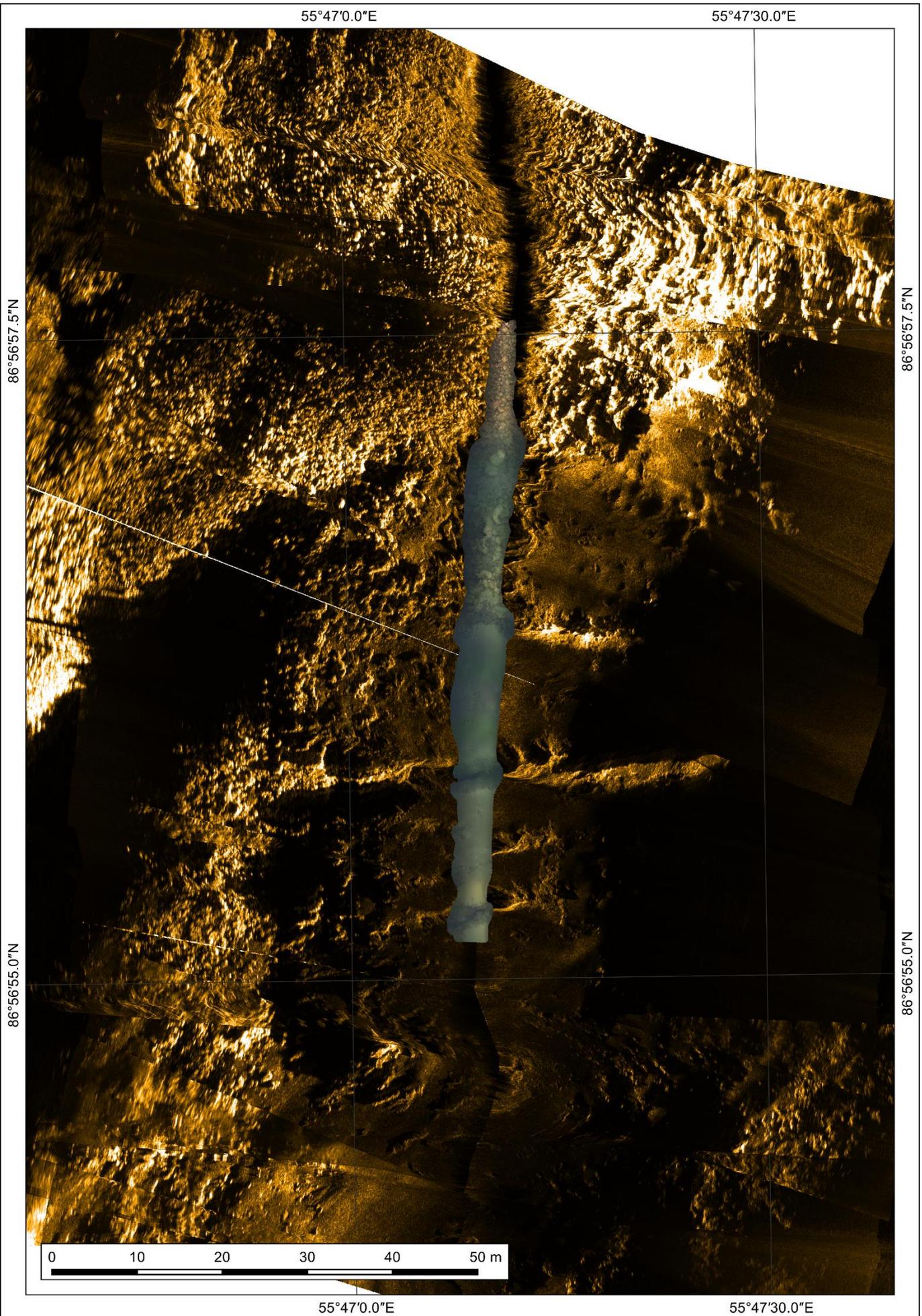
PS101/179-1 – Area B – Side Scan Mosaic & Image Orthomosaic

230 kHz side scan mosaic superimposed with 540 kHz side scan mosaic
and image orthomosaic

Projection: WGS 84 / IBCAO Polar Stereographic (EPSG:3996)
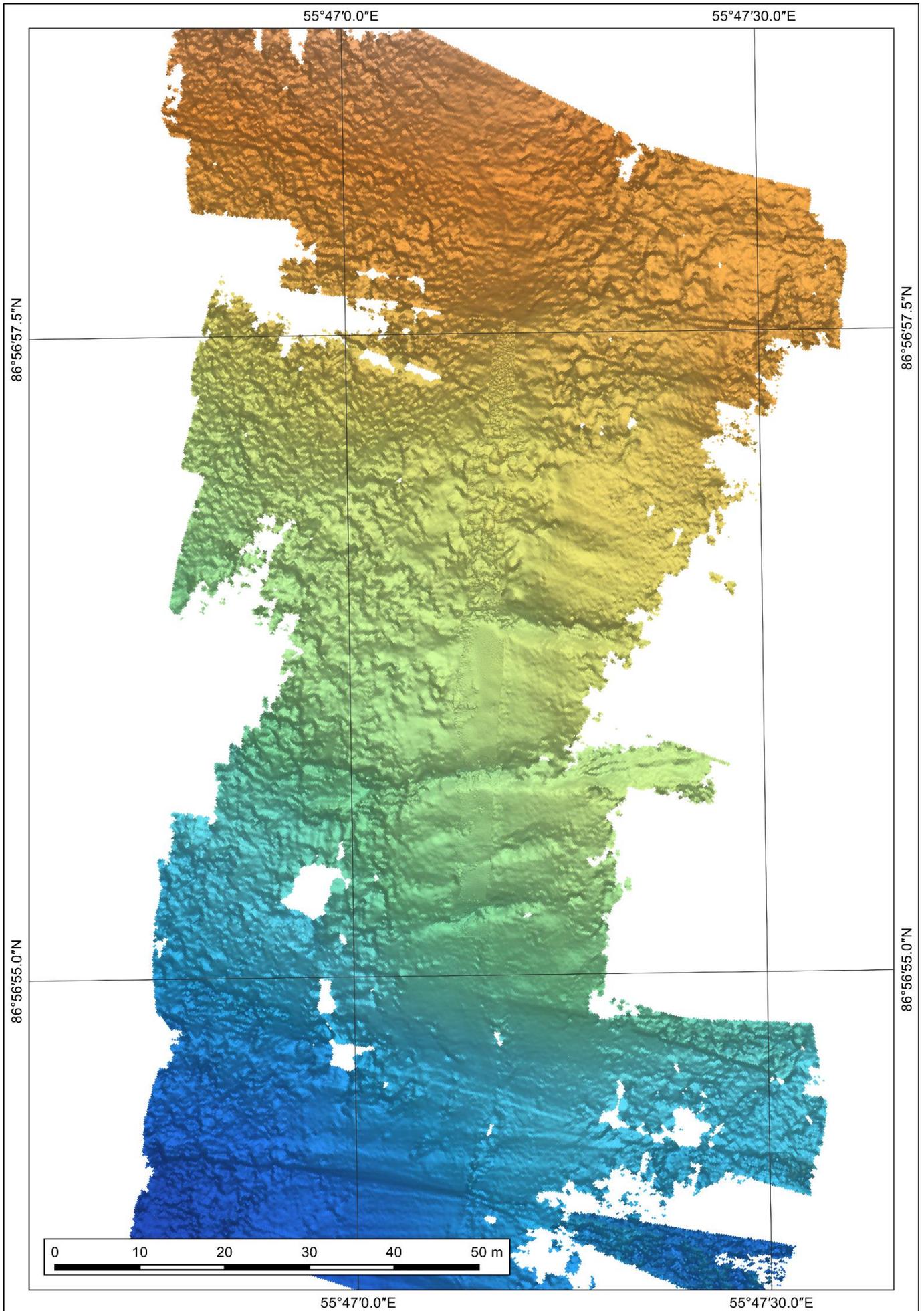
PS101/179-1 – Area B – Bathymetry

540 kHz swath sonar bathymetry superimposed with
photogrammetry derived microbathymetry

Projection: WGS 84 / IBCAO Polar Stereographic (EPSG:3996)

Depth [m]

3175   3150   3125   3100   3075
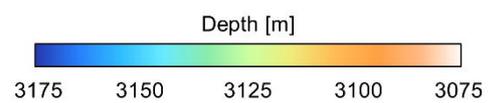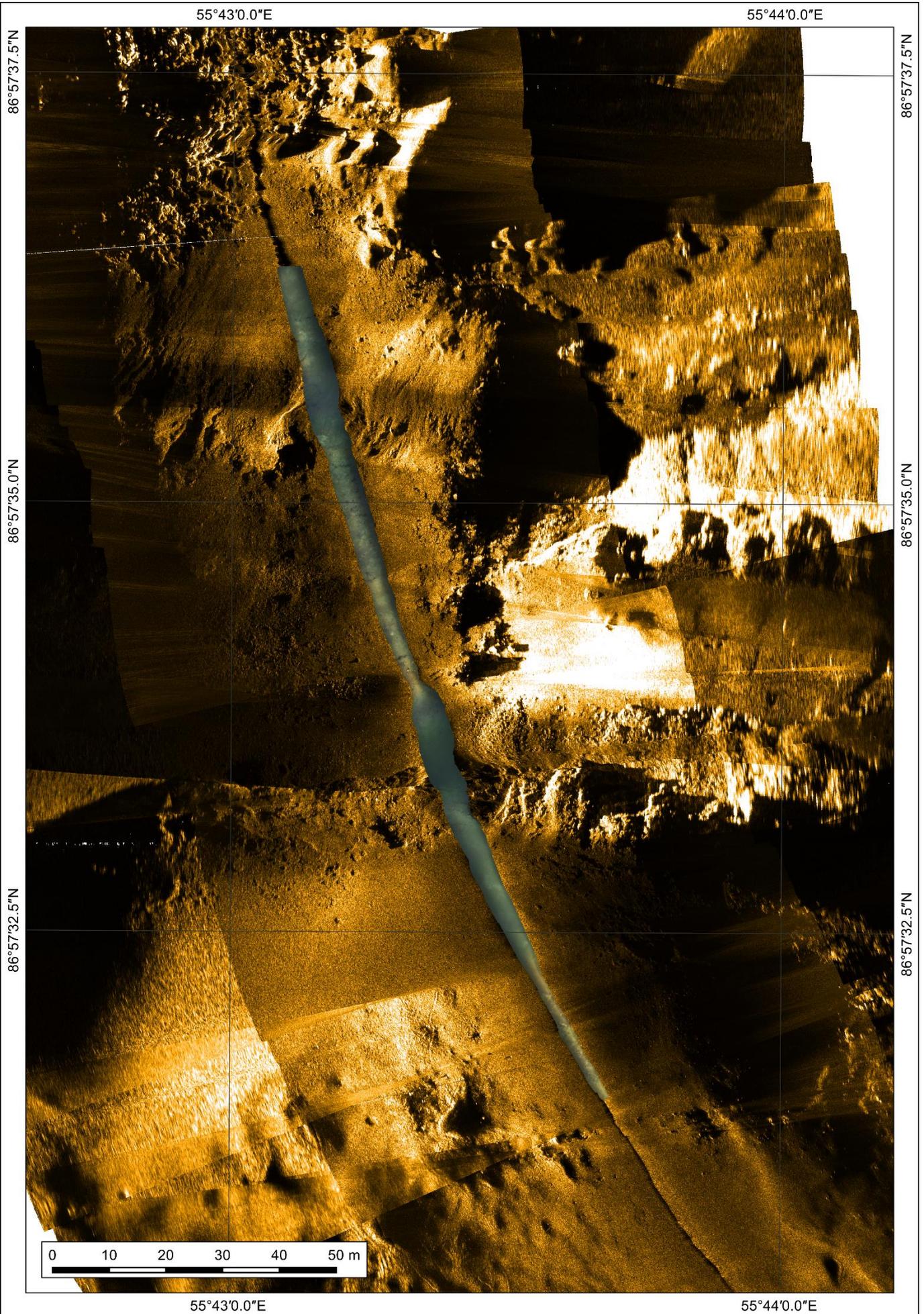
PS101/179-1 – Area C – Side Scan Mosaic & Image Orthomosaic

230 kHz side scan mosaic superimposed with 540 kHz side scan mosaic
and image orthomosaic

Projection: WGS 84 / IBCAO Polar Stereographic (EPSG:3996)

PS101/179-1 – Area C – Bathymetry

540 kHz swath sonar bathymetry superimposed with
photogrammetry derived microbathymetry

Projection: WGS 84 / IBCAO Polar Stereographic (EPSG:3996)

Depth [m]

3190 3180 3170 3160 3150 3140